Function and Regulation of Cytochrome P450 4V2 and the Implications in Bietti's Crystalline Dystrophy

Catherine M. Lockhart

A dissertation

submitted in partial fulfillment of the

requirements for the degree of

Doctor of Philosophy

University of Washington

2016

Reading Committee:

Edward J. Kelly, Chair

Danny D. Shen

Shiu-Lok Hu

Program Authorized to Offer Degree:

Pharmaceutics

University of Washington

Abstract

Function and Regulation of Cytochrome P450 4V2 and the Implications in Bietti's Crystalline Dystrophy

Catherine M. Lockhart

Chair of the Supervisory Committee:

Associate Professor Edward J. Kelly

Department of Pharmaceutics

Background: Cytochrome P450 4V2 (CYP4V2) is one of 57 functional human isozymes in the cytochrome P450 superfamily of heme-containing monooxygenase enzymes. CYP4V2 is one of thirteen human P450 enzymes classified as 'orphans' because their substrate specificity and role in physiological function are not well characterized. CYP4V2 is ubiquitously expressed, with known ω-hydroxylase activity for medium-chain fatty acids, and is believed to play a role in lipid homeostasis. In 2004, researchers at the National Eye Institute identified a mutation in the 'orphan' cytochrome P450 4V2 (*CYP4V2*) gene in patients with Bietti's crystalline dystrophy (BCD), a rare, degenerative, blinding retinal disease. In genetic studies aside from BCD, a common polymorphism in *CYP4V2* has been associated with deep vein thrombosis, and expression

of CYP4V2 has been inversely correlated with tumor grade in breast cancer. The research described in this dissertation was conducted to better understand normal physiological function of CYP4V2, to further elucidate the molecular mechanisms behind BCD, and to identify potential therapeutic targets that may lead to treatment options.

Methods: *Murine model of BCD*. With assistance from the University of Washington Transgenic Core Facility, embryonic stem cells with targeted disruption of the *Cyp4v3* gene were obtained from the Knockout Mouse Project. The embryonic stem (ES) cell clone was expanded on embryonic feeder cells, evaluated for correct gene targeting by polymerase chain reaction (PCR), and then injected into albino C57Bl/6 blastocysts to generate chimeric mice. Offspring that inherited the targeted Cyp4v3 allele were interbred as heterozygotes for production of *Cyp4v3*$^{-/-}$ mice. To confirm the null allele in Cyp4v3$^{-/-}$ mice, genotype analysis was performed by PCR. To confirm that the *Cyp4v3* gene targeting event is truly null, CYP4V3 protein expression was assessed by Western blot analysis. To screen for changes in ocular appearance, a Micron II small animal retinal imaging system from Phoenix Research Laboratories was used to capture fundus images. Analysis of 20 μL sera from *Cyp4v3* knockout and wild-type mice for PUFA content was performed using methanol and methyl-t-butyl ether (MTBE), and total fatty acids were analyzed by GC-EI/MS. For histologic analysis, whole eyes were harvested from mice and immediately fixed in 10% formalin for standard histological processing and hematoxylin & eosin staining. Whole eyes were also immediately frozen in Tissue-Tek optimum temperature cutting compound for histologic processing and Oil Red O staining for lipid content. Additionally, whole eyes were immediately submerged in 1/2x Karnovsky's fixative, postfixed in osmium tetroxide and processed, sectioned, and

examined by transmission electron microscopy. In addition to fundus images additional tests for visual acuity and function were conducted in collaboration with colleagues at Oregon Health and Science University. Electroretinograms were measured on dark-adapted mice anesthetized with ketamine/xylazine. Pupils were dilated, electrodes applied, and the electrical transmission of the retina was recorded from light flash intensities ranging from -4.34 to 3.55 log cd•s/m^2. Optical coherence tomography was conducted on mice sedated using 1.5% isofluorane delivered via nose cone, with anesthetized corneas and dilated pupils, using linear horizontal scans in the temporal and nasals quadrants and linear vertical scans in the superior and inferior quadrants. Visual acuity was measured by optokinetic response in which computer monitors form a virtual cylinder of rotating sine-wave vertical gratings, which randomly rotates clockwise or counterclockwise, and mice reflexively respond to the rotating gratings by turning their head in the corresponding direction. A minimum of two to seven days lapsed between anesthesia and testing for each mouse.

CYP4V2 mutations in BCD. At regular intervals, the patient underwent ophthalmic examination and testing, which included best-corrected visual acuity (BCVA), fundus color photography, wide-field fundus autofluorescence (AF; Optos), wide-field fluorescein angiography (FA; Optos), semi-automated kinetic and automated static full-field perimetry (Octopus 101/900, Haag-Streit, Inc), spectral-domain optical coherence tomography (OCT; Heidelberg Engineering), and ERG. To conduct the genotype analysis, DNA was extracted from buccal swabs from a BCD patient and a healthy control. Each exon was individually amplified from extracted DNA by standard polymerase chain reaction and validated by gel electrophoresis. Sequencing results were

analyzed for homology to known CYP4V2 sequence using the Basic Local Alignment Search Tool (BLAST, http://blast.ncbi.nlm.nih.gov). A homology model of wild-type CYP4V2 was constructed using the I-TASSER server, and all molecular dynamics (MD) simulations were performed in Gromacs 4.6.5.

Regulation of *CYP4V2*. Human liver microsomes, total mRNA, and total RNA was extracted from human liver tissue from the University of Washington liver bank. Whole genome expression was measured from total mRNA, SDS-PAGE and Western blot analysis of prepared human liver microsomes were conducted and quantified, and total RNA was used to screen for miRNA expression by microarray analysis. To validate a regulatory interaction by the candidate miRNA (miR-146b-5p), HepG2 cells were stably transfected with plasmid vectors containing the complete CYP4V2 3'UTR, and either a vector to overexpress miR-146b-5p, or a non-targeting control. Luciferase activity was evaluated using the SecretePair® Dual Luminescence Assay and measured with a Synergy HTX plate reader. ARPE-19 cells were transiently transfected with plasmids to overexpress miR-146b-5p, or a non-targeting control miRNA, fixed in methanol, and incubated with fluorescent-tagged antibodies. The processed samples were analyzed with a Nikon Ti-S microscope, and the ratio of CYP4V2 to GFP signal was determined for each transfection condition. Absolute protein was measured using LC-MS/MS techniques and two unique signature peptides.

Results: We demonstrated that *Cyp4v3*$^{-/-}$ mice recapitulate the most significant elements of the phenotype observed in BCD, particularly the development of glistening yellow-white crystalline deposits in the retinal tissue, a defining characteristic of BCD. In a patient with BCD, we successfully determined her genotype, the first homozygous point

mutation that had previously only been reported as one allele in a compound heterozygous patient. We also were the first to develop a sequence homology model describing the functional deficiency caused by this homozygous point mutation. In an effort to elucidate the biochemistry of CYP4V2 in normal physiological function, we showed strong evidence that CYP4V2 is influenced by regulatory pressure of microRNA (miR-146b-5p). Finally, we described rationale for conducting a pilot gene replacement therapy study in our knockout mouse model using an adeno-associated virus (AAV) vector packaged with functional CYP4V2 cDNA.

Conclusion: This dissertation presents a collection of studies aimed at better characterizing CYP4V2 in normal physiological function, and to begin to elucidate the aberrant physiology observed in BCD. We developed a knockout mouse model that recapitulates the hallmark phenotype observed in BCD, and is a promising preclinical model for further evaluation of the pathophysiology of BCD, as well as a platform for screening potential therapeutic options, including gene replacement therapy or treatment with small molecule candidates. Finally, we identified miR-146b-5p as a candidate for regulation of expression and function of CYP4V2, which contributes to our knowledge of the role of CYP4V2 in normal physiology and can lead to better understanding of the abnormal pathophysiological mechanism of disease.

Table of Contents

List of Figures

List of Tables

Acknowledgements

For their invaluable input and guidance, I thank Richard G. Weleber, MD, and Paul Yang, MD, PhD, from the Casey Eye Institute at Oregon Health Sciences University; Russell van Gelder, MD, PhD, professor and chair of the Department of Ophthalmology at the University of Washington; and J. Fielding Hejtmancik, MD, PhD, from the National Eye Institute. I also thank the University of Washington Drug Metabolism, Transport and Pharmacogenomic Research program; the University of Washington School of Pharmacy Mass Spectrometry Center; Warren Ladiges, DVM, MS, director of the Department of Veterinary Medicine, at the University of Washington; Kelly Hudkins, MS, for histology and pathology support; H. Denny Liggitt, DVM, PhD, for his veterinary pathology expertise; and Scott Greenwald, PhD, for assistance with fundus imaging.

Dedication

The work described in this dissertation is dedicated to patients with rare diseases, particularly those with Bietti's crystalline dystrophy, who are my inspiration and drive my passion to research.

Chapter 1

Introduction: Bietti's Crystalline Dystrophy and Cytochrome P450 4V2

1.1 Introduction

Cytochrome P450 4V2 (CYP4V2) is one of 57 functional human isozymes in the cytochrome P450 superfamily of heme-containing monooxygenase enzymes. CYP4V2 is one of thirteen human P450 enzymes classified as 'orphans' because their substrate specificity and role in physiological function are not well characterized.[1] It is known that enzymes of family 4 are involved primarily in metabolism of endogenous fatty acids and steroids through ω-hydroxylation.[2] *CYP4V2* is an evolutionarily ancient, and remarkably conserved gene. In fact, within the CYP4 family, *CYP4V* is the only subfamily that includes both vertebrates and invertebrates.[3] There is such a high degree of sequence conservation that *CYP4V2* has more sequence homology (65% similarity, 45% identity) with the ortholog found in *C. elegans* than with other mammalian *CYP4* genes.[4] *CYP4V2* is also functionally conserved, as described by a study in *C. elegans* showing that lack of functional *Cyp31a2* or *Cyp31a3*, the homolog of human *CYP4V2*, resulted in defective eggshell development due to inadequate lipid deposition.[5] It shares only 31-37% protein sequence homology to other CYP4 enzymes, below the classical 40% homology required for family inclusion, but it does exhibit preferential hydroxylation of fatty acids at the ω position, the characteristic function of CYP4 isozymes.[6,7] Studies confirm CYP4V2 has specificity for saturated, medium-chain fatty acids that are 12 to 16 carbons in length.[8] Longer substrates are also metabolized, with known ω-hydroxylase activity for the docosanoids eicosapentaenoic acid (EPA, C20:5(n-3)) and docosahexaenoic acid (DHA, C22:6(n-3)) with kinetics comparable to CYP4F2.[9] CYP4V2 is ubiquitously expressed, including liver and ocular tissues, and is believed to play a role in lipid homeostasis.[1,8] This notion is supported by the evidence of substrate specificity, as well as dyslipidemia associated with changes in the expression or function of CYP4V2 or its orthologs.[10-14]

In 2004, researchers at the National Eye Institute identified a mutation in the 'orphan' cytochrome P450 4V2 (*CYP4V2*) gene in patients with Bietti's crystalline dystrophy (BCD), a rare, degenerative, blinding retinal disease.[15] While the enzyme is ubiquitously distributed, expression in the eye is highest within RPE cells, with weaker expression in the cornea.[9,16] To date, over 60 mutations have been identified in BCD patients, with at least one mutation in each of the gene's 11 exons.[17-41] Genotype analysis has shown the most common pathologic *CYP4V2* mutation is c.802-8_810del17insGC, which results in skipping Exon 7, though other mutations in each exon are also associated with the disease.[18,23,34] In genetic studies aside from BCD, a common polymorphism (minor allele frequency 45%) in *CYP4V2* has been associated with deep vein thrombosis (rs13146272; Q259K),[42,43] and expression of CYP4V2 has been inversely correlated with tumor grade in breast cancer.[44] This chapter provides an introduction to CYP4V2, describes the anatomy and physiology of the human eye, and the pathophysiology of Biettis' crystalline dystrophy

1.2 Anatomy and Physiology of the Eye

1.2.1 Structure of the Eye

The human eye is an exquisite organ system that is solely responsible for vision. The eye is roughly spherical in shape, with an average axial diameter of 24.2mm in adults.[45] Figure 1-1 illustrates the basic structure of the eye, as well as the complexity of the retina and cornea.[46] Structurally, the eye is mostly hollow, filled with the vitreous humor, a viscous fluid that maintains the globe shape, maintains optical clarity between the lens and retina, and acts as a conduit for metabolic needs of the cells in the lens and other anterior structures.[47] The vitreous humor is mostly acellular, and is composed of over 98% water hydrating a dilute extracellular

network of unbranched collagen fibrils. The eye is generally classified into two structural categories: the anterior chamber, including the cornea, lens, iris, and ciliary body; and the retina, which is located at the posterior of the eye.

The sclera is the white, protective outer layer of the eye that consists primarily of collagen and forms an elastic structure that helps to maintain the overall shape of the globe.[48] The tissue is rigid enough to withstand intraocular pressure, and also serves to protect the vulnerable internal tissues of the eye from damage and environmental exposure. The tissue is opaque, which also aids in preventing light scatter that could disrupt the retinal image. The choroid is the highly vascular layer resting just inside the sclera, and is responsible for facilitating blood flow to ocular tissues.[49] On the interior surface of the choroid, the Bruch's membrane provides structural support, and comprises the basement membrane of retinal tissue (Figure 1-1).

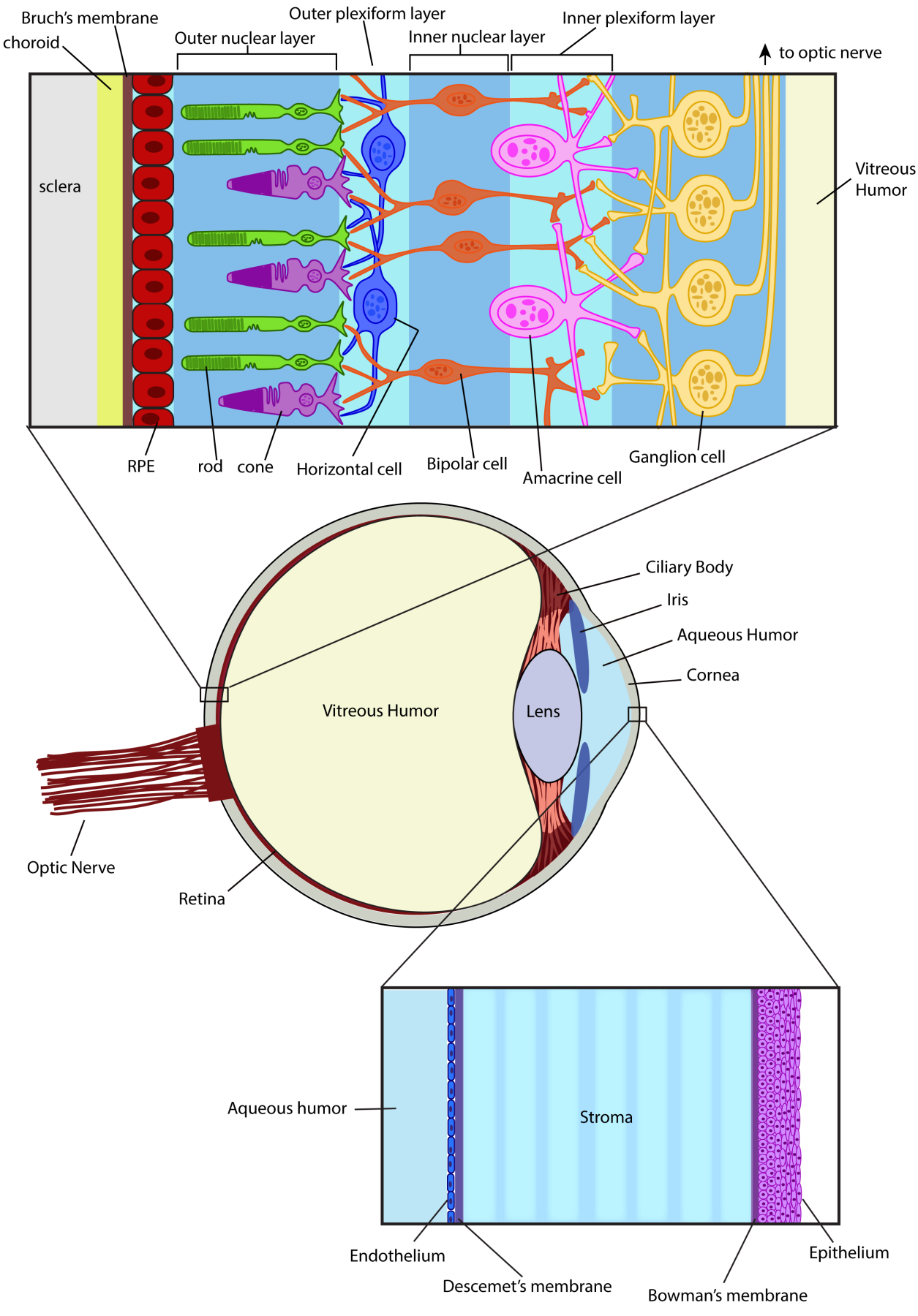
Bruch's membrane
choroid
Outer plexiform layer
Outer nuclear layer
Inner nuclear layer
Inner plexiform layer
to optic nerve
sclera
Vitreous Humor
RPE
rod
cone
Horizontal cell
Bipolar cell
Amacrine cell
Ganglion cell
Ciliary Body
Iris
Aqueous Humor
Cornea
Vitreous Humor
Lens
Optic Nerve
Retina
Aqueous humor
Stroma
Endothelium
Descemet's membrane
Bowman's membrane
Epithelium

Figure 1-1. Anatomical structure of the retina and cornea. The retina (upper blowout panel) is a complex tissue comprised of layers of cells built on the structural foundation of the sclera, choroid and Bruch's membrane. The retinal pigmented epithelial (RPE) cells provide a base layer to support the structure and function of photoreceptor cells (rods and cones) located in the outer nuclear layer. When light enters the eye, it penetrates the retinal tissue and is absorbed by photoreceptor cells where it is converted into an electrical signal. A series of nerve-type cells (horizontal, bipolar and amacrine cells) form the outer plexiform, inner nuclear and inner plexiform layers, and are responsible for transmitting the electrical signal to the ganglion cells in the innermost layer of the retina. Ganglion cells connect to the optic nerve and transmit the visual signal to the brain. The cornea (lower blowout panel) consists of an endothelial layer of cells in contact with the aqueous humor of the anterior chamber. The stroma is located between Descement's membrane on the endothelial side, and Bowman's membrane on the epithelial side. The epithelial layer of cells makes up the surface of the cornea. Reproduced with permission from reference [46].

1.2.2 The Retina

The cells of the retina are complex and distinctive from many other cell types. The retina is made of an intricate, highly organized layer of cells built on the structural foundation of the Bruch's membrane (Figure 1-1).[46,50] The retinal pigmented epithelial (RPE) cells comprise the base layer to support the structure of the neural retina.[51] RPE cells form a single layer of hexagonal-shaped cells that are bound by tight junctions and have a functional interaction with photoreceptor cells (rods and cones) located in the outer nuclear layer. One of the primary functions of RPE cells is to absorb scattered light within the eye to enhance visual clarity. Pigment granules within the cells provide a non-reflective surface to capture photons that are not absorbed by the photoreceptor cells.[51] Irradiation from visible light also generates heat that is absorbed by melanocytes and the highly perfused vasculature in the choroid helps dissipate the built up heat.

Tissues in the eye experience a high level of photo-oxidative stress by absorbing and transforming energy from visible light.[51] This photo-oxidation is damaging to delicate photoreceptor cells. A common cellular defense against oxidative damage is the enzyme

glutathione that scavenges free radicals and other reactive species.[52] Glutathione is abundantly present in the retinal pigmented epithelial cells, but is nearly absent in the outer segments of photoreceptor cells, where most photo-oxidation occurs.[53] One significant defensive process is to shed the damaged outer segment membranes. Once shed, the segments undergo phagocytosis by the RPE cells, where they are recycled into component parts to renew photoreceptor cells. The eye is a physiologically isolated system, so the RPE cells also play a critical role in delivering nutrients and water from the blood to internal ocular tissues.[51] Similarly, the RPE cells contribute to detoxification by transporting endogenous or xenobiotic compounds out of the eye for elimination through the blood.

Photoreceptor cells form the deepest layer of the retina, and have a functional interaction with the RPE layer. The majority of photoreceptors are rods (80%), with only approximately 20% cones. Photoreceptors are among the most specialized cells responsible for vision.[50] Rods and cones transform visible light, via phototransduction, into electrical impulses that are recognized and transmitted through neural pathways to the visual cortex of the brain where a visible image is registered. From the photoreceptors, the electrical signals travel through the network of cells in the neural retina. These include the horizontal cells, bipolar cells, and amacrine cells, which function similarly to other neural cells in signal transduction. Ganglion cells then gather all signals to transmit through the optic nerve to the brain (Figure 1-1). The function of the visual cycle is described in more detail in Section 1.2.4 below.

1.2.3 Anterior Eye

The anterior chamber of the eye is a region at the front of the eye filled with the aqueous humor, and includes the structures externally visible, and is separated from the vitreous humor and posterior region of the eye by the iris, lens and musculature that controls focus (Figure 1-1).

The cornea is the optically clear tissue layer located at the front of the eye. The cornea provides a protective barrier for internal tissues, and also is the optical "window" through which light passes on its path to the retina.[54] To maintain optically clarity, the cornea is made up of several layers of specialized cells and proteins that persist in a state of relative dehydration, and is completely devoid of vasculature.

The iris is the pigmented ring of musculature that expands and contracts based on light exposure to define the size of the pupil. When light travels through the pupil, it strikes the lens, which is responsible for focusing light rays into a cogent image on the retinal surface.[55] The lens is a crystalline structure located posterior to the iris and suspended in place by fibers from the ciliary body. The lens epithelium, or capsule, includes actively dividing cells that form new lens fibers. These new lens fibers populate the outer layers of the lens, while compressing the older fibers into the nucleus. The lens is avascular, so must derive nutrients from the aqueous humor. The lens is able to focus by changing shape through influence by the ciliary body.[55]

1.2.4 Physiology of Vision

The process of vision begins when visible light enters the eye through the cornea, and is focused by the lens to strike the retina.[51] There are two main photosensory cells of the retina, the rods and cones.[56] Rods are extremely sensitive and are designed for detection of as little stimulus as a single photon for low-light vision, while cones are less sensitive with higher temporal resolution to mediate daylight vision and color vision. Photoreceptor cells are structured in three primary functional sections: outer segment, inner segment including the cell body, and synaptic terminal (Figure 1-2). The outer segment consists of densely stacked membrane layers containing an abundance of visual pigment, including rhodopsin in rods, and cone pigment in cones. This is the primary location of phototransduction for image-forming vision, while

intrinsically photosensitive retinal ganglion cells mediate non-image-forming vision.[56] The phototransduction process differs slightly between rods and cones, particularly in the recovery stage after signal transduction, but the visual cascade in cones is not as clearly understood.[51]

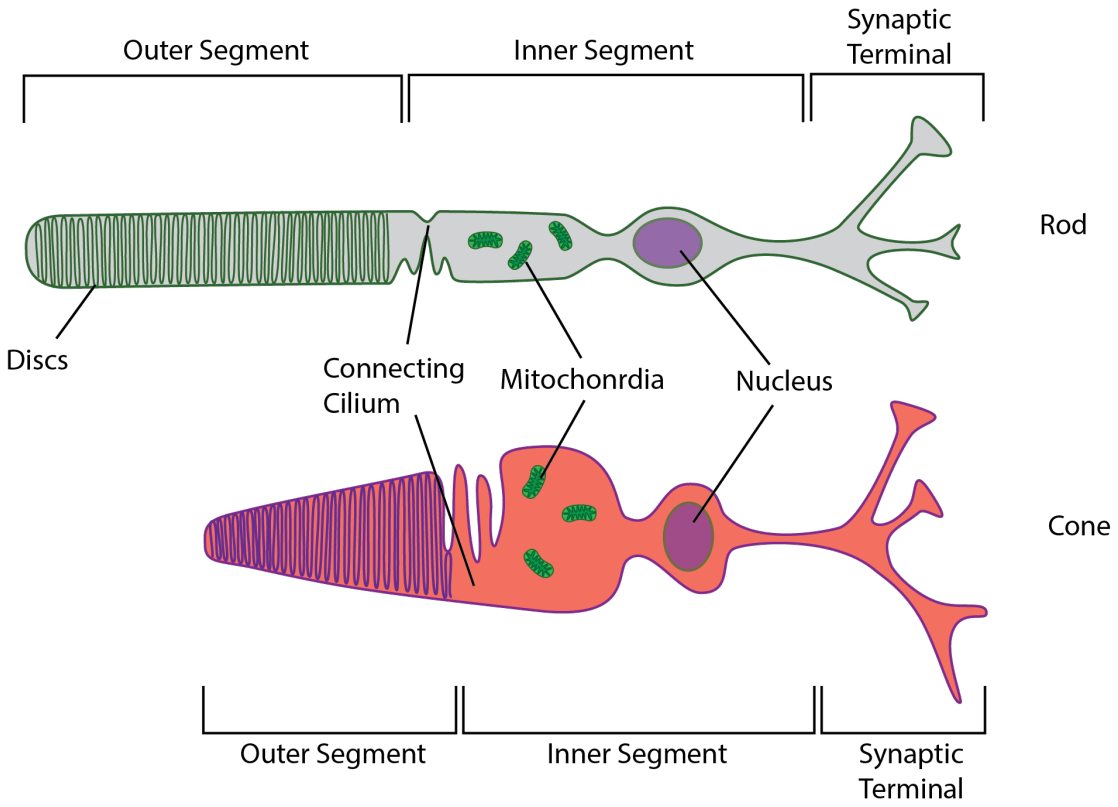

Figure 1-2. Anatomy of photoreceptor cells.

The process of phototransduction is mediated by a G-protein-signaling pathway in the photoreceptor cells (Figure 1-3).[56] A photon absorbed in a rod interacts with rhodopsin and isomerizes 11-*cis* retinal into all-*trans* retinal in the outer segment.[57] Rhodopsin then changes conformation and splits into opsin and all-*trans* retinal. The opsin is then enzymatically active, and in turn activates transducin, the regulatory G-protein involved in the visual cycle. Transducin then activates phosphodiesterase (PDE), which hydrolyzes cyclic guanosine monophosphate (cGMP) into 5'-GMP, and the resulting decrease in cGMP concentration causes cGMP-gated

sodium channels located in the plasma membrane to close. Closure of the channel causes membrane hyperpolarization by blocking the influx of cations, decreasing the release of dark glutamate at the synaptic terminal. This results in generation of an electrical signal that is transmitted through the other cells of the neural retina, through the optic nerve, and to the visual cortex.[56]

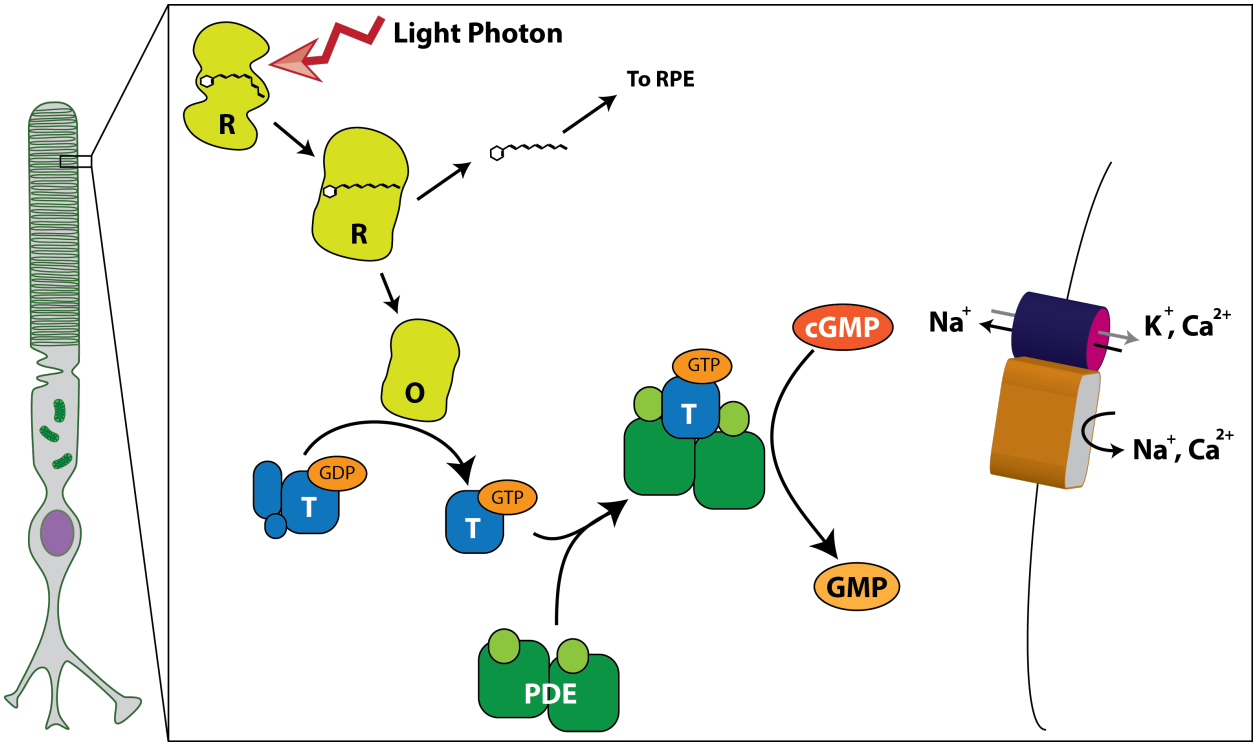

Figure 1-3. Phototransduction. Physiology of phototransduction for visual function in the human eye. A light photon stimulus interacts with rhodopsin (R), converting 11-cis retinal to all-trans retinal, which dissociates from the activated opsin (O) and is transported to the retinal pigmented epithelium for recycling. Opsin activates transducin (T), which activates phosphodiesterase (PDE), and in turn hydrolyzes cyclic guanosine monophosphate (cGMP) to guanosine monophosphate (GMP). Decrease in intracellular cGMP closes the cGMP-gated sodium channel resulting in membrane hyperpolarization and an electrical signal that is transported through the neural retina to the visual cortex in the brain.

After signal generation, the cell must recover and return to a resting state in anticipation of the next photon stimulus (Figure 1-4).[51,56] As part of the recovery process, the isomerized all-*trans* retinal must be restored to the original 11-cis retinal form. First, all-*trans* retinal is reduced

by retinol-dehydrogenase to all-*trans* retinol, which is then transported from the photoreceptor cell to the RPE. Once in the RPE cells, all-*trans* retinol undergoes esterification by lecithin:retinol transferase (LRAT), re-isomerization by RPE65, and oxidation back to 11-cis retinal by 11-cis retinol dehydrogenase (RDH).[51] The inactivated 11-cis retinal is transported back to the photoreceptor outer membrane where it is reincorporated into rhodopsin. In the photoreceptor cell, activated rhodopsin undergoes phosphorylation by rhodopsin kinase (GRK1) to lower the level of activation, and completely inactivated through binding by arrestin (Arr1). PDE is deactivated through hydrolysis of bound guanosine triphosphate (GTC), thus terminating the activation of cGMP. The intracellular concentration of cGMP then increases, resulting in re-opening of cGMP-gated sodium channels and depolarization of the membrane.

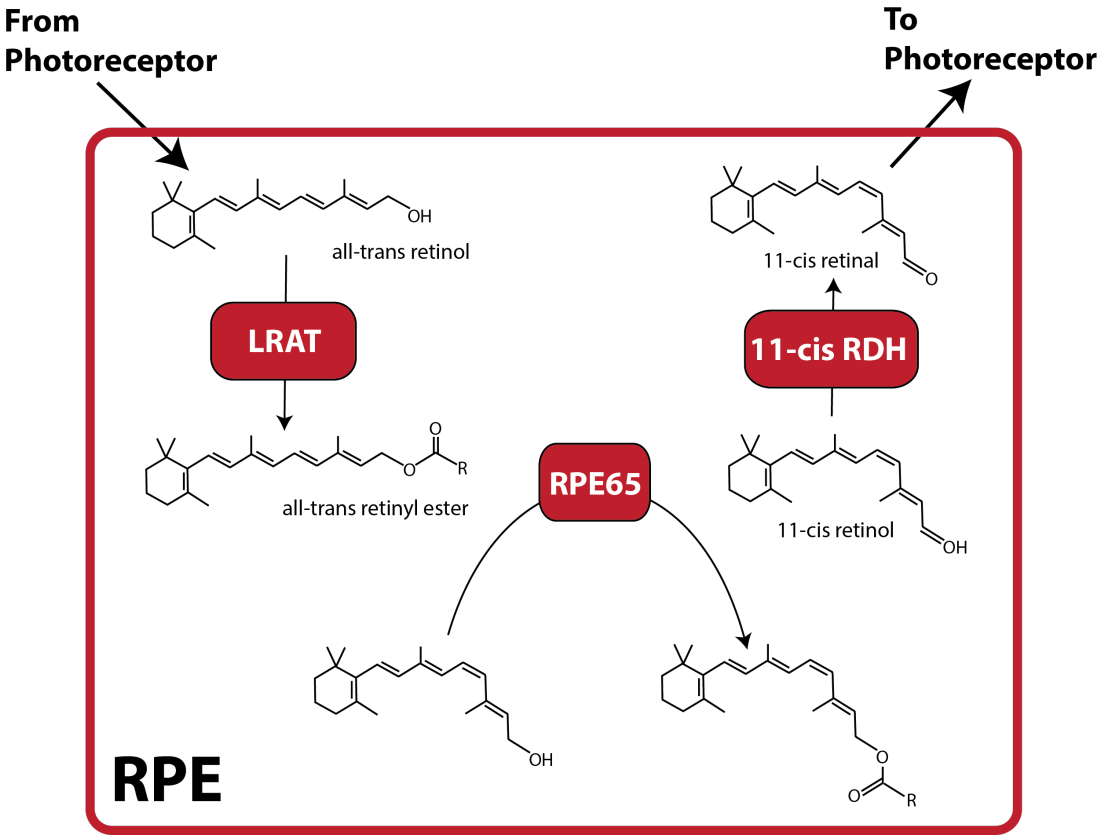

Figure 1-4. Phototransduction resolution**.** Physiology of resolution after phototransduction in the human visual cycle. LRAT = lecithin:retinol transferase; 11-cis RDH = 11-cis retinol dehydrogenase

The phototransduction process in cones differs somewhat from that in rods due to some fundamental physiological differences in structure and function, although it is not well defined in cones. Cones have been estimated to be many 100-fold less sensitive than rods, but also recover approximately 10-fold faster.[57] One difference in the cone visual cycle, when compared to that of rods, is in the isomerization process that resolves the signal cascade. It has been shown that all-*trans* retinol is transported to Müller cells, rather than RPE cells, for isomerization back to 11-*cis* retinol for transport back into the cones for NADP-dependent oxidation to 11-*cis* retinal and ready for the next signaling cascade. Therefore, in contrast to the one-step process in rods that occurs in RPE cells, the isomerization in cones is a two-step process occurring in the Müller cells, with the final oxidation step occurring back in the cones.[57]

1.2.5 Blood-Retinal Barrier

One important feature of the eye is the presence of the blood-retinal barrier (BRB). The BRB is composed of two main components: inner BRB and outer BRB.[45,58,59] The primary functions of both the inner and outer BRB are to maintain ocular homeostasis, and to protect vulnerable ocular tissues from both xenobiotic and endogenous compounds present in the blood. These are accomplished through several mechanisms including the presence of intracellular tight junctions, and transporters that control flow of fluids and compounds in and out of the eye. The BRB also has substantial implications in drug delivery and treatment options for ocular diseases, as the BRB is intentionally difficult to penetrate. Potential solutions to overcoming the challenges of drug delivery are explored in the Future Directions section of this document (Chapter 5). Both the BRB and the role of ocular transporters are described in detail below.

1.2.6 Ocular Transporters

Despite the lack of availability (in most cases) of monospecific antibodies, access to gene sequence information and to RT-PCR techniques has facilitated measurement of the transcriptional levels of drug transporters in the eye. A recent study used high-throughput RT-PCR techniques to screen ocular tissues for expression of genes from the solute carrier (SLC) and ATP binding cassette (ABC) families of transporters, in addition to several metabolic enzymes.[60] Overall, expression was highest in retinal and corneal tissues compared to other substructures, and in both tissues SLC family transporters were the most prevalent with 68% of expression in the cornea and 75% in the retina attributed to SLC transporters. Among the most highly expressed genes, more nutrient transporters were present in the retina compared to cornea (46% versus 38%, respectively), and more drug transporters were identified in the cornea (29%) compared to the retina (13%). In the cornea, ABC transporters represented 16% of expressed transporters, nuclear receptors and transcription factors accounted for 9%, and Phase I and II enzymes represented 7% of the evaluated gene expression. In the retina, ABC transporters represented 9% of expressed transporters, nuclear receptors and transcription factors accounted for 6%, and Phase I and II enzymes represented 10% of the evaluated gene expression.[60]

The human cornea expresses both uptake and efflux transporters. RT-PCR studies have detected transcripts for numerous uptake transporters, including several solute carriers (SLC), the amino-acid transporter $B^{0,+}$ ($ATB^{0,+}$) and the large, neutral, amino-acid transporter 1 (LAT1), and their functional activities have been confirmed in transporting L-arginine and L-phenylalanine across isolated rabbit cornea.[61,62] Figure 1-5 illustrates the localization of transporter proteins in ocular tissues as determined by RT-PCR evaluation of gene transcripts. The uptake transporters from the family of solute carriers expressed in the cornea include peptide transporters 1 and 2 (PEPT1, PEPT2), organic cation transporters 1, 2, and 3 (OCT1, OCT2,

OCT3), organic cation/carnitine transporter 2 (OCTN2), organic anion transporters 1 and 3 (OAT1, OAT3), multidrug and toxin exclusion transporters 1 and 2 (MATE1, MATE2), organic anion transporting peptide 1A2, 1B1, 1B3, and 2B1 (OATP1A2, OATP1B1, OATP1B3, OATP2B1), and Na^+-taurocholate cotransporting polypeptide (NTCP). In terms of efflux, the ATP-binding cassette transporters B1 (ABCB1, multiple drug resistance 1 or P-glycoprotein), C1 (ABCC1 or multidrug resistance-associated protein 1, MRP1), C2 (ABCC2 or MRP2), C3 (ABCC3 or MRP3), C4 (ABCC4 or MRP4), C5 (ABCC5 or MRP5), C6 (ABCC6 or MRP6) and breast cancer resistance protein (BCRP) are expressed in human cornea and in Statens Seruminstitut rabbit corneal cells.[63-66] However, the quantitative data obtained from these corneal expression studies often varies widely for a given transporter, due possibly to differences in experimental methods, but perhaps more likely to the varying clinical background and post-mortem status of the particular tissue samples that were used. There is limited information regarding subcellular localization of transporters within ocular tissues; however, a recent study examined cultured rabbit primary corneal epithelial cells and determined the efflux transporter P-glycoprotein and PEPT1 were present in the mitochondrial membranes.[67] A high throughput RT-PCR analysis of gene transcripts suggests organic cation transporter 2 (OCT2), peptide transporter 1 (PEPT1), and organic anion transporting polypeptides 1A2 and 1B3 (OATP1A2, OATP1B3) are also present in the retina (Figure 1-5).[60]

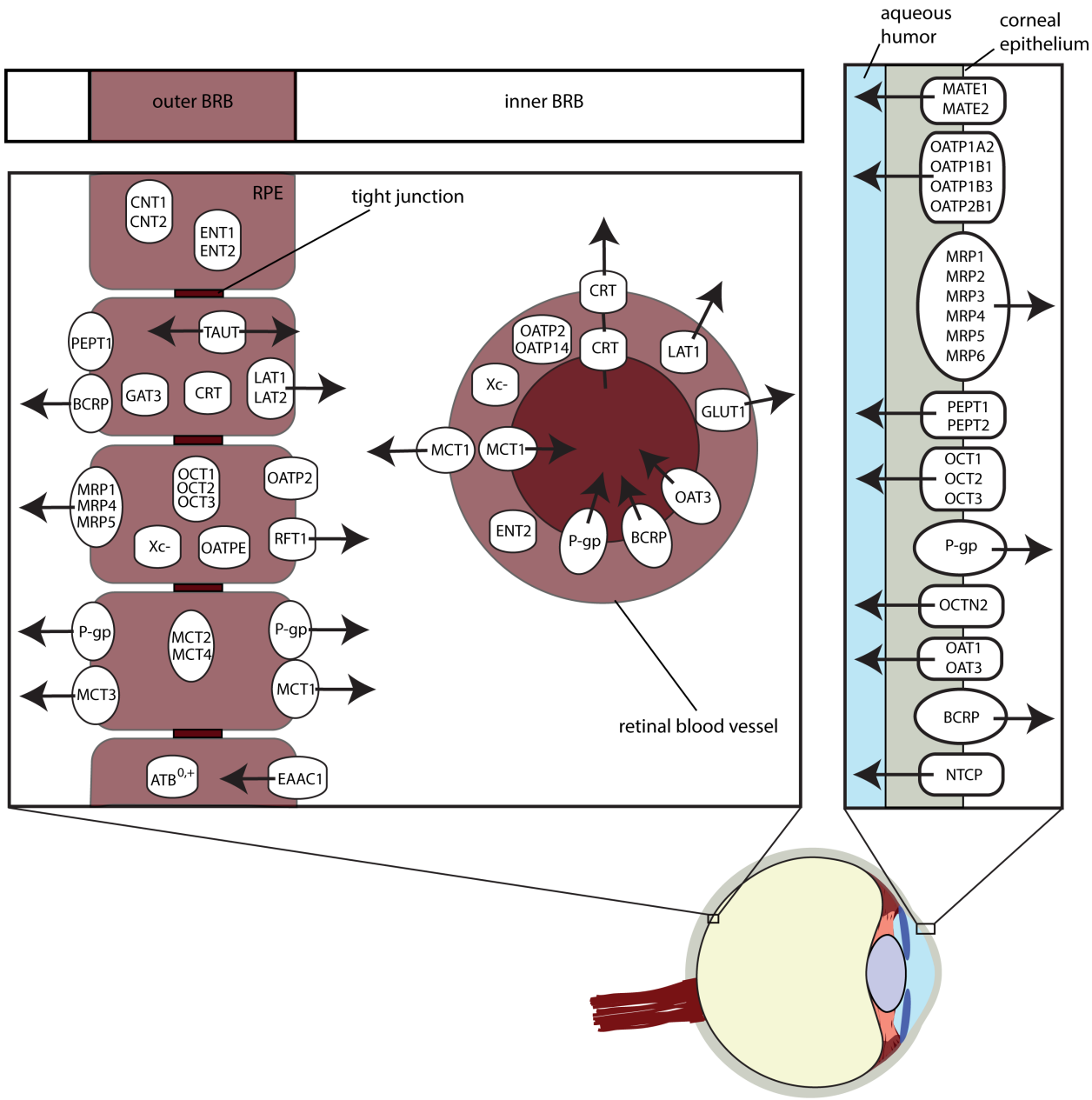

Figure 1-5. Ocular transporters. Localization of uptake and efflux transporters in the corneal epithelium, outer blood retinal barrier (BRB) and inner BRB. The outer BRB includes the retinal pigmented epithelium (RPE) that is bound by tight junctions to provide a physical barrier between systemic circulation and the photoreceptor cells and neural retina. The inner BRB is formed by the vasculature that serves the neural retina and acts as a gatekeeper for nutrient delivery, toxin removal and prevention of endogenous and exogenous compounds that do not belong in the eye from reaching the sensitive retinal tissue. Approximate cellular localization is illustrated, along with proposed functional direction of transport. Transporters that have been identified to be present in ocular tissue, but for which exact localization or function has not been confirmed are placed within the cell without directional arrows. Uptake transporters: Amino-acid

transporter $B^{0,+}$ ($ATB^{0,+}$), nucleoside transporters (CNT, ENT), creatinine transporter (CRT), gamma-aminobutyric acid transporter (GAT), facilitative glucose transporter (GLUT), large, neutral amino-acid transporter (LAT), multidrug and toxin exclusion transporters (MATE), monocarboxylate transporter (MCT) Na^+-taurocholate cotransporting polypeptide (NTCP), organic anion transporter (OAT), organic anion transporting peptide (OATP), organic cation transporters (OCT), organic cation/carnitine transporter (OCTN), peptide transporter (PEPT), reduced folate transporter (RFT), taurine transporter (TAUT), Na^+-independent glutamate/cysteine exchange transporter (Xc^-). Efflux transporters: breast cancer resistance protein (BCRP), excitatory amino-acid transporter (EAAC1), multidrug resistance-associated protein (MRP), monocarboxylate transporter (MCT), multiple drug resistance protein/P-glycoprotein (P-gp). Reproduced with permission from reference [46].

Retinal tissue is highly vascularized, and the sensitive tissues are protected from systemic endogenous and exogenous compounds by the blood-retinal barrier (BRB), similar in structure and function to the blood-brain barrier. There are two main components to the BRB: the outer BRB consists of the retinal pigmented epithelial (RPE) cells with tight junctions that provide a physical barrier to neuroretinal tissue, and the inner BRB is defined by the vessel endothelium of the intraretinal vasculature.[68] Figure 1-5 illustrates transporters localized in the inner and outer BRB. In the RPE cells of the outer BRB, the high affinity excitatory amino acid transporter 1 (EAAC1) facilitates removal of extracellular glutamate, an excitatory neurotransmitter used by cells of the neural retina that is neurotoxic in high concentrations.[68] Other amino acid transporters localized in the RPE include neurotransmitter transporters from the SLC6 family (TAUT, system β) that are responsible for transport of taurine, the most abundant retinal amino acid with transport direction dependent upon taurine and ion concentration gradients. Creatinine transporter (CRT) has been identified in rat retinal endothelium, and GAT3 transports GABA, the most abundant inhibitory neurotransmitter found in retinal tissues. The amino-acid transporter $B^{0,+}$ ($ATB^{0,+}$) has been detected in RPE cells, but the function is still unknown.[68] The large, neutral, amino-acid transporter 1 (LAT1) is involved in uptake of L-phenylalanine in RPE-19 cells, and LAT2 is believed to mediate transport of leucine. The Na^+ independent

glutamate/cysteine exchange transporters (Xc^-) are present in outer BRB as well as inner BRB to support glutamate homeostasis.[68] Monocarboxylate transporters 1 through 4 (MCT1, MCT2, MCT3, MCT4) facilitate uptake of lactate in ARPE-19 cells and isolated bovine RPE, organic cation transporters 1 through 3 (OCT1, OCT2, OCT3) have been identified in RPE cells which may affect drug transport, and folate uptake is medicated by reduced folate transporter 1 (RFT-1).[60,68] Nucleoside transporters ENT1, ENT2, CNT1, and CNT2 have been identified in immortalized rate retinal capillary endothelial cells (TR-iBRB), as well as organic anion transporting polypeptides OATP2, OATPE, and OATP12. Efflux transporters expressed in the outer BRB include multidrug resistant protein 1 (MDR1, P-gp), and the ATP-binding cassette transporters MRP1, MRP4, MRP5, and the breast cancer resistance protein (BCRP).[60,68]

In the inner BRB, transporters are located in the vascular endothelium of vessels in the neural retina. The retinal capillary system includes many of the same transporters that have been identified in the outer BRB. D-Glucose is transported by facilitative glucose transporter 1 (GLUT1) from the blood as the primary energy source for retinal tissue. Creatinine transporter (CRT) has been identified in rat retinal vessels, as well as the large, neutral, amino-acid transporter 1 (LAT1). Monocarboxylate transporter 1 (MCT1) facilitates movement of lactate in between blood and retina through the inner BRB.[68-70] The Na^+ independent glutamate/cysteine exchange transporters (Xc^-) are present in inner BRB to support glutamate homeostasis, and organic anion transporting polypeptide 2 (OATP2), and RNA from OATP14 was detected in rat retinal vessels. Efflux transporters expressed in the inner BRB include multidrug resistant protein 1 (MDR1, P-gp), organic anion transporter 3 (OAT3), and breast cancer resistance protein (BCRP).[68-70]

In the retina, multidrug resistance protein 1 (MRP1), PEP2, OCT1 and organic cation/carnitine transporter (OCTN1 and OCTN2) exhibited higher expression levels in the eye than the liver, and the expression levels of MDR1 and BCRP were approximately 4-fold lower than those on the liver.[71] Interestingly, there is a good consensus on MDR1 and BCRP expression levels in multiple reports[60,66] although, compared to the data on the cornea, limited numbers of comparator studies are available. In addition, MRPs and LRP retinal expression of MRPs were observed.[60,66,71] In human immortalized retina pigmented epithelial cells (ARPE-19), transcripts for the uptake transporters, excitatory amino-acid transporter C1 (EAAC1), taurine transporter (TAUT), LAT2, creatinine transporter (xCT), peptide histidine transporter 1 (PHT1), monocarboxylate transporters 1, 3 and 4 (MCT1, MCT3 and MCT4), reduced-folate transporter (RFT) and organic cation transporter 3 (OCT3) have all been detected.[68]

It seems plausible that efflux and uptake transporters in the eye could have evolved to perform both an ocular barrier function and to control xenobiotic pharmacokinetics because certain transporters show mRNA expression levels comparable to those in the liver, small intestine and kidney,[71] organs that play significant roles in drug disposition. Transporters have an important role in ocular drug absorption, distribution and clearance, but the degree of involvement by each transporter and subcellular localization of those transporters remains to be elucidated. This requires more comprehensive functional studies together with robust protein quantitation data that are becoming increasingly easy to obtain for drug transporters using SILAC-based mass spectrometry techniques.[72]

1.3 Bietti's Crystalline Dystrophy

Bietti's crystalline dystrophy (BCD) is a rare, degenerative retinal disease that belongs to the family of inherited retinal degenerations known collectively as retinitis pigmentosa and allied

disorders. BCD was first identified in 1937 by Dr. G. B. Bietti, an Italian ophthalmologist who treated three patients with progressive night blindness.[73] These patients developed sparkling crystalline deposits in their corneas and posterior pole of their retinas, leading to declining vision that did not respond to traditional vision correction.[73-75] BCD is regarded as rare with a prevalence estimated at 1:67,000, although it may be underdiagnosed.[76,77] There is no available treatment, and patients will eventually become completely blind.

The symptoms and clinical features of BCD are similar to many forms of retinitis pigmentosa, characterized by gradual constriction of the visual field, night blindness, abnormal retinal electrophysiology, altered visual acuity, and often colorblindness.[17,78] Structural findings are also typically similar to retinitis pigmentosa including degeneration of the retinal pigment epithelium (RPE), pigment clumping, and sclerosis of the choroid.[17,79] The hallmark characteristics that differentiate BCD from other retinal disorders are formation of yellow-white crystals in the retina and sometimes in the cornea.

1.3.1 Clinical Characteristics

There is wide variability in phenotype among BCD patients with differing disease severity and rate of progression. Visual acuity is often diminished, but there are reports of patients with best corrected vision within a completely normal range despite symptoms such as nyctalopia or blurred vision, the presence of characteristic crystalline deposits, and signs of retinal degeneration.[80,81] Electroretinography (ERG) examination typically shows decreased amplitudes of b-waves from both rods and cones,[82] however in one study evaluating 15 BCD patients, more than 50% had recordable standard ERG, and 2 were within normal limits 20 years after initial BCD diagnosis, suggesting ERG may not always correlate with disease progression.[83] In one case report, standard ERG was normal, but multifocal ERG showed

depressed central responses consistent with the macular lesion identified by optical coherence tomography (OCT).[84] This suggests the neuroretinal cells were still functioning in this patient despite RPE degeneration. Conversely, there are reports in which patients have severely diminished visual acuity such that only the ability to perceive light remains.[85]

A normal, healthy eye has a visual field that includes both central vision and peripheral vision. Central vision extends approximately 30 degrees from the point of central fixation, and in peripheral vision the field extends 100 degrees laterally, 60 degrees medially and upward, and 75 degrees downward.[86] Similar to visual acuity, there is a wide variation in severity of visual field constriction among BCD patients. Case reports show patients with normal visual field, especially during earlier stages of the disease, as well as patients with severe constriction (only 5-10° remaining).[85]

Optical coherence tomography (OCT) images of BCD patients have revealed not only the presence of crystalline deposits in retinal and corneal tissue,[19] but also that in some cases the cellular layers of the retina become disturbed and disorganized over time.[80,82,87] As the disease progresses, fundus autofluorescence often shows a patchy mosaic of hypofluorescence, indicating possible atrophy of the retinal pigmented epithelium (RPE) or neovascularization, and hyperfluorescence, indicating the possible presence of drusen or other degeneration. These imaging results are indicators of retinal degeneration.

1.3.2 Dyslipidemia in Bietti's Crystalline Dystrophy

Clinical systemic dyslipidemia in BCD patients has been reported, possibly due to nonfunctional CYP4V2 enzymes. For example, lymphocytes from BCD patients displayed a lack of two fatty acid-binding proteins with molecular weights of 32-kDa and 45-kDa that are expressed in control subjects.[88] Further analysis showed that the 32-kDa protein preferentially

bound docosahexaenoic acid (DHA, C22:6), α-linolenic acid (ALA, C18:3), and palmitic acid (C16:0).[88] Abnormal fatty acid processing and storage has been identified in lymphocytes and fibroblasts of BCD patients, including decreased conversion of fatty acid precursors into n-3 polyunsaturated fatty acids (PUFAs), and increased incorporation of ALA into triglycerides.[13] Further, fatty acid profiling in BCD serum showed an abnormal composition of fatty acids and reduced activity of the Δ-9-desaturase regardless of *CYP4V2* genotype.[11] Lymphocytes and fibroblasts from three BCD patients revealed crystalline deposits, some resembling complex lipid deposits, although the crystal composition was not determined.[75] Similarly, the composition of ocular crystals that accrue in BCD has not been determined. Elucidation of the chemical nature of these crystals would be an invaluable step towards a biochemical understanding of BCD; however, the availability of this material from human subjects is extremely limited and analysis is further complicated by adventitious debris from macular degeneration often present in ageing patients. To understand the biochemical mechanism underlying this progressive blinding disease, we have cloned and expressed the human enzyme, demonstrating that, like other CYP4 enzymes, CYP4V2 characteristically catalyzes medium and long-chain fatty acid ω-hydroxylation reactions, despite sharing only 31-37% sequence homology to other CYP4 enzymes.[89]

1.4 Cytochrome P450 4V2 (CYP4V2) in Bietti's Crystalline Dystrophy

Cytochrome P450 4V2 (CYP4V2) is an 'orphan' member of the superfamily of heme-containing monooxygenase enzymes that is highly expressed in retinal pigmented epithelial (RPE) cells.[9,90] Family 4 are involved primarily in metabolism of endogenous fatty acids and steroids through ω-hydroxylation,[2] and while it shares only 31-37% protein sequence homology to other CYP4 enzymes, it does exhibit preferential hydroxylation of fatty acids at the ω position, the characteristic function of CYP4 isozymes.[2,91]

Studies in BCD have suggested abnormality in fatty acid processing, including DHA, may be a causal mechanism in the disease.[11,13,88] DHA synthesis is limited in mammals, and RPE cells have a critical function in DHA uptake, recycling, and delivery to rod inner segments.[92] DHA is essential in the structure of disk outer membrane phospholipid bilayers, but it also functions as a precursors to cytoprotective docosanoids, including Resolvin D1 (RvD1) and Protectin D1 (PD1)/Neuroprotectin D1 (NPD1), which are important anti-inflammatory and immunoregulatory signaling molecules.[93,94] Anabolism for both molecules is similar to formation of leukotriene B4 (LTB_4) from arachidonic acid via a lipoxygenase-dependent pathway. CYP4F3A can sequentially ω-hydroxylate LTB_4, resulting in inactivation. Thus, it is plausible that a comparable pathway of inactivation of resolvins and protectins may exist.[95] Data have shown that in a human RPE cell line (ARPE-19), CYP4V2 is the only CYP4 isozyme expressed, suggesting that RPE cells may require CYP4V2 for DHA-related signaling and local polyunsaturated fatty acid metabolism. This was confirmed by RNA-Seq analysis of ARPE-19 cells. Figure 1-6 describes a potential role for CYP4V2 in the arachidonic acid inflammatory pathway.

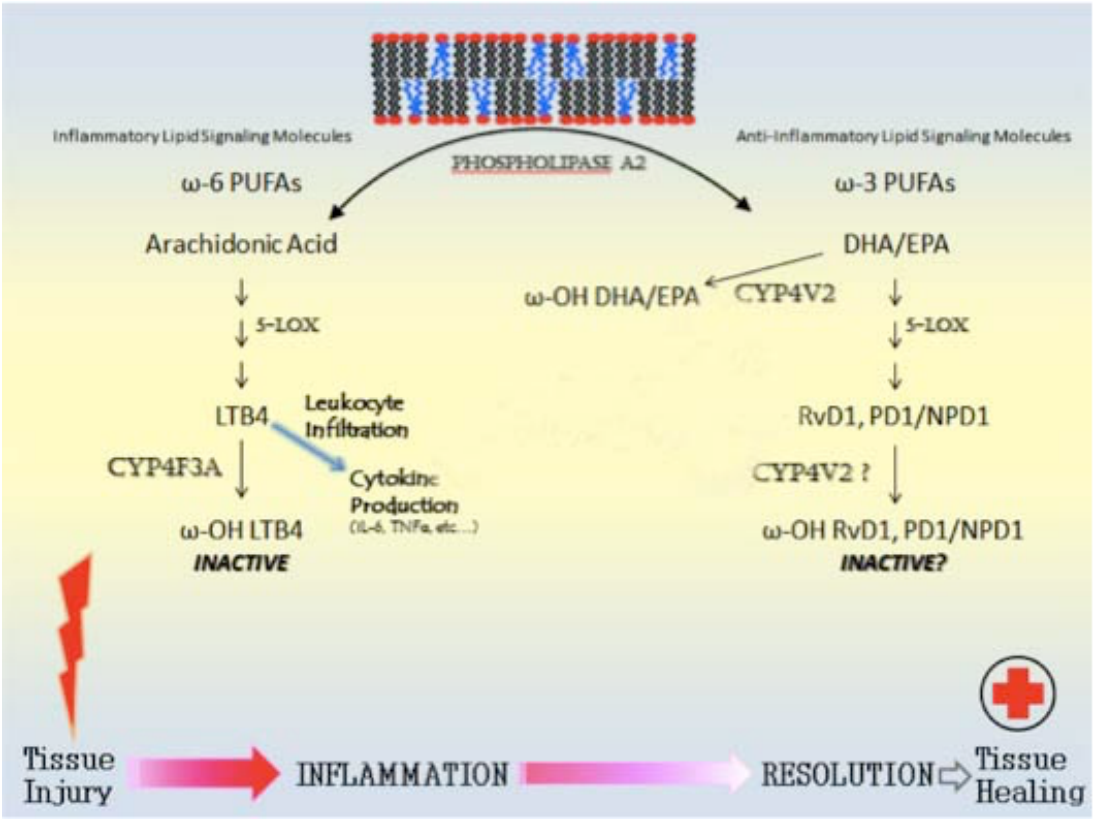

Figure 1-6. CYP4V2 in Inflammation. Potential roles for CYP4V2 in modulating the inflammatory pathway mediated by ω-6 and ω-3 polyunsaturated fatty acids (PUFAs). CYP4V2 is known to ω-hydroxylate medium-chain fatty acids, and active substrates include docosahexaenoic acid (DHA) and eicosapentaenoic acid (EPA). Both DHA and EPA are involved in the resolution stage of inflammation caused by acute tissue injury. If CYP4V2 is involved in this physiological function, it is possible that by inactivation of DHA and EPA through ω-hydroxylation, CYP4V2 may play a regulatory role in the resolution phase of inflammation.

1.4.1 CYP4V2 Genetic Mutations

To date, over 80 mutations have been reported in BCD patients, with at least one in each of its 11 exons (Figure 1-7**,** Table 1-1).[11,17,19,27,28,39,40,82-85,96-119] Genotype analysis has shown the most common pathologic *CYP4V2* mutation is c.802-8_810del17insGC, which results in deletion of Exon 7, though other mutations in each exon are also responsible for the disease.[79,113,115] There have been reports of individuals displaying the typical BCD phenotype, but for whom no *CYP4V2* mutations were identified. This suggests the possibility of pathogenic mutations that

occur outside the coding regions and are therefore not detected with standard primer-based polymerase chain reaction (PCR) techniques.[85]

The inheritance pattern of BCD is generally considered to be autosomal recessive, though some reports suggest possible haplo-insufficiency, in which a heterozygous carrier may display some phenotypic characteristics, though usually less severe or subclinical.[82] The likelihood of inheriting homozygous mutant alleles of this autosomal trait is increased in consanguineous pairings, such that both parents are heterozygous carriers at minimum or homozygotes with the disease. It has been estimated that 10.5% of children worldwide come from consanguineous parents, typically first cousins, and overall the risk of congenital disorders is increased by 2-4% over non-consanguineous offspring.[120] Consanguinity is not a requirement for developing the disease, as many cases have been reported with no evidence of consanguineous marriage in the immediate family.[74,75,106]

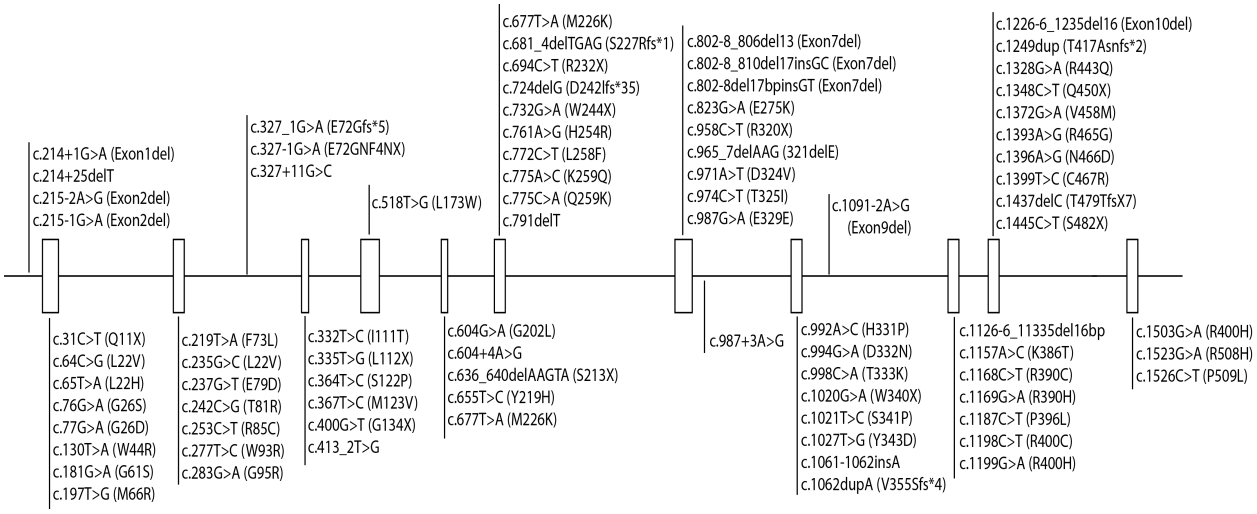

Figure 1-7. CYP4V2 Mutations.

Table 1-1. *CYP4V2* Gene Mutations Reported to Date

Mutation			Reference
Exon	**Nucleotide Change**	**Predicted Protein Change**	
1	c.31C>T	p.Q11X	*106*
1	c.64C>G	p.L22V	*39,102,106,111*
1	c.65T>A	p.L22H	*116*
1	c.76G>A	p.G26S	*83*
1	c.77G>A	p.G26D	*99,116*
1	c.130T>A	p.W44R	*17*
1	c.181G>A	p.G61S	*17*
1	c.197T>G	p.M66R	*99*
IVS1	c.214+1G>A	Exon1del	*115*
IVS1	c.214+25delT	Not available	*17*
IVS1	c.215-2A>G	Exon2del	*106,115,116*
IVS1	c.215-1G>A	Exon2del	*115*
2	c.219T>A	p.F73L	*40,106,112,116*
2	c.235G>C	p.L22V	*110*
2	c.237G>T	p.E79D	*17*
2	c.242C>G	p.T81R	*85*
2	c.253C>T	p.R85C	*111*
2	c.277T>C	p.W93R	*83*
2	c.283G>A	p.G95R	*40,99,105,106,111,116*
IVS2	c.327+1G>A	p.E72Gfs*5	*17*
IVS2	c.327-1G>A	p.E72GNF4NX	*17*
IVS2	c.327+11G>C	Not available	*99*
3	c.332T>C	p.I111T	17,82-85,98
3	c.335T>G	p.L112X	*111*
3	c.364T>C	p.S122P	*83*
3	c.367A>G	p.M123V	*17*
3	c.400G>T	p.G134X	*17*
3	c.413_2T>G	splicing acceptor	*106*
4	c.453A>C	p.T151T	*104*
4	c.518T>G	p.L173W	*28,107,116*
4	c.555A>T	p.A185A	*110*
5	c.604G>A	p.G202L	85
5	c.604+4A>G	splicing	85
5	c.636_640delAAGTA	p.S213X	*105*

Mutation			Reference
Exon	**Nucleotide Change**	**Predicted Protein Change**	
5	c.655T>C	p.Y219H	11,101
6	c.677T>A	p.M226K	*99*
6	c.681_4delTGAG	p.S227Rfs*1	*116*
6	c.694C>T	p.R232X	*83*
6	c.724delG	p.D242Ifs*35	*83*
6	c.732G>A	p.W244X	11,101,106
6	c.761A>G	p.H254R	*115*
6	c.772C>T	p.L258F	*109*
6	c.775A>C	p.K259Q	*39,83,104*
6	c.775C>A	p.Q259K	*103*
6	c.791delT	deletion	*106*
7	c.810T>G	p.A270A	*39,110*
7	c.802-8_806del13	Exon7del	*17*
7	c.802-8_810del17insGC	Exon7del	11,19,27,28,40,85,96,97,99-102,106-108,111-114,116-118
7	c.802-8del17bpinsGT	Exon7del	*116*
7	c.823G>A	p.E275K	*110*
7	c.958C>T	p.R320X	*106,115*
7	c.965_7delAAG	p.321delE	*116*
7	c.971A>T	p.D324V	11,101
7	c.974C>T	p.T325I	119
7	c.987G>A	p.E329E	*104*
IVS7	c.987+3A>G	Not available	*99*
8	c.992A>C	p.H331P	11,17,28,101,102,106,111,116
8	c.994G>A	p.D332N	*116*
8	c.998C>A	p.T333K	*99*
8	c.1020G>A	p.W340X	96,102,113
8	c.1021T>C	p.S341P	*17*
8	c.1027T>G	p.Y343D	*106*
8	c.1061-1062insA	insertion	*106*
8	c.1062dupA	p.V355Sfs*4	*40,116*
8	c.1062_1063dupA	p.Val354Serfs2x	*104*
IVS8	c.1091-2A>G	Exon9del	11,17,39,40,101-103,106,112,114,116
9	c.1126-6_11335del16bp	splicing site	*116*
9	c.1157A>C	p.K386T	*27*
9	c.1168C>T	p.R390C	*102,116-118*

Mutation			Reference
Exon	Nucleotide Change	Predicted Protein Change	
9	c.1169G>A	p.R390H	83,115,116
9	c.1187C>T	p.P396L	101,106
9	c.1198C>T	p.R400C	11,85,101
9	c.1199G>A	p.R400H	11,101,111,112
10	c.1226-6_1235del16	Exon10del	111,115
10	c.1249dup	p.Thr417Asnfs*2	85
10	c.1328G>A	p.R443Q	83
10	c.1348C>T	p.Q450X	28
10	c.1372G>A	p.V458M	98
10	c.1393A>G	p.R465G	83,85,99
10	c.1396A>G	p.N466D	
10	c.1399T>C	p.C467R	39
10	c.1437delC	T479TfsX7	112
10	c.1445C>T	p.S482X	27
11	c.1503G>A	p.R400H	99
11	c.1523G>A	p.R508H	17
11	c.1526C>T	p.P509L	100
	Full Gene Deletion		85

1.5 Summary and Research Aims

The eye is a complex organ system designed to convert visual stimulus in the form of visible light photons into electrical signals that are resolved in the visual cortex of the brain into a visual image. Vision impairment has a significant impact on quality of life and normal daily functioning.[121-123] Studies have shown that a large proportion of people with vision impairment report difficulty in most measures of quality of life, including mobility, usual activities, and levels of anxiety or depression. Furthermore, patients with chronic conditions reported lower quality of life with concomitant visual impairment.[122,123] A study assessing the quality of life in patients with retinitis pigmentosa showed that overall quality of life declined, while anxiety and depression increased as both visual field and visual acuity declined.[121]

Bietti's crystalline dystrophy (BCD) is a rare, degenerative eye disease caused by mutations in the gene that encodes the orphan enzyme CYP4V2. There is no treatment or cure, and patients will gradually become blind. The pathophysiology of this disease is poorly understood. The physiological function of CYP4V2 is also poorly understood in healthy individuals, much less what is occurring abnormally in patients with this disease. The work described in this dissertation was conducted to better understand the molecular mechanisms behind this debilitating disease, and to identify potential therapeutic targets that may lead to treatment options.

To build a scientific foundation for elucidating the pathophysiology and biochemistry surrounding this disease, I have developed and characterized a murine model that recapitulates the primary phenotype observed in BCD. This knockout mouse model provides an *in vivo* platform for studying disease pathogenesis, biochemical characteristics, and evaluating therapeutic agents. Ocular tissue is not readily available from patients, as it is impractical to collect samples and would carry a very high risk of injury to the patient in doing so. Therefore, a preclinical animal model is essential to study the pathophysiology of disease, and to understand the underlying characteristics that drive the unique phenotype observed in BCD. An *in vivo* model also presents a practical means for testing therapeutic approaches, such as small molecules or gene replacement therapy that could be administered, while observing changes in the longitudinal progression of disease.

I also elucidated biochemical mechanisms associated with physiological function of CYP4V2 in an attempt to better understand the implications of mutations observed in BCD, but also of polymorphisms that may influence other conditions such as risk of deep vein thrombosis. It has been shown that BCD patients exhibit some systemic dyslipidemia due to non-functioning

CYP4V2 enzyme, but the only known site of clinically significant manifestation is in the eye. CYP4V2 is ubiquitously expressed, including in highly metabolic organs such as the liver, but little is known about its role in normal physiology. Therefore, it is important to understand the biochemistry and function in a healthy physiological system to identify the mechanism and specific contribution to lipid homeostasis. That will then enable better understanding of the abnormal processes that lead to disease.

The clinical implications for more thorough understanding of Bietti's crystalline dystrophy are substantial for patients with this disease. Furthermore, more thorough understanding of the biochemistry and physiological function of CYP4V2 extend beyond this blinding disease have much broader health implications for individuals with polymorphisms that may influence risk for other disorders. The research described in this dissertation is guided by the hypotheses and specific aims listed below.

1.6 Hypotheses and Specific Aims

Hypothesis 1: Targeted disruption of the murine ortholog of the *CYP4V2* gene (*Cyp4v3*) will recapitulate the biochemical and pathological defect(s) of Bietti's crystalline dystrophy.

Aim 1.1: Generation of a *Cyp4v3* knockout mouse line (Chapter 2).

Aim 1.2: Biochemical and pathological characterization of *Cyp4v3* knockout mice (Chapter 2).

Hypothesis 2: Loss of function of CYP4V2 enzyme activity in retinal pigmented epithelium is the primary causative factor in the pathological manifestation of Bietti's crystalline dystrophy.

Aim 2.1: Identify and model the *CYP4V2* mutation in BCD patient #7 (Chapter 3).

Hypothesis 3: Expression levels of CYP4V2 are influenced in part by post-transcriptional regulation by microRNAs.

Aim 3.1: Identify correlations of interindividual expression levels of CYP4V2 mRNA and/or protein with specific microRNA molecules (Chapter 4).

Aim 3.2: Determine functional specificity of candidate microRNA(s) for regulating CYP4V2 expression via interaction(s) with the 3' untranslated region of *CYP4V2* mRNA (Chapter 4).

Chapter 2

Generation and Characterization of a Murine Model of Bietti's Crystalline Dystrophy

The work presented in this chapter was published:

Investigative Ophthalmology & Visual Science. 2014;55:5572-5581

DOI: 10.1167/iovs.13-13717

Generation and Characterization of a Murine Model of Bietti Crystalline Dystrophy

Catherine M. Lockhart,[1] Mariko Nakano,[2] Allan E. Rettie,[2] and Edward J. Kelly[1]

[1]Department of Pharmaceutics, University of Washington, Seattle, Washington, United States
[2]Department of Medicinal Chemistry, University of Washington, Seattle, Washington, United States

Correspondence: Edward J. Kelly, Department of Pharmaceutics, 1959 NE Pacific Street, Health Sciences Building, Room H-272D, University of Washington, Box 357610, Seattle, WA 98195-7610, USA; edkelly@uw.edu.

Submitted: December 5, 2013 Accepted: July 30, 2014

Citation: Lockhart CM, Nakano M, Rettie AE, Kelly EJ. Generation and characterization of a murine model of Bietti crystalline dystrophy. Invest Ophthalmol Vis Sci. 2014;55:5572– 5581. DOI:10.1167/iovs.13-13717.

2.1 Abstract

PURPOSE. Bietti crystalline dystrophy (BCD) is a rare, autosomal recessive, progressive, degenerative eye disease caused by mutations in the CYP4V2 gene, for which no treatments are currently available. Cyp4v3 is the murine ortholog to CYP4V2, and to better understand the molecular pathogenesis of this disease we have established a Cyp4v3-null mouse line.

METHODS. Cyp4v3$^{-/-}$ mice were generated by homologous recombination in embryonic stem cells. Ocular morphologic characteristics were evaluated via fundus imaging, plasma lipid profiling, and histologic analysis via Oil Red O reactivity, hematoxylin and eosin staining, and transmission electron microscopy.

RESULTS. The Cyp4v3$^{-/-}$ mouse recapitulates the characteristic features of corneoretinal crystal

accumulation and systemic dyslipidemia seen in BCD. The Cyp4v3$^{-/-}$ mice behave normally and are viable and fertile when maintained under specific pathogen-free (SPF) housing conditions.

CONCLUSIONS. Cyp4v3$^{-/-}$ mice represent a promising preclinical model that may be used to better understand the disease etiology and to evaluate pharmacotherapies for this devastating condition.

Keywords: Bietti crystalline dystrophy, preclinical model, CYP4V2

2.2 Introduction

Bietti's crystalline dystrophy (BCD) is a rare, degenerative eye disease that was first identified in 1937 by Gian Battista Bietti, an Italian ophthalmologist who treated three patients with progressive night blindness. These patients developed sparkling crystalline deposits in their corneas and posterior pole of their retinas, leading to declining vision that did not respond to traditional vision correction.[73,75,124] Bietti crystalline dystrophy is regarded as a rare disease with a prevalence estimated at 1:67,000, although it may be underdiagnosed.[76,77] There is no available treatment, and patients will eventually become completely blind.

The symptoms and clinical features of BCD are similar to those of many forms of retinitis pigmentosa, characterized by gradual constriction of the visual field, night blindness, abnormal retinal electrophysiology, altered visual acuity, and often color blindness.[17] Structural findings are also typically similar to those for retinitis pigmentosa, including degeneration of the retinal pigment epithelium (RPE), pigment clumping, and sclerosis of the choroid.[17] Importantly, the hallmark characteristic that differentiates BCD from other retinal disorders is formation of yellow-white crystalline deposits on the cornea and retina.

There is a wide variability in phenotype among BCD patients with differing disease severity and rate of progression. Visual acuity is often diminished, but there are reports of

patients with best corrected vision within a normal range despite symptoms such as nyctalopia or blurred vision, the presence of characteristic crystalline deposits, and signs of retinal degeneration.[80,81] Optical coherence tomography (OCT) images of BCD patients have revealed not only the presence of crystals in retinal and corneal tissue,[19] but also the disruption and disorganization of cellular layers of the retina.[80,82] Electroretinography (ERG) examination typically shows decreased amplitudes of b-waves from both rods and cones;[82] however, in one study that evaluated 15 BCD patients, more than 50% of patients had recordable standard ERG, and 2 had readings within normal limits 20 years after initial BCD diagnosis, suggesting that ERG may not always correlate with disease progression.[83] In one case report, standard ERG was normal, but multifocal ERG showed depressed central responses consistent with the macular lesion identified by OCT.[84] This suggests that the neuroretinal cells were still functioning in this patient despite RPE degeneration. Reports indicate that neuroretinal cell dysfunction in BCD patients is highly variable, and it is reasonable to suggest that the progression of RPE degeneration in BCD may originate from tissues on the basal side of the RPE rather than the neural cell layers.

In 2004, researchers at the National Eye Institute identified a mutation in the ‘‘orphan’’ cytochrome P450 4V2 (CYP4V2) gene in patients with BCD.[17] CYP4V2 is one of 57 functional human enzymes in the cytochrome P450 superfamily of heme-containing monooxygenase enzymes. While the enzyme is ubiquitously distributed, expression in the eye is highest within RPE cells, with weaker expression in the cornea.[9,90] CYP4V2 is one of 13 human P450 enzymes classified as orphans because their substrate specificity and physiological role are not well characterized.[90] To date, over 50 mutations have been identified in BCD patients, with at least one mutation in each of the gene’s 11 exons.[17,19,27,28,39,40,82-84,98-101,103,104,109-111,113-115,117-119]

Genotype analysis has shown that the most common pathologic CYP4V2 mutation is c.802-8_810del17insGC, which results in deletion of exon 7 in the mature transcript, though other mutations in each exon are also linked to the disease.[79,113,115] Additionally, a relatively common polymorphism in CYP4V2 (rs13146272; Q259K), with a minor allele frequency of 45%, has been associated with deep vein thrombosis.[125] The inheritance pattern of BCD is generally considered to be autosomal recessive, though some reports suggest possible haploinsufficiency, in which a heterozygous carrier may display some phenotypic characteristics, though less severe.[82]

Clinical systemic dyslipidemia in BCD patients has been reported, possibly due to nonfunctional CYP4V2 enzymes. For example, lymphocytes from BCD patients displayed a lack of two fatty acid-binding proteins, involved with fatty acid trafficking, with molecular weights of 32 and 45 kDa, that are expressed in control subjects.[88] Further analysis showed that the 32-kDa protein preferentially bound docosahexaenoic acid (DHA, C22:6), a-linolenic acid (ALA, C18:3), and palmitic acid (C16:0).[88] Abnormal fatty acid processing and storage has been identified in lymphocytes and fibroblasts of BCD patients, including decreased conversion of fatty acid precursors into n- 3 polyunsaturated fatty acids (PUFAs) and increased incorporation of ALA into triglycerides.[13] Further, fatty acid profiling in BCD serum showed an abnormal composition of fatty acids and reduced activity of the D-9-desaturase regardless of the CYP4V2 mutation spectrum.[11,75] Lymphocytes and fibroblasts from three BCD patients revealed crystalline deposits, some resembling complex lipid deposits, although the crystal composition was not determined.[75] Similarly, the composition of ocular crystals that accrue in BCD has not been determined. Elucidation of the chemical nature of these crystals would be an invaluable step toward a biochemical understanding of BCD; however, the availability of this material from

human subjects is extremely limited. Analysis is further complicated by adventitious debris from macular degeneration often present in aging patients, along with the observation that crystals are no longer present in end-stage disease.[126,127] To understand the biochemical mechanism underlying this progressive blinding disease, we have previously cloned and expressed the human enzyme, demonstrating that, like other CYP4 enzymes, CYP4V2 characteristically catalyzes medium- and long-chain fatty acid ω-hydroxylation reactions despite sharing only 31% to 37% sequence homology to other CYP4 enzymes.[89] In addition, the enzyme has x-hydroxylase activity for the docosanoids eicosapentaenoic acid (EPA, C20:5(n-3)) and DHA, with kinetic parameters comparable to those of CYP4F2.[9]

The Cyp4v3 gene is the mouse ortholog of human CYP4V2, and the proteins share 82% identity and 92% similarity.[91] Therefore, to better understand BCD etiology, we have generated a strain of $Cyp4v3^{-/-}$ mice that are viable and fertile with no overt phenotype at birth. To determine whether mice lacking functional CYP4V3 recapitulate the pathophysiology of BCD, $Cyp4v3^{-/-}$ mouse eyes were screened for the presence of ocular crystalline deposits by fundus examination. In addition, ocular lipid deposition was examined histochemically by Oil Red O staining; retinal structural features were assessed by both light microscopy of hematoxylin and eosin (H&E)-stained sections and transmission electron microscopy (TEM); and plasma PUFA profiles were compared to those of wild-type animals.

2.3 Materials and Methods

Atropine (1% ophthalmic solution), ketamine (100 mg/mL), xylazine (20 mg/mL), and GenTeal lubricant eye gel were purchased from the University of Washington Drug Services (Seattle, WA, USA). 2,2-d_2-Stearic acid was purchased from Sigma-Aldrich Corp. (St. Louis,

MO, USA). All chemicals were of the highest purity available.

2.3.1 Production and Characterization of Cyp4v3$^{-/-}$ Mice

Embryonic stem cells (clone ID KO-1055, Cyp4v3_BB5) with targeted disruption of the Cyp4v3 gene were obtained from the Knockout Mouse Project (https://www.komp.org/, University of California, Davis [in the public domain]). The targeting vector design from Velocigene (Regeneron Pharmaceuticals, Inc., Tarrytown, NY, USA) contains the 5' untranslated region and start codon of exon 1 of Cyp4v3 in the 5' arm, and the 3' arm starts after the stop codon of exon 11. Thus, homologous recombination of the targeting vector results in a complete absence of any CYP4V3 coding sequence (Figure 2-1). With assistance from the University of Washington Transgenic Core Facility, the embryonic stem (ES) cell clone was expanded on embryonic feeder cells, evaluated for correct gene targeting by polymerase chain reaction (PCR), and then injected into albino C57Bl/6 blastocysts to generate chimeric mice. Mice with high degrees of chimerism were backcrossed with albino C57Bl/6 mice to test for germline transmission. Offspring that inherited the targeted Cyp4v3 allele were interbred as heterozygotes for production of Cyp4v3$^{-/-}$ mice. The Cyp4v3$^{-/-}$ mice behave normally and are viable and fertile when maintained under specific pathogen-free (SPF) housing conditions to exclude the possibility of infectious agents known to cause murine diseases that may confound phenotypes attributable to the gene targeting event.

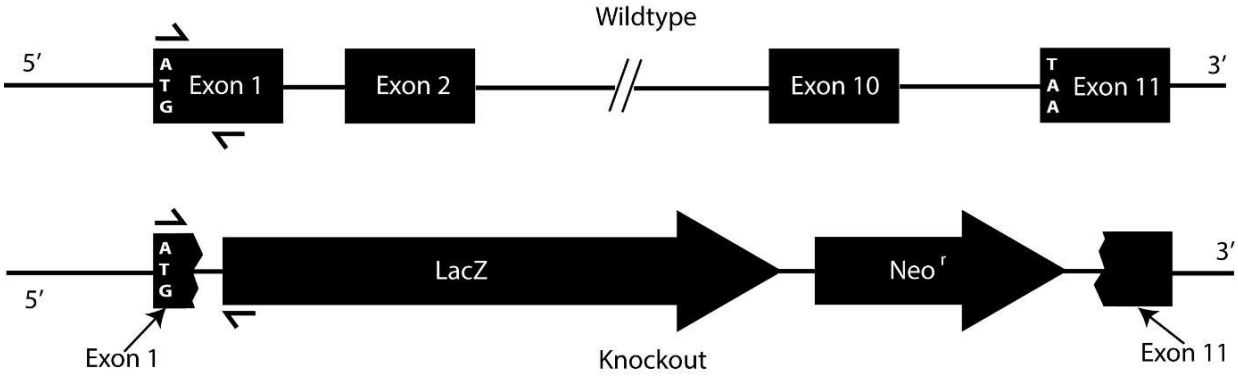

Figure 2-1. **Cyp4v3 knockout vector design.** Mouse Cyp4v3 gene structure and targeting vector design. Top: The mouse Cyp4v3 gene is composed of 11 coding exons and maps to chromosomal region 8 B1.1 (syntenic with human CYP4V2, chromosome 4q35.2). Bottom: Arrangement of the Cyp4v3 locus following homologous recombination with the targeting vector. The replacement vector (http://www.velocigene.com/komp/detail/10578 [in the public domain]) deletes exons 2 to 10 and portions of exons 1 and 11 of the Cyp4v3 gene (deletion size 26,040 bp) and inserts a splice acceptor-lacZ reporter and ubC-Neo^{r} resistance cassette (ZEN-Ub1). The locations of the primers used for PCR genotyping are indicated by directional arrows over exon 1 and the lacZ reporter gene.

To confirm the null allele in Cyp4v3$^{-/-}$ mice, genotype analysis was performed by PCR. Primers for Cyp4v3, LacZ, and fatty acid binding protein (FABP) were mixed with DNA extracted from Cyp4v3$^{-/-}$ mice, heterozygote mice, and wild- type controls in a master mix containing GemTaq 53 Reaction Buffer and GemTaq polymerase (MGQuest; Lynnwood, WA, USA), deoxyribonucleotide triphosphates (dNTPs; Qiagen, Valencia, CA, USA), 5 M betaine (Sigma-Aldrich Corp.), and dimethyl sulfoxide (DMSO; Sigma-Aldrich Corp.). Polymerase chain reaction amplicons were separated by agarose gel electrophoresis and stained with ethidium bromide (Bio-Rad, Hercules, CA, USA); data were acquired on a UVP Doc-ItLS image acquisition system (Upland, CA, USA).

To detect the nontargeted wild-type allele, primers Cyp4v3- Ex1.for and Cyp4v3-Ex1.rev were used. The forward primer spans nucleotides (nt) 19 to 37 of the Cyp4v3 mRNA (NM_133969.2) and the reverse primer nt 241 to 265, resulting in a 246-bp amplicon. The lacZ.rev primer is located at nt 111 to 132 of the ZEN-Ub1 lacZ-NeoR selection cassette

designed by Velocigene for Knockout Mouse Project (KOMP) and, in combination with primer Cyp4v3-Ex1.for, yields a 335-bp amplicon for a correctly targeted allele. The location of the Cyp4v3-Ex1.rev primer is beyond the portion of the Cyp4v3 gene that is deleted in the replacement vector. Thus, as seen in Figure 2-1, it yields a product only for wild-type or heterozygous mice. To control for the presence of PCR-amplifiable genomic DNA, each sample was subjected to analysis using primers for the single-copy somatic gene (FABP) as previously described.[128]

To confirm that the Cyp4v3 gene targeting event is truly null, CYP4V3 protein expression was assessed by Western blot analysis. Microsomes were prepared from excised livers from Cyp4v3$^{-/-}$ mice (n = 3) and wild-type control mice (n = 3) as previously described.[129] Sodium dodecyl sulfate–polyacrylamide gel electrophoresis (SDS-PAGE) was used to separate proteins in samples containing 15 μg total protein per well. Separated proteins were transferred to nitrocellulose membranes (Invitrogen, Carlsbad, CA, USA) using iBlot (Invitrogen), blocked overnight in Odyssey blocking buffer (Li-Cor, Lincoln, NE, USA), and probed for CYP4V3 using a rabbit polyclonal antibody raised against human CYP4V2;[9] b-actin (Li-Cor) was used as a loading control. Immunoreactivity was detected using Li-Cor secondary antibodies, and images were generated with Odyssey CLX (Li-Cor).

2.3.2 Fundus Imaging

To screen for changes in ocular appearance, a Micron II small animal retinal imaging system from Phoenix Research Laboratories (Pleasanton, CA, USA) was used. In brief, mouse eyes were first treated with topical atropine (Bausch & Lomb, Tampa, FL, USA) and then the mice were anesthetized with ketamine/xylazine (University of Washington Drug Services) prior to fundus imaging. GenTeal lubricant eye gel (Novartis, East Hanover, NJ, USA) was applied to

the eyes of anesthetized mice to keep them moist during imaging. Mice were placed on the stage of the imaging system and placed under the camera to capture retinal images. Animal studies were conducted in accordance with all applicable animal care and use laws, regulations, and guidelines, including adherence to the ARVO Statement for the Use of Animals in Ophthalmic and Vision Research guidelines, under a protocol approved by the University of Washington Institutional Animal Care and Use Committee in an Association for Assessment and Accreditation of Laboratory Animal Care–accredited facility.

2.3.3 Plasma PUFA Profiling

Analysis of 20 μL sera from Cyp4v3 knockout and wild-type mice for PUFA content was performed using methanol and methyl-t-butyl ether (MTBE) as described previously.[130] Specifically, 1 μg 2,2-d_2-stearic acid (internal standard) was added to the biological sample, followed by 0.75 mL methanol (Thermo Fisher Science, Pittsburgh, PA, USA). After shaking for 5 minutes, 1.5 mL MTBE was added to the mixture and shaken for 1 hour at room temperature. Then, 0.63 mL nanopure water was added, and the mixture was centrifuged at 1000g for 10 minutes. The upper organic layer was transferred to a clean centrifuge tube, and the extraction procedure was repeated a second time. The pooled organic layers were washed with small quantities of 0.2 M aqueous potassium chloride and nanopure water. Next, the organic solvent was dried under a stream of N_2 gas. The extracted fraction was reconstituted with a small amount of ethyl acetate and derivatized using a molar excess of diazomethane. After derivatization, the sample was dried under a stream of N_2 gas. The extracted fraction was reconstituted with 60 μL ethyl acetate and analyzed by gas chromatography and electron ionization mass spectrometry (GC-EI/MS). At this point, all free fatty acids had been derivatized to their methyl ester forms.

The following procedure released fatty acids from complex lipids and transesterified them. The derivatized samples in ethyl acetate were transferred to a glass tube and mixed with 200 μL toluene and 1 mL 2% sulfuric acid in methanol (vol/vol). After the tube was sealed and vortexed quickly, the lipids were heated at 100°C in a sand bath for 65 minutes. Then the lipids were cooled on ice, and 1.2 mL nanopure water was added. Lipids were extracted with 0.7 mL hexane, and the extraction was repeated two more times. The combined solvent was dried under a stream of N_2 gas, and the dried fraction was reconstituted in 60 μL ethyl acetate. Finally, total fatty acids were analyzed by GC-EI/MS.

2.3.4 Lipid Profiling by GC-EI/MS

The transesterified lipids were analyzed on a Shimadzu QP2010 GCMS (Shimadzu, Kyoto, Japan) fitted with a 60-m fused-silica capillary column (DB-1) using selected ion monitoring. The analytes were injected at a temperature of 100°C. After 2 minutes, the oven temperature was raised at 30°C/min to 1308C, 10°C/min to 180°C, held for 2 minutes, 48C/min to 210°C, 10°C/min to 235°C, held for 3 minutes, 4°C/min to 255°C, 10°C/min to 310°C, then held for 4 minutes. Under these conditions, the derivatized saturated and unsaturated fatty acids eluted as follows: d_2-C18:0 at 21.30 minutes, C14:0 at 13.86 minutes, C16:0 at 17.77 minutes, C16:1 at 17.36 minutes, C18:0 at 21.30 minutes, C18:1 cis-9 at 20.91 minutes, C18:1 cis-11 at 21.01 minutes, C18:2 at 20.76 minutes, C18:3 at 20.83 minutes, C20:4 at 23.66 minutes, C20:5 at 23.57 minutes, and C22:6 at 27.65 minutes. Quantitation was achieved by selected ion monitoring of the characteristic $[M- 31]^+$ and $[M-43]^+$ fragment ions found in EI spectra of the majority of fatty acid methyl esters. The PUFAs' most abundant ions appeared at less than 100 mass-to-charge ratio (m/z), unlike other saturated and mono- and diunsaturated fatty acids. Thus 74 m/z is utilized as a characteristic ion for penta- and hexaunsaturated fatty acids as described

previously.[9,89] Standard curves ($r^2 > 0.98$) for each fatty acid were generated with their authentic chemical standards. Differences between two means within a group were tested with Student's t-test (two-tail, two-sample unequal variance by Student's t-test using GraphPad Prism [GraphPad Software, Inc., La Jolla, CA, USA]).

2.3.5 Histologic Analysis

Whole eyes dissected from mice were immediately submerged in 10% formalin (Fisher Scientific, Hampton, NH, USA) and stored at 4°C to fix the tissue for standard histology processing by the University of Washington Histology and Pathology Specialized Services Core as described previously.[131] Briefly, formalin-fixed tissues were dehydrated in graded ethanols and embedded in paraffin. Sections (10 μm) were deparaffinized, rehydrated, and treated with sodium citrate buffer before staining with H&E. Slides were washed thoroughly and fixed, and images were captured on a Nikon Ti-S microscope (Nikon Instruments, Inc., Melville, NY, USA).

For histochemical lipid analysis, whole eyes were harvested from mice, immediately frozen at -80°C in Tissue-Tek optimum temperature cutting compound (Electron Microscopy Sciences, Fort Washington, PA, USA), and submitted for histologic processing and Oil Red O staining for lipid by the University of Washington Histology and Pathology Specialized Services Core. Briefly, frozen sections were sliced 8 to 10 μm thick and mounted on slides. The slides were dehydrated in propylene glycol and then stained in Oil Red O solution for 8 to 10 minutes at 60°C. Slides were then placed in 85% propylene glycol solution for 2 to 5 minutes for differentiation, rinsed, and counterstained in hematoxylin solution for 30 seconds. Slides were washed thoroughly and fixed, and images were captured on a Nikon Ti-S microscope (Nikon Instruments, Inc., Melville, NY, USA).

For analysis of retinas by TEM, whole eyes harvested from mice were cut open to facilitate fixative penetration and then submerged in 1/2x Karnovsky's fixative (2.5% glutaraldehyde with 2% formaldehyde in 0.1 M buffer). The tissue was postfixed in osmium tetroxide and processed, sectioned, and examined by TEM according to standard protocols as described previously.[131]

2.4 Results

To confirm successful knockout of Cyp4v3 alleles and to verify the absence of CYP4V3 protein in Cyp4v3$^{-/-}$ mice, we performed PCR genotyping analysis and Western blot analysis. The Cyp4v3 amplicon of 246 bp in length is present in both wild-type and heterozygous mice, but absent in mice with the null allele. The LacZ gene is a marker in the knockout construct and appears as a band at 335 bp in knockout and heterozygote mice. Fatty acid binding protein is a control to verify genomic DNA integrity and should be present in all samples tested. Figure 2-2a shows the results of PCR genotyping for Cyp4v3$^{-/-}$, Cyp4v3$^{+/-}$, and wild-type control mice. Lanes 1, 6, and 11 contain molecular weight markers in 100-bp increments; lanes 2, 7, and 12 contain DNA samples from wild-type control mice; lanes 3, 8, and 13 contain DNA from heterozygote mice; lanes 4, 9, and 14 contain DNA from Cyp4v3$^{-/-}$ mice; and lanes 5, 10, and 15 contain a nontemplate control. As expected, the wild-type control has bands positive for Cyp4v3 and FABP, but is negative for LacZ that was part of the knockout construct. The heterozygote has bands for all three markers, while the Cyp4v3$^{-/-}$ mouse is negative for Cyp4v3 but positive for LacZ and FABP. This confirms correct gene targeting in Cyp4v3$^{-/-}$ mice.

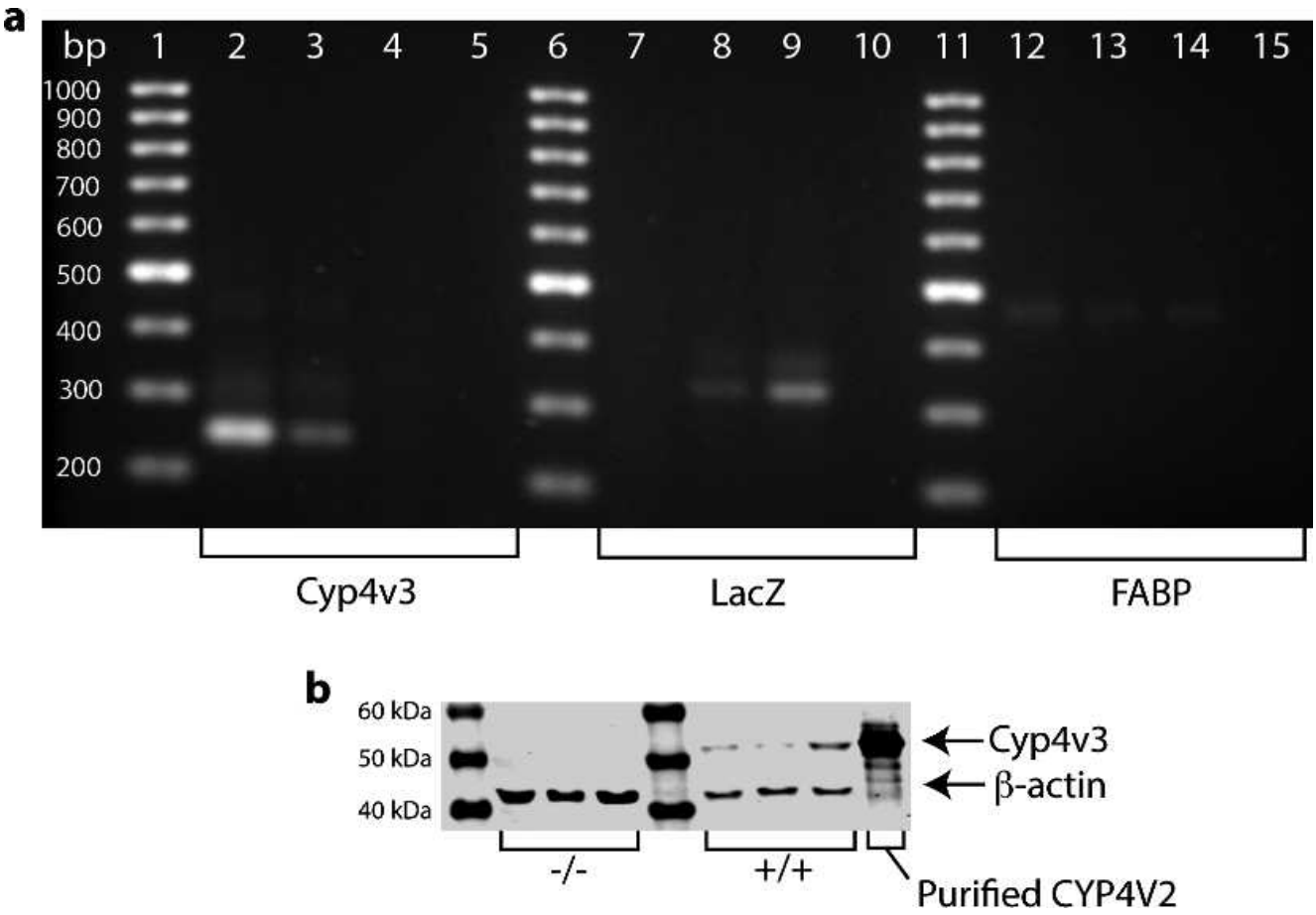

Figure 2-2. Mouse Cyp4v3 genotype and expression. Confirmation of genotype and protein expression of Cyp4v3$^{-/-}$ mice compared to wild-type controls. (a) PCR of wild-type (lanes 2, 7, and 12), heterozygote (lanes 3, 8, and 13), and Cyp4v3$^{-/-}$ mice (lanes 4, 9, and 14) shows that wild-type mice have positive bands for Cyp4v3 (lane 2), negative bands for the LacZ reporter construct (lane 7), and positive bands for FABP to verify the presence of genomic DNA (lane 12). Heterozygotes show bands for all three genes, and Cyp4v3$^{-/-}$ mice are negative for Cyp4v3 (lane 4), positive for the LacZ reporter construct (lane 9), and positive for FABP (lane 14). This confirms that Cyp4v3$^{-/-}$ mice lack functional Cyp4v3, and the targeting vector was successfully incorporated into the genome. (b) Western blot analysis of Cyp4v3$^{-/-}$ mice (lanes 2, 3, and 4), wild-type mice (lanes 5, 6, and 7), and 0.18 pmol human purified CYP4V2 as a validation control. Lower bands are b-actin, used to verify the presence of equivalent total protein in each lane, and upper bands show the presence (wild-type) and absence (Cyp4v3$^{-/-}$) of CYP4V3 protein expression, as expected. This confirms that mice without functional Cyp4v3 do not produce the corresponding protein.

Western blotting was performed to verify that Cyp4v3$^{-/-}$ mice lack CYP4V3 protein. Microsomes were prepared from mouse livers according to previously published protocols and

proteins separated by SDS-PAGE electrophoresis.[45] CYP4V3 has a molecular weight of approximately 60 kDa and appears as the upper band in Figure 2-2b. The lower band at approximately 42 kDa is β-actin and confirms that equivalent amounts of protein were loaded in each lane of the gel. Lane 1 is the molecular weight marker; lanes 2, 3, and 4 contain liver microsomes (15 μg total protein) from Cyp4v3$^{-/-}$ mice; lanes 5, 6, and 7 contain liver microsomes (15 μg total protein) from wild-type control mice; and lane 8 contains 0.18 pmol purified human CYP4V2.

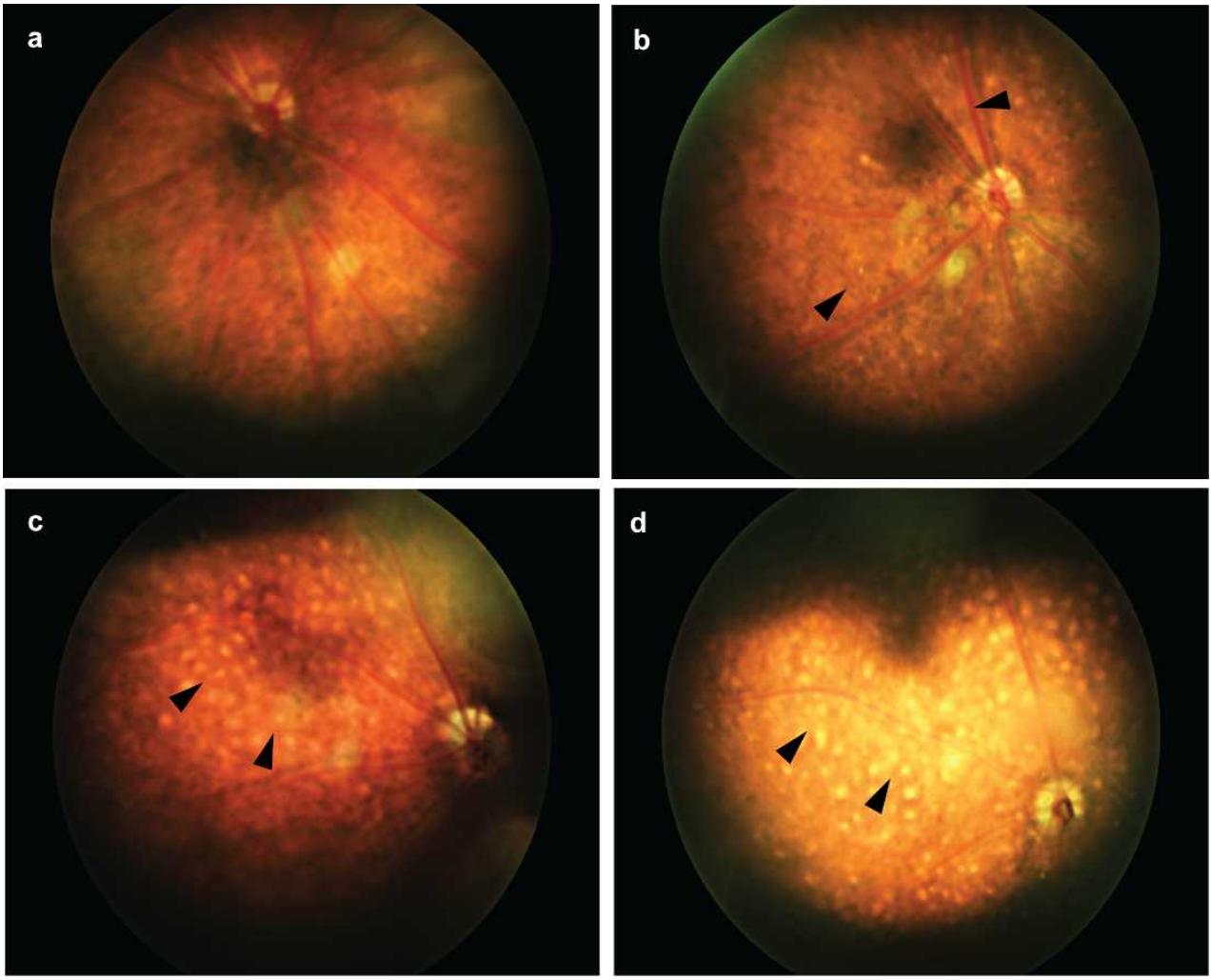

Figure 2-3. Mouse fundus images. Fundus images of Cyp4v3$^{-/-}$ mice and a Cyp4v3$^{+/+}$ control. (a) Normal retina of a 12-month-old Cyp4v3$^{+/+}$ mouse; (b) retina of a 6- month-old Cyp4v3$^{-/-}$ mouse with sparse, reflective crystalline deposits (arrowheads); (c) retina of 12-month-old and (d) 18-month-old Cyp4v3$^{-/-}$ mice with highly confluent crystalline deposits (arrowheads).

As crystalline deposits are a hallmark of BCD, we performed fundus imaging on Cyp4v3$^{-/-}$ mice (Figure 2-3). At 6 months of age (n = 4 each wild-type and Cyp4v3$^{-/-}$), sparse crystals (10–20 μm in diameter) were visible on retinal exam, and by 12 months of age (n = 6 wild-type and n = 8 Cyp4v3$^{-/-}$) the crystalline pattern became stark and approached confluence. Microscope measurements indicated that each deposit was approximately 10 to 20 μm in diameter, on average. These are similar in absolute size to those observed in BCD patients,[4] and appear larger in mice due to the much smaller relative globe size. From a species comparison, a 6-month-old mouse approximates humans in their 20s, corresponding to the approximate age of BCD diagnosis. A 12-month-old mouse approximates humans in their 50s, corresponding to the approximate age of legal blindness in BCD.[75,132] Thus, the gross ocular pathology of Cyp4v3$^{-/-}$ mice recapitulates the clinical timeline of BCD pathogenesis, and crystal morphometry mimics the human disease.[81]

To gain more detailed knowledge of the ocular pathology of Cyp4v3$^{-/-}$ mice, we evaluated histologic sections from wild- type and Cyp4v3$^{-/-}$ mice (Figure 2-4). All mice were older than 18 months and of similar age. In Figure 2-4, the top row (Figure 2-4a, Figure 2-4b) shows histologic sections of two individual wild-type mice. The bottom row (Figure 2-4c, Figure 2-4d) shows histologic sections of two individual Cyp4v3$^{-/-}$ mice. The sections clearly delineate the layers of the retina, and there is no visible difference in the neural retinal tissue between wild-type and Cyp4v3$^{-/-}$ mice. Of particular interest, however, is a distinct linear array of optically clear vacuoles (arrowheads, Figure 2-4c, Figure 2-4d) contained deep within the photoreceptor outer segment and adjacent to the pigment epithelium. Contents of the vacuoles were lost during tissue processing; however, their size and location are consistent with our knowledge of the crystalline deposits observed in BCD patients and in our Cyp4v3$^{-/-}$ mice as shown in Figure 2-3.

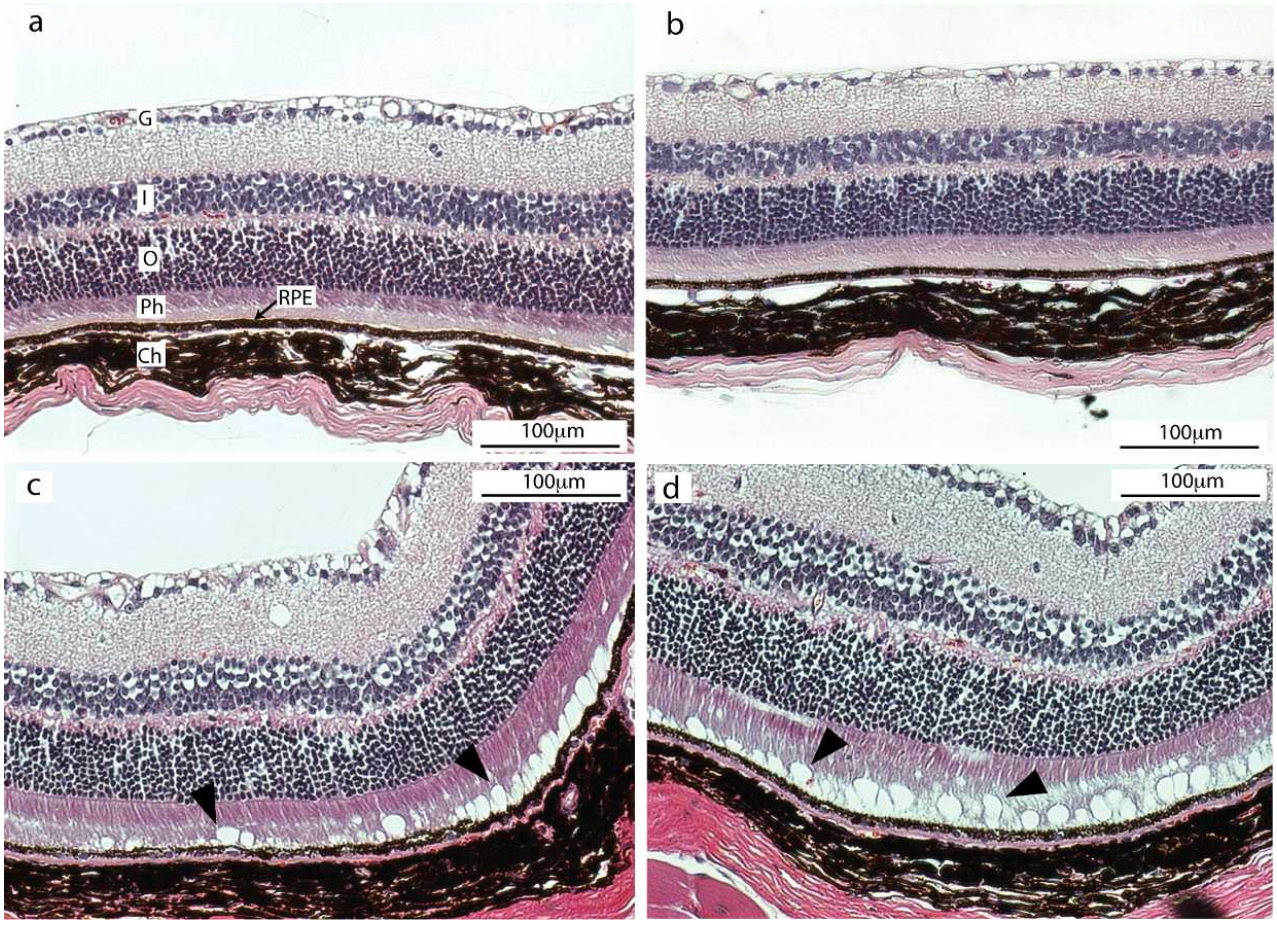

Figure 2-4. Histologic sections of murine retinas. 20x magnification. (a, b) Images from two individual wild-type mice and (c, d) from two individual Cyp4v3$^{-/-}$ mice. The tissue structures appear normal in all four mice. However, in the Cyp4v3$^{-/-}$ mouse (c, d), circular vacuoles are present at the base of the photoreceptor layer just anterior to the RPE cells (arrowheads). These vacuoles are consistent in size, location, and composition with the crystalline deposits observed by fundus imaging in BCD patients and Cyp4v3$^{-/-}$ mice. Ch, choroid; G, ganglion cell layer; I, inner nuclear layer; O, outer nuclear layer; Ph, photoreceptor cell layer; RPE, retinal pigmented epithelium.

Images gathered from TEM of retinal sections from wild- type and Cyp4v3$^{-/-}$ mice are shown in Figure 2-5. Again, all mice were older than 18 months and of similar age. Images in Figure 2-5a and Figure 2-5b are from two different wild-type mice, and Figure 2-5c and Figure 2-5d are from two separate Cyp4v3$^{-/-}$ mice. Osmification of tissues for examination by EM results in a marked increase in the electron density of lipid-containing structures. Consequently,

on electron microscopy (EM), the lipid-filled vacuoles represented as optically clear spaces in Figure 2-4 appear as either scattered solitary foci or confluent black globular structures arranged in various patterns in Figure 2-5 due to the number and close adjacency of vacuoles. In one sample from a Cyp4v3$^{-/-}$ albino mouse (Figure 2-5d), the pigment normally present within the pigment epithelium is missing, but the other structures are still present.

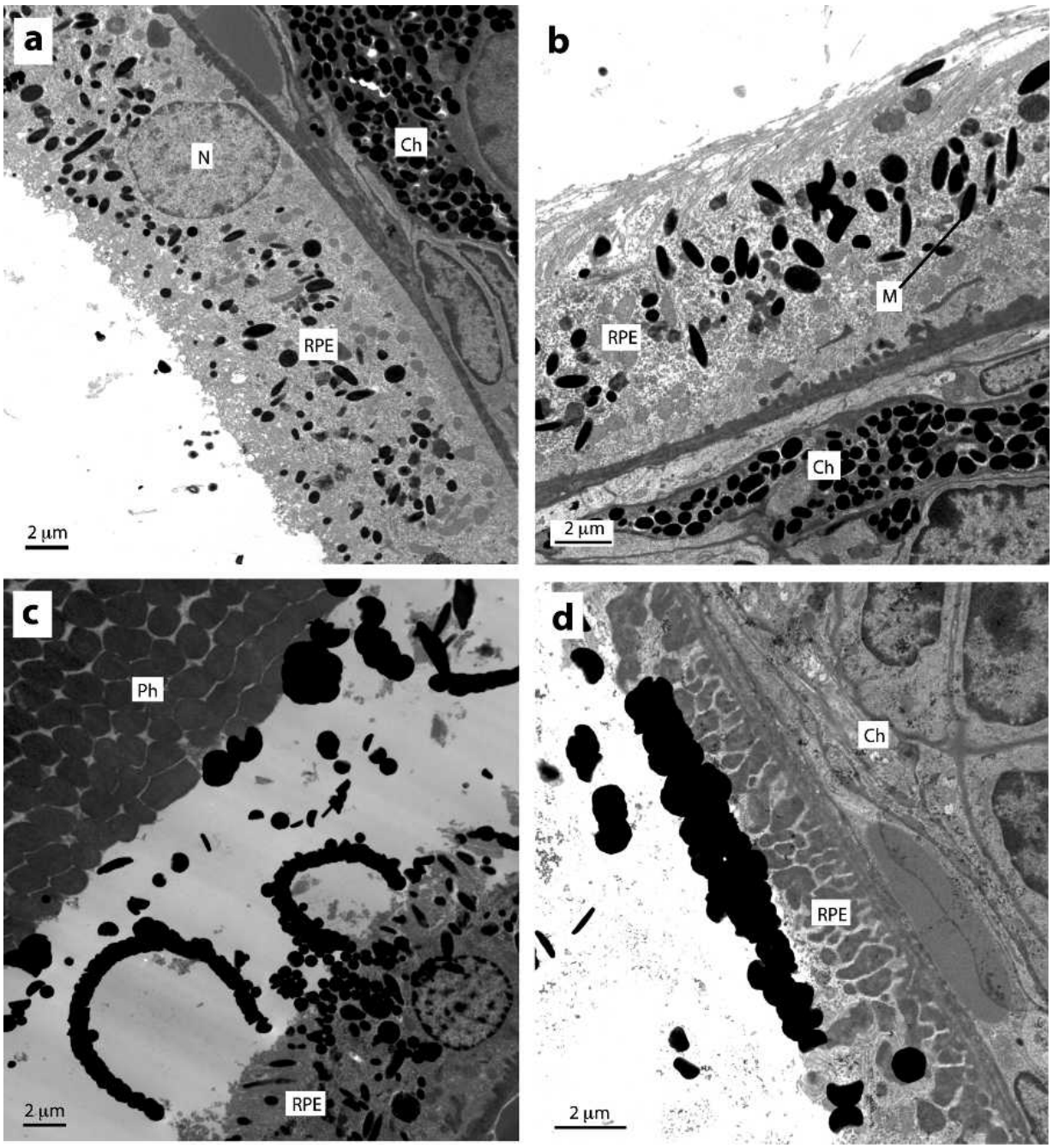

Figure 2-5. Transmission electron microscopy images of murine retinas. (a, b) Retinas of two different wild-type control mice. (c, d) Retinas of two Cyp4v3$^{-/-}$ mice. The presence of osmium increases the electron density of lipid-containing structures, so lipid-filled vacuoles appear as scattered solitary foci or confluent black globular structures. In one sample from a Cyp4v3$^{-/-}$ albino mouse, the pigment normally present within the pigment epithelium was missing, but other structures were the same. Ch, choroid; M, melanin pigment granule; N, nucleus; Ph, photoreceptors; RPE, retinal pigmented epithelium.

Biochemical analysis of murine plasma revealed changes in several fatty acids in knockout mice. At 12 months of age, C18:0 levels were significantly lower, while C18:2 and C18:3 levels were significantly higher in knockout mice versus wild- type controls. A previous study in BCD patients also showed a difference in C18:0 levels of similar magnitude, but in the opposite direction to our results in mice. Specifically, BCD patients exhibited a significantly higher level of C18:0 compared to healthy controls (P = 0.007). The n-3 PUFA DHA level was numerically higher in knockout versus wild- type mice, but just failed to reach statistical significance (P = 0.07; Figure 2-6). Levels of DHA showed a similar trend toward elevated levels in BCD patients that, as in Cyp4v3$^{-/-}$ mice, approached but did not reach statistical significance (P = 0.12).[11] These results suggest that systemic dyslipidemia is a common component in Cyp4v3$^{-/-}$ mice and BCD patients, but the mechanism and clinical relevance remain unclear.

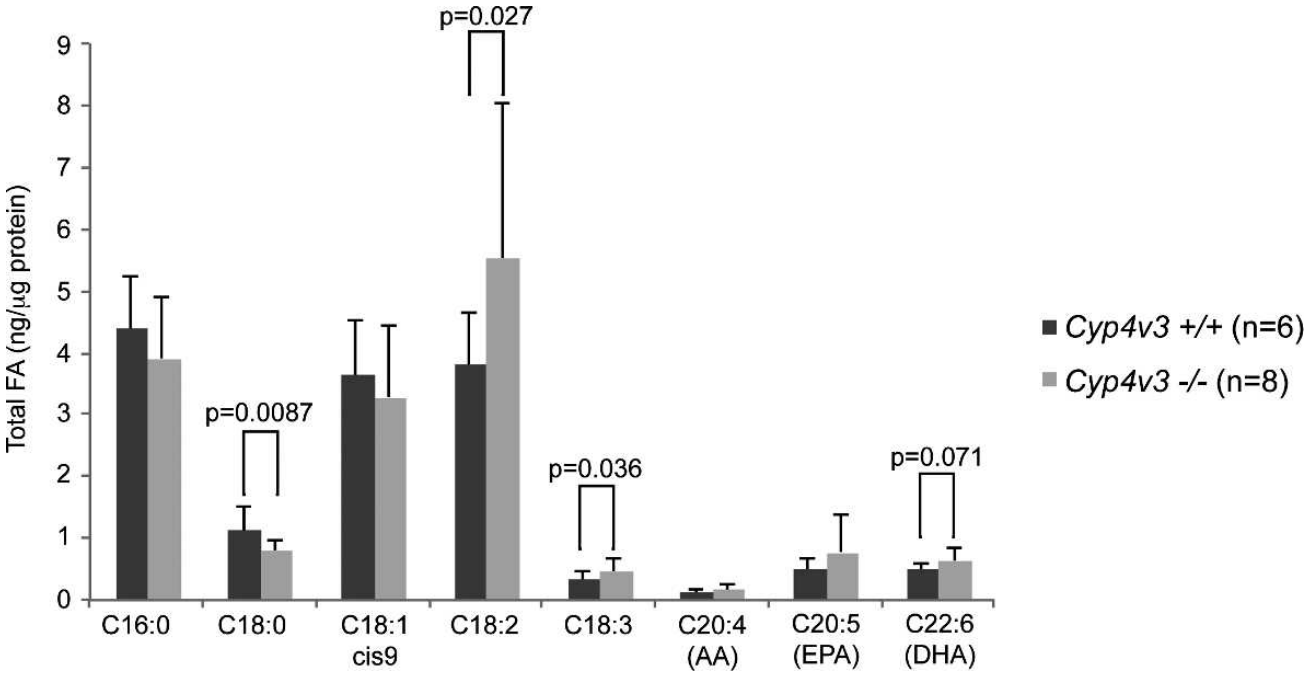

Figure 2-6. Murine lipid analysis**.** Serum fatty acid concentrations in Cyp4v3$^{-/-}$ mice compared with age-matched Cyp4v3$^{+/+}$ controls.

In addition to plasma lipid analysis, we examined the eyes of Cyp4v3$^{-/-}$ mice using the lysochrome diazo dye Oil Red O. While 6-month-old mice appeared normal (data not shown), 12-month-old mice exhibited significant focal accumulation of Oil Red O lipid droplets within the choroid layer (Figure 2-7). This suggests that lipid processing in ocular tissue is abnormal in Cyp4v3$^{-/-}$ mice and has an age-related progression. Indeed, ocular lipid processing becomes much less efficient with advanced age, and it has been observed that lipids accumulate in the Bruch's membrane over time even in normal, healthy eyes. This accumulation has been suggested to influence the pathological formation of lesions in age-related macular degeneration.[133,134]

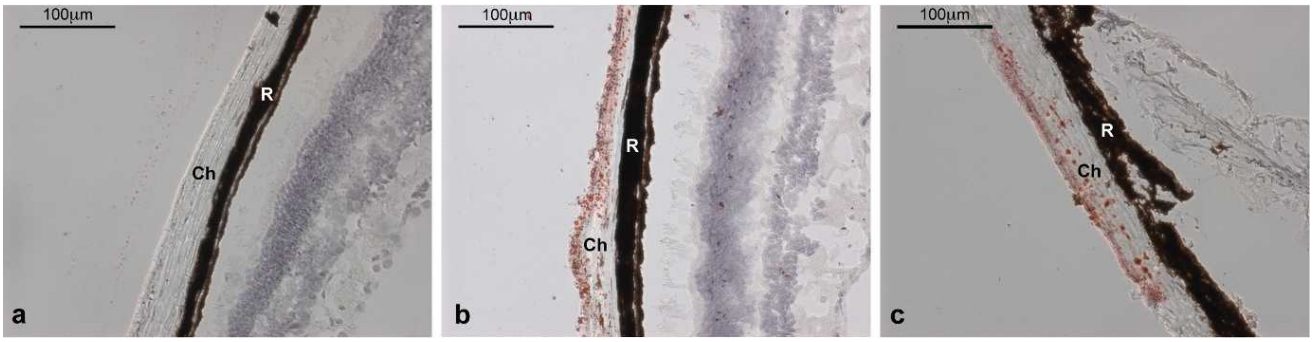

Figure 2-7. Lipid microscopy. Oil Red O staining of cross-sectional eye tissue samples from 12-month-old Cyp4v3$^{-/-}$ mice and an age-matched Cyp4v3$^{+/+}$ control. (a) Normal Cyp4v3$^{+/+}$; (b, c) two individual Cyp4v3$^{-/-}$ mice with red-stained lipid droplets visible throughout. Ch, choroid; R, retinal pigment epithelium.

2.5 Discussion

Here we describe generation and characterization of a Cyp4v3$^{-/-}$ mouse developed as a preclinical model for BCD. This model displays age-related progression of the disease that mimics the human pathology in ocular tissue, and also exhibits systemic dyslipidemia as reported in human patients. Human CYP4V2 and the murine ortholog CYP4V3 are likely involved in

lipid homeostasis in that the human enzyme is known to catalyze preferential ω-hydroxylase activity on medium-chain fatty acids.[89] Of particular interest is the role of CYP4V2 in metabolism of DHA both systemically and in ocular tissue, because DHA is an essential component of retinal rod outer segment membranes, and is also a known precursor to resolvins and protectins (essential components in innate anti- inflammatory modulation).[135-138] Pathology from nonfunctional CYP4V2 may be related to inflammation in ocular tissue. This would follow other age-related retinal degenerative diseases such as macular degeneration, in which inflammatory response has an important role.[139]

Recycling of rod outer segment membranes is a very active process, with as many as 10% of disc membranes shed each day in a normal eye.[140] Dysfunction in CYP4V2 may disrupt membrane processing in the RPE, leading to localized dyslipidemia and photoreceptor degradation. Given the slow, age-related progression of BCD, however, CYP4V2 may not be critical for recycling rod outer segments, as significant disruption of the high turnover would imply more rapidly progressing pathology.

Because the onset of BCD is unlike early-onset, aggressive ocular diseases (e.g., Leber's congenital amaurosis or primary congenital glaucoma), the hypothesis that CYP4V2 is critical to recycling of essential PUFA components of rod outer segments seems unlikely given the rapid turnover of these organelles. An attractive alternative hypothesis is that CYP4V2 plays a role in attenuating the signaling pathway mediated by resolvins/protectins, potent anti-inflammatory mediators.[139] We have previously demonstrated that CYP4V2 metabolizes DHA and EPA to their ω-hydroxy products. It is possible that ω-hydroxy docosanoids are not substrates for the lipoxygenase enzymes responsible for generating resolvins/protectins from DHA/EPA, thus limiting their production. Alternatively, the resolvin/protectin molecules themselves may be

substrates for CYP4V2. This would be an interesting counterbalance to another CYP4 enzyme (CYP4F3A), which is also involved in modulating inflammatory signaling pathways. In the case of CYP4F3A, this neutrophil-specific splice variant enzyme plays a key role in mitigating leukotriene B4 signaling by ω-hydroxylation, thus inactivating this arachidonic acid–derived n-6 proinflammatory lipid molecule.[95] Considering that resolvins/protectins are anti- inflammatory lipid signaling molecules, CYP4V2 could be playing a role in terminating the resolution phase of the inflammatory process. Importantly, evaluation of ARPE-19 cells revealed that CYP4V2 is the only known ω-hydroxylase enzyme expressed in RPE cells.[9] In such a scenario, it is plausible that acute loss of CYP4V2 is not detrimental, and that it is only with time and other confounding factors (e.g., environmental or dietary) that BCD progresses to a clinically diagnosed state. More work is required to test these admittedly speculative scenarios.

There are a number of limitations to this study. First, as this was a preliminary investigation into the phenotype of a newly established Cyp4v3$^{-/-}$ mouse line, the number of mice evaluated was limited, although the fundus pathology with crystalline deposits occurred consistently across all individuals examined. Second, although there is documented dyslipidemia in BCD patients, the clinical relevance has not yet been determined. While Oil Red O staining of the eye shows a clear difference in the knockout mouse, it does not provide information on specific lipid composition. Oil Red O is a lysochrome diazo dye that reacts with neutral lipids and cholesterol esters, but it is relatively nonspecific and does not distinguish different lipid species.[141] Light microscopy and TEM analyses further suggest that the crystalline deposits are composed of lipids, but we still have no indication regarding the identity of the lipids present. Therefore, it will be critical to profile the ocular lipid composition of the knockout mice in future studies, utilizing more advanced methodology such as matrix-assisted laser desorption ionization

(MALDI) imaging. In summary, Cyp4v3$^{-/-}$ mice exhibit phenotypic characteristics that correspond well to BCD in humans, in terms of both progressive crystal deposition in the eye and the systemic nature of the lipid abnormalities. To validate this knockout mouse as a model of BCD, further detailed characterization is warranted, including electrophysiological changes (ERG), spectral-domain OCT, and optokinetic measurements of visual acuity. Finally, the availability of a mouse model of BCD will allow detailed investigations into the molecular and biochemical changes that occur as a result of genetic defects in CYP4V enzyme activity.

2.6 Acknowledgments

For their invaluable input and guidance, the authors thank Richard G. Weleber, MD, from the Casey Eye Institute at Oregon Health Sciences University; Russell van Gelder, MD, PhD, professor and chair of the Department of Ophthalmology at the University of Washington; and J. Fielding Hejtmancik, MD, PhD, from the National Eye Institute. They also thank the University of Washington Drug Metabolism, Transport and Pharmacogenomic Research program; the University of Washington School of Pharmacy Mass Spectrometry Center; Warren Ladiges, DVM, MS, director of the Department of Veterinary Medicine, at the University of Washington; Kelly Hudkins, MS, for histology and pathology support; H. Denny Liggitt, DVM, PhD, for his veterinary pathology expertise; and Scott Greenwald, PhD, for assistance with fundus imaging.

This work was supported by the University of Washington Drug Metabolism, Transport and Pharmacogenomic Research Program and National Institutes of Health Grant R01 GM49054.

Disclosure: C.M. Lockhart, None; M. Nakano, None; A.E. Rettie, None; E.J. Kelly, None

2.7 Further Characterization

At the time of publication, some key ophthalmologic tests had not yet been conducted in characterization of the *Cyp4v3*$^{-/-}$ mouse model. While I was able to demonstrate morphological changes that arose in ocular tissues of the knockout mice, as well as some physiologic changes such as ocular and systemic dyslipidemia, I was unable to describe any functional changes in vision that occurred as a result of genetic engineering. In collaboration with colleagues at Oregon Health & Science University, we were able to conduct further clinical characterization of the *Cyp4v3*$^{-/-}$ mice to identify functional deficiencies in visual acuity and visual function, and to compare any changes with those observed in BCD patients.

Two diagnostic modalities commonly used in ophthalmology are optical coherence tomography (OCT) and electroretinography (ERG). In BCD patients, there is a wide variation in the type and extent of observed morphological and functional changes, as described in Section 1.3.1 of this dissertation. In nearly all cases there is a progression that occurs over time, typically years, but the specific manifestation of degeneration differs among patients. To capture the both the static and temporal changes in vision, OCT and ERG analyses were performed on cohorts of *Cyp4v3*$^{-/-}$ mice and age-matched controls at 12 and 18 months of age. We also measured visual acuity through optokinetic nystagmus (OKN) testing.

2.7.1 Electroretinogram Background

The electroretinogram (ERG) is a commonly used tool in ophthalmology to measure the electrophysiologic function of the neural and non-neural retina.[142] This is a measure of retinal function and can give insight into the signal conductivity of the neural retinal in transmitting visual signals to the brain. Electrophysiologic testing generally falls into three techniques that

generate slightly different information, so selection of the test depends somewhat on the diagnostic goals. The three techniques are flash electroretinogram (FERG), Multifocal electroretinogram (MfERG), and visual evoked potential (VEP).

2.7.1.1 Flash Electroretinogram

The FERG is designed to evaluate the overall clinical status of the retina by measuring the electrical response to a light stimulus.[142] After the pupil is dilated and the eye is dark-adapted, corneal electrodes are attached and measure the electrical response to flashes of light. The ERG response is measured as the amplitude and implicit time to maximal response of each of three major components of the wave: a-wave, b-wave, and c-wave. The a-wave is produced by photoreceptor cells, located at the outer layer of the retina, and the b-wave is produced by the bipolar and Müller cells located at the inner layer of the retina. The b-wave is most commonly used as a measure of retinal function, but an index measure to estimate the retinal electrical transmission can be determined by the ratio of b-wave/a-wave. The slower c-wave is produced by the retinal pigmented epithelium (RPE) and reflects the integrity of the interaction between RPE and photoreceptor cells.[142]

The FERG contributes diagnostic information for many retinal conditions including retinopathies associated with cancer, melanoma, or toxicity-based etiologies, as well as several congenital conditions such as night blindness and achromatopsia.[142] Limitations in interpretation of the ERG include variation in responses based on age, sex, other ocular pathologies, and even by measurement technique. Drugs and other xenobiotics can also affect the ERG response and may limit the diagnostic usefulness.

2.7.1.2 Multifocal Electroretinogram

The MfERG is conducted similarly to FERG in that the electrical response is measured with corneal electrodes; however, the MfERG test is optimally conducted under normal room illumination rather than under dark-adaptation.[142] Also unique to MfERG is the capability to simultaneously record signals generated in at least 256 discrete points throughout the retina. This allows identification of retinal dysfunction with high spatial sensitivity. The stimulus pattern is an array of hexagonal elements positioned in a 20° to 25° radius from a point of central fixation. Response is measured as a-, b-, and c-waves similar to FERG. Signal amplitude and implicit times of waves are recorded from each discrete measurement point, allowing for identification of small areas of dysfunction.[142]

The MfERG is useful in identifying heterogenous dysfunction, or more subtle pathologies throughout the retina that may be missed on standard examination.[142] Limitations of MfERG include technical difficulty with electrode placement, and eye movement can disrupt the signals.

2.7.1.3 Visual Evoked Potential

The visual evoked potential (VEP) is a technique to measure the electrical transmission of visual stimulus from the retina to the visual cortex of the brain.[142] To record the VEP, electrodes are placed on the scalp over the occipital lobes to measure the electrical signal that reaches the visual cortex. The stimulus is often generated from a black and white checkerboard pattern displayed 50 to 150cm away. The black and white pattern is often alternately reversed, or the checkerboard may be alternated with a diffuse gray to generate the stimulus. The responses to approximately 100 stimulus episodes are recorded. The primary diagnostic use of the VEP is to

address dysfunction of the optic nerve, but is not effective in identifying the underlying cause of dysfunction.[142]

2.7.2 Cyp4v3$^{-/-}$ Murine Electroretinogram

2.7.2.1 Methods

ERGs were performed as previously reported,[143] two to seven days after SD-OCT imaging. Dark-adapted mice were anesthetized with ketamine (100 mg/kg)/xylazine (10 mg/kg), corneas were anesthetized, and pupils were dilated. Mice were placed on a heated platform (37 °C) inside of a Ganzfeld dome coated with a highly reflective paint. Goniovisc, Hypromellose 2.5% (Dynamic Diagnostics, Westland, MI), was applied to the corneas, and platinum signal electrodes were placed on the center of each cornea. Additional reference and ground electrodes were placed in the forehead and tail, respectively. Flash intensities ranged from -4.34 to 3.55 log cd•s/m^2. The number of trials at each light intensity was decreased as the flash intensity increased in order to prevent light adaptation. The time between each flash was increased to allow for pigment regeneration, and ranged from 7 to 70 seconds. Flashes were calibrated as previously described.[143-145]

2.7.2.2 Results

The a- and b-waves of the electroretinograms were recorded for each mouse at 12- and 18 months of age (Figure 2-8 and Figure 2-9). As expected, the amplitude of response increased progressively with increasing light intensity (Figure 2-8). Retinal function declined with age (blue line) compared with testing conducted at the younger age (red line), but the response according to light intensity was similar at the older time point as that from the younger.

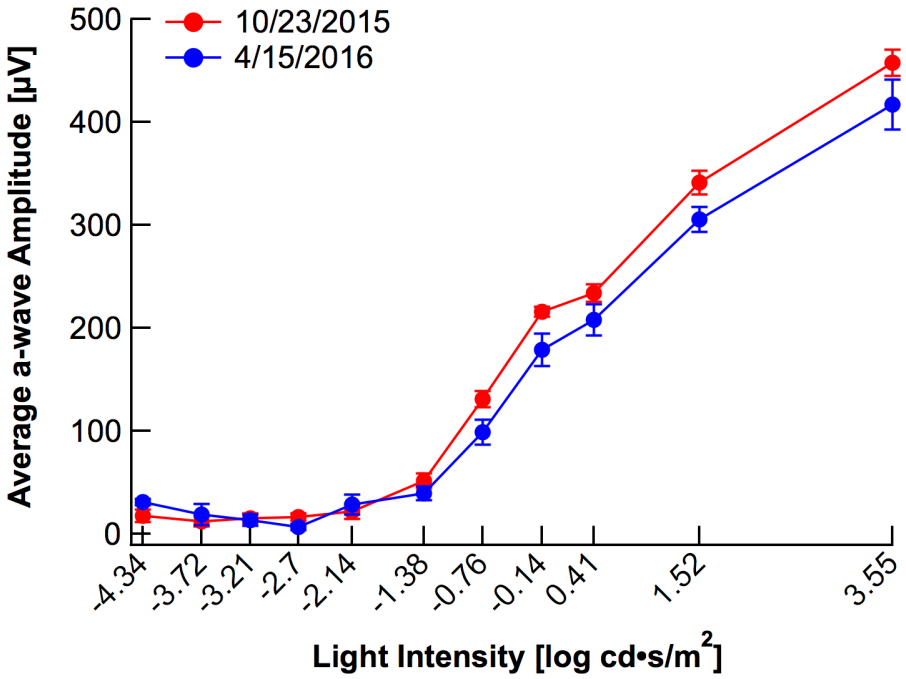

Figure 2-8. Electroretinogram measuring the a-wave in a single longitudinal cohort of mice at 12- and 18-months of age. The a-wave measures the electrical response of the photoreceptor cells.

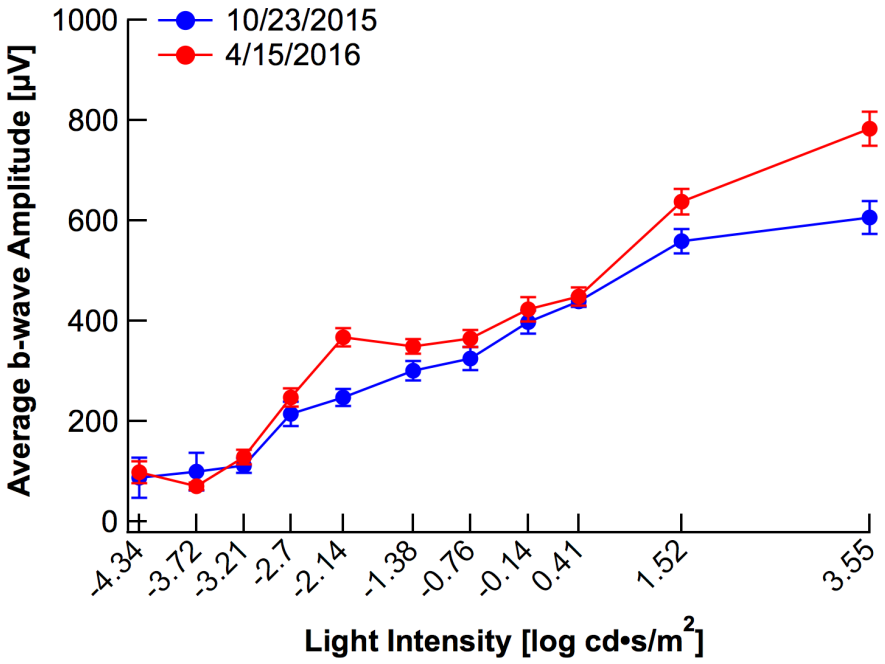

Figure 2-9. Electroretinogram measuring the b-wave in a single longitudinal cohort of mice at 12- and 18-months of age. The b-wave measures the electrical response of the Mueller cells on the surface of the retina, and is often considered the main signal for measuring visual function.

There is a pronounced divergence in electrical response at the higher light intensity in the b-wave measurement (Figure 2-9). Since the difference occurs at the last measure of light intensity, it is unclear whether this is a signal of declining retinal function or an anomaly in measurement or testing.

2.7.3 Optical Coherence Tomography Background

Optical coherence tomography (OCT) is an optical imaging modality that generates high-resolution images of tissue microstructure.[146] It functions similar to ultrasound technology, in which a transducer records the sound waves that are reflected of tissues of different densities; however, OCT records cross-sectional images by recording the backscatter of visible light. While it is possible to image many tissue types with OCT, ophthalmology applications are the most

common.[146] When light interacts with tissues of different densities or optical properties, it is backscattered or backreflected at different velocities. Through complex computer algorithms, the information from the reflected light can be resolved into visual images that describe the cross-sectional morphology of complex tissue such as the retina.[146]

2.7.4 Cyp4v3$^{-/-}$ Murine Optical Coherence Tomography

2.7.4.1 Methods

Retinas were imaged as previously reported.[143,147] Briefly, mice were sedated using 1.5% isoflurane delivered via a nose cone, corneas anesthetized with 0.5% proparacaine, and pupils dilated using a combination of 1% tropicamide and 2.5% phenylephrine. Artificial tears were used to maintain corneal clarity. Mice were seated in a Bioptigen AIM-RAS holder and spectral domain optical coherence tomography (SD-OCT) images were obtained using an Envisu R2200-HR SD-OCT instrument (Bioptigen, Durham, NC).[143,147] Each eye was imaged using linear horizontal scans in the temporal and nasals quadrants and linear vertical scans in the superior and inferior quadrants.

2.7.4.2 Results

Optical coherence tomography images showed the cross-sectional morphology of the *Cyp4v3*$^{-/-}$ murine retinal tissue (Figure 2-10). The images on the left in Figure 2-10 are from 12-month-old mice, while the images on the right are similar images from the same mice. There is no obvious abnormality in the tissue structure at either time point.

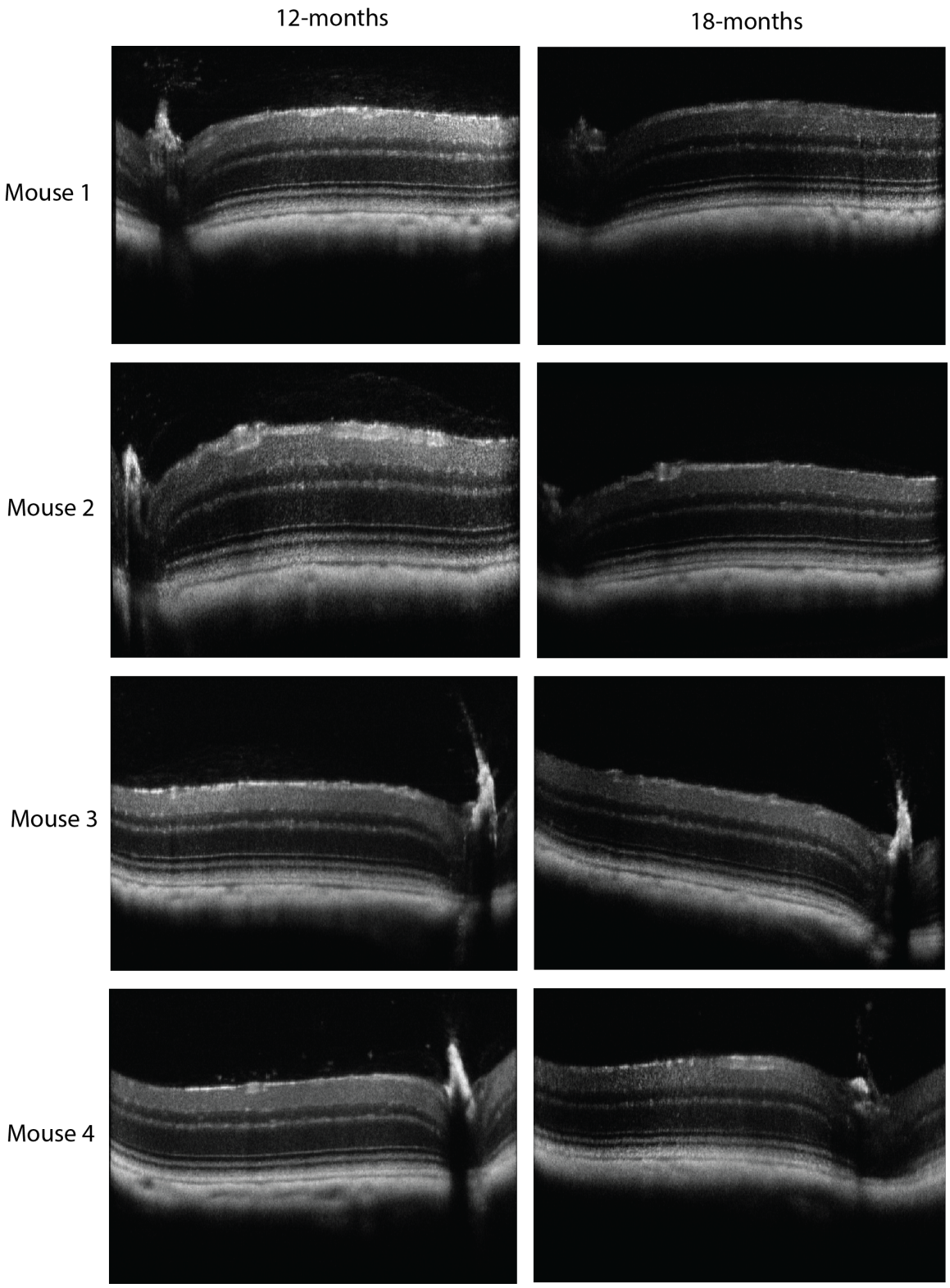

Figure 2-10. *In vivo* Optical coherence tomography images of the retinas of Cyp4v3$^{-/-}$ mice at 12- and 18-months of age.

Based on previous studies where we identified abnormal lipid deposits between the retinal pigmented epithelium (RPE) and photoreceptor cells,[148] we expected to see some aggregation or separation between the RPE and photoreceptor layers. There is no obvious abnormality in the images, but it is possible that the lipid aggregates were simply not detected. Based on histological images (Figure 2-4) and transmission electron microscope images (Figure 2-5), the lipid-based aggregates that appear in *Cyp4v2*$^{-/-}$ mice seem to be relatively flat in relation to the RPE cell layer. Therefore, it is possible that the crystalline deposits visible by fundus imagery (Figure 2-3) are not forming an aggregate that is of sufficient spatial volume to be readily detectable on the scale of optical coherence tomography.

2.7.5 Optokinetic Nystagmus Background

In mice, a common method for testing visual acuity is through optokinetic nystagmus (OKN) testing. In this test, mice are placed on a platform surrounded by computer monitors that display a pattern of vertical lines that rotate either clockwise or counterclockwise. Mice with normal visual acuity will turn their head to follow the moving pattern. These head movements are monitored to estimate visual acuity.

2.7.6 Cyp4v3$^{-/-}$ Murine Optical Nystagmus Testing

2.7.6.1 Methods

Analyses of mouse optokinetic responses were examined using the OptoMotry system (CerebralMechanics, Inc., Lethbridge, Alberta, Canada). Briefly, the system consists of a square array of four computer monitors, an elevated platform on which a freely moving mouse is placed, and an overhead camera to observe the mouse. The computer monitors form a virtual

cylinder of rotating sine-wave vertical gratings, which randomly rotates clockwise or counterclockwise, and mice reflexively respond to the rotating gratings by turning their head in the corresponding direction. The observer registers the mouse behavior by picking either clockwise or counterclockwise.[149] The computer program randomly changes the grating spatial frequency, until the threshold or maximal spatial frequency (cycles/degrees) is reached at 70% of trials correctly registered.[150] Gratings move at the optimal speed (Sp) of 12.0 deg/s, with the temporal frequency (Ft) automatically adjusted by the computer program based on the equation, Ft=Sp x Fs.[150]

2.7.6.2 Results

Optokinetic responses of each mouse in a cohort of evaluated at 12- and 18-months of age. The average spatial frequency (cycles/degrees) was calculated for the tests conducted at each age. Figure 2-11 shows that the visual acuity decreased slightly with age, as expected. It has been reported that healthy C57/BL6 wild-type mice with normal vision have an average visual acuity, as measured by OKN testing, of 0.375 cycles/degrees.[151] The mice in that study were young, at approximately 16 weeks of age at the time of visual testing, so it is difficult to assess the amount of degeneration attributable only to age. Our results did not include wild-type controls, and the youngest mice evaluated were approximately 12-months old. It is unclear whether the visual acuity was abnormal for these mice. Studies are ongoing to compare age-matched, wild-type controls to the *Cyp4v3*$^{-/-}$ mice to determine the presence and extent of visual acuity loss.

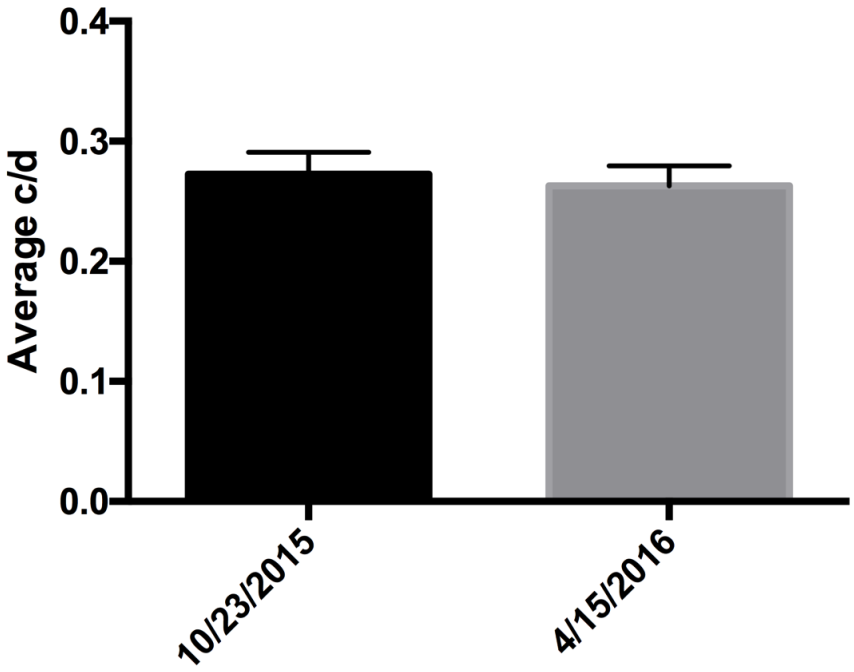

Figure 2-11. Optokinetic Response measured by spatial frequency (cycles/degrees) for a single cohort of mice at 12- and 18- months of age.

2.8 Discussion

Three tests were conducted in a single cohort of *Cyp4v3*$^{-/-}$ mice at two age points: 12-months and 18-months. Electroretinograms were recorded to evaluate electrical function of the retina, optical coherence tomography images were recorded to capture structural information of the retinal tissue, and optokinetic testing was conducted to evaluate visual acuity in the mice.

Electroretinograms showed a typically increasing electrical response to increasing light intensity. While the retinal function appeared to decline at the older time point compared to the younger, this is likely a natural effect of aging. A degraded electroretinogram is not a diagnostic requirement for BCD, but it is possible that the degenerative process observed in BCD patients over time may not follow the same temporal scale in our mice.

Optical coherence tomography images appeared normal in this cohort of mice at both age measurements. From earlier histological studies, the lipid-based aggregates that appeared between the retinal pigmented epithelium and the photoreceptors were relatively flat, and it is possible that the OCT technology was not able to capture any gross abnormalities based on the scale of the image. It is also possible that the retinal degeneration does not occur as extensively in mice as in BCD patients, or may not occur at the same stage of disease.

Optokinetic testing showed some decline in visual acuity, but it is not clear whether the decline was naturally age-related, or due to underlying pathology. Case reports in human BCD patients have shown that visual acuity is not necessarily affected until the stage of extensive degeneration,[80,85] so this test does not necessarily suggest an incomplete phenotype in *Cyp4v3*$^{-/-}$ mice.

In spite of this battery of tests reflecting visual acuity, function, and structure similar to wild-type mice, this model of BCD is still a valuable preclinical platform for assessing potential therapeutic options that may alter the nature or progression of crystalline deposit formation, the hallmark characteristic that defines BCD. Research is ongoing to test a larger cohort of mice, in an effort to better understand the pathophysiology of this blinding disease.

Chapter 3

Longitudinal characterization of function and structure of Bietti crystalline dystrophy: report on a novel homozygous mutation in *CYP4V2*

The work presented in this chapter will be submitted for publication to

The British Journal of Ophthalmology

Corresponding author: Dr. Edward J. Kelly
Department of Pharmaceutics
University of Washington
1959 NE Pacific St.
Health Sciences Building, H272
Seattle, WA 98195
USA
email: edkelly@uw.edu
Telephone: 206-685-4641
Fax: 206-543-3204

Authors: Catherine M. Lockhart, PharmD, PhD
Department of Pharmaceutics
University of Washington
Seattle, WA
USA

Dr. Richard G. Weleber
Casey Eye Institute
Oregon Health & Science University
Portland, OR
USA

Dr. Travis B. Smith
Casey Eye Institute
Oregon Health & Science University

Paul Yang, MD, PhD
Casey Eye Institute
Oregon Health & Science University

Dr. Allan E. Rettie
Department of Medicinal Chemistry
University of Washington
Seattle, WA
USA

Dr. Abhinav Nath
Department of Medicinal Chemistry
University of Washington
Seattle, WA
USA

Keywords: Bietti crystalline, CYP4V2, protein modeling, macular edema

3.1 Abstract

Background: Bietti crystalline dystrophy (BCD) is a rare inherited disorder characterized by fine crystalline deposits in the corneal limbus and retinal posterior pole. In 2004, researchers at the National Eye Institute identified mutations in the *CYP4V2* gene as the cause BCD. Here we describe the first report of a homozygous point mutation in Exon 9 in a patient with BCD, and provide a detailed characterization of function and structure longitudinally over twenty years.

Methods: At regular intervals, the patient underwent ophthalmic examination and testing, which included best-corrected visual acuity (BCVA), fundus color photography, wide-field fundus autofluorescence (AF), wide-field fluorescein angiography (FA), semi-automated kinetic and automated static full-field perimetry, spectral-domain optical coherence tomography (OCT), and ERG. DNA was extracted from buccal swabs and each exon was amplified by standard polymerase chain reaction and validated by gel electrophoresis. Sequencing results were analyzed for homology to known CYP4V2 sequence. A homology model of wild-type CYP4V2 was constructed using the I-TASSER server, the R400C mutant was constructed *in silico*.

Results: The proband is a 47-year-old woman, who is of German ancestry, and the only known affected member of her family. She presented at age 25 with reduced visual acuity and was diagnosed with crystalline retinopathy. Over the next twenty years, her visual acuity, ffERGs, kinetic perimetry, and static perimetry gradually declined, with extensive RPE atrophy in both eyes. Gene sequencing showed a single C>T point mutation located in Exon 9, which results in an arginine to cysteine amino acid change. Computational modeling suggests the observed loss of function is due to loss of a hydrogen bonding interaction with the propionate side chains of the heme prosthetic group.

Conclusion: We present a rare report of a very detailed long-term follow-up of BCD, utilizing visual function tests and multimodal imaging to provide insight into the dynamics of disease progression in BCD. Moreover, this is the first report of a homozygous R400C mutation in CYP4V2 with protein modeling showing a high likelihood of enzyme dysfunction.

3.2 Introduction

Bietti crystalline dystrophy (BCD) is a rare inherited disorder characterized by fine crystalline deposits in the corneal limbus and retinal posterior pole.[152] Patients typically present with asymmetric disease with symptoms of decreased visual acuity, impaired color discrimination, and nyctalopia in the second to third decade of life, and subsequent visual field loss, abnormal electroretinogram (ERG) responses, and legal blindness in the fifth to sixth decade of life. Progressive retinal degeneration involves the retinal pigment epithelium (RPE), choriocapillaris, and photoreceptors, and may be complicated choroidal neovascularization.

In 2004, researchers at the National Eye Institute identified mutations in the *CYP4V2* gene as the cause BCD.[17] Cytochrome P450 4V2 (CYP4V2) is a member of a superfamily of heme-containing monooxygenase enzymes.[79] CYP4V2 is ubiquitously expressed in humans, including liver and ocular tissues, and has substrate specificity for medium chain fatty-acids; however, normal physiological function has yet to be elucidated.[9] Since the genetic cause was first described, over 50 unique mutations have been identified throughout all eleven exons of *CYP4V2*, and any one mutation can cause the disease.[148] BCD is a genetically conferred disease, and transmission generally follows an autosomal recessive pattern, requiring two nonfunctional alleles.[75] Here we describe the first report of a homozygous point mutation in Exon 9 in a patient with BCD, and provide a detailed characterization of function and structure longitudinally over

twenty years.

3.3 Materials and Methods

3.3.1 Patient

This study was conducted in accordance with the tenets of the Declaration of Helsinki and the study protocol was approved by the internal review board at Oregon Health and Science University in Portland, Oregon. Written informed consent was obtained, and the patient was followed for twenty years at the Casey Eye Institute Oregon Retinal Degeneration Center at Oregon Health and Science University. At regular intervals, the patient underwent ophthalmic examination and testing, which included best-corrected visual acuity (BCVA), fundus color photography, wide-field fundus autofluorescence (AF; Optos), wide-field fluorescein angiography (FA; Optos), semi-automated kinetic and automated static full-field perimetry (Octopus 101/900, Haag-Streit, Inc), spectral-domain optical coherence tomography (OCT; Heidelberg Engineering), and ERG. Static perimetry was analyzed and modeled as previously described.[153] Full-field ERG (ffERG) were obtained using Burian-Allen electrodes (Hansen Opththalmic Development Laboratory) according to the International Society for Clinical Electrophysiology of Vision guidelines[154] and as previously described.[155] Multifocal ERG (mfERG) were also obtained using Burian-Allen bipolar contact lens electrodes, and performed according to the International Society for Clinical Electrophysiology of Vision guidelines[156] using the Veris system (Electro-Diagnostic Imaging) with a protocol that used 103 hexagons, a bandpass of 10 to 300 Hz, and a testing time of 8 minutes divided into 60-second segments.

3.3.2 Polymerase Chain Reaction Genotyping

DNA was extracted from buccal swabs from a BCD patient and a healthy control with a Puregene™ DNA Isolation Kit following the manufacturer protocol (Gentra Systems, Minneapolis, MN, USA). Each exon was individually amplified from extracted DNA by standard polymerase chain reaction with the following conditions: After 5 minutes at 94°C, the annealing phase consisted of ten cycles with 15 sec at 94°C, 30 sec at 95°C decreasing 1°C per cycle, and 60 sec at 72°C, then the amplification phase consisted of 30 cycles with 15 sec at 94°C, 30 sec at 55°C, and 60 sec at 72°C. For each reaction, 1 µL of sample DNA was added to a mixture containing 0.25 µL DMSO (Sigma-Aldrich, St. Louis, MO, USA), 5.2 µL 5M betaine (Sigma-Aldrich), 0.25 µL GemTaq™ DNA polymerase (MGQuest, Lynnwood, WA, USA), 4.0 µL GemTaq™ buffer in 1.5 mM $MgCl_2$ (MGQuest, Lynnwood, WA, USA), 200 µM dNTPs (Qiagen, Valencia, CA, USA), 300 µM each amplification forward and reverse primer (Integrated Data Technologies, San Diego, CA, USA), and nanopure water to a final volume of 20 µL. **Table 3-1** lists the forward and reverse primer sequences used for each reaction. Correct PCR amplification was validated by gel electrophoresis using 1.5% agarose gel, and amplicons were isolated using a QIAquick® PCR Purification Kit following the manufacturer protocol (Qiagen, Valencia, CA, USA). Sequencing reactions containing 0.5 µL sequencing primer for either forward or reverse reactions (Integrated Data Technologies, San Diego, CA, USA), 5 µL of isolated amplicons, and 4.5 µL of nanopure water were prepared and submitted for sequencing by Operon (Eurofins Genomics, Huntsville AL, USA). Sequencing results were analyzed for homology to known CYP4V2 sequence using the Basic Local Alignment Search Tool (BLAST, http://blast.ncbi.nlm.nih.gov).

Table 3-1. Primer sequences for PCR amplification and sequencing of CYP4V2 DNA extracted from buccal swabs.

Reaction	Exon	Amplification		Sequencing	
		Forward Primer	Reverse Primer	Forward Primer	Reverse Primer
1	1				
2	2	5'-CTA CCT GGC TTC CTC TAA CAG-3'	5'-TTT TTG TGC TGA AAT GGC TGA A-3'	5'-GAA TTA GTA TAT TCA TCA AA-3'	5'-ATA TAA GGA CAC GTT ATA TT-3'
3	3	5'-AGA TTC GCC TCC TCC CAC CTC AC-3'	5'-ACC TGG ACT CTT GGC CTC TTG ACG-3'	5'-CTA GCT GTA TTC TAG CCA GTA-3'	5'-GCC AGC TGC CAG CTG GAC CT-3'
4	4	5'-TGC CAA AAG CAT TTG AGA ACC TGT-3'	5'-CGC GCT GAA GAG CCC GTC AC-3'	5'-GAA GCT GTT TCA GGA GAA TT-3'	5'-CCG TCA CCC TTT CCC GTC CC-3'
5	5	5'-AGG AAG AAC AGG AAC AGG GAG TAG-3'	5'-CAA CGC AGA AAT TGT TAG CAA TAA-3'	5'-GAC AAA GCA GGA TGT ACG TC-3'	5'-GCA ATA ATT TTT AAA GCC TA-3'
6	6	5'-GCT TCA TGG GAT GCG TAA TAG C-3'	5'-GAA ATG AAC GGT GGG GAT GGT-3'	5'-CCC ACG ATT GCC TTC ATC AAG-3'	5'-GCA CAA CAT CGT GAA TGC AC-3'
7	7	5'-GAG CCT ATG TTG TCG AAA TGT-3'	5'-TCT GAA GAA GTT GAG CTG GTA CTT-3'	5'-AGA AAC TAG CAT ATT TTA TA-3'	5'-CTT CTT TAG TTA AAC TAC TT-3'
8	8	5'-GTT TGC AGT CAC AGT GCA GTC-3'	5'-CCA GCA TCC GGC CTA GTA CAG TC-3'	5'-AAT CCA GAG ACA ATT CAA AA-3'	5'-GTG ACA TCT CTG CAG CAG ACT-3'
9	9 and 10	5'-ATG CCA TGC CTT GAT CCA CCT GT-3'	5'-TGG GCA ATG TCA CAT CAC ATC TCA-3'	5'-TTA GAT GTC TGC ACC CCC AG-3'	5'-AAA TCA CTG TGA GAA ACC CA-3'
10	11	5'-CTC TTC ATC TTT AAC AGG TGT TCC-3'	5'-CAA AAC TCA AAA CTT TTT CTT TGT-3'	5'-AGC CAT TCT GGT TCT CCT TC-3'	5'-TCA AGA TCA GTG GGA TCA AG-3'

3.3.3 Homology Modeling

A homology model of wild-type CYP4V2 was constructed using the I-TASSER server,[157] which relies on both sequence and structural similarities to identify suitable templates for homology modeling from the Protein Data Bank. The highest-ranked of 5 I-TASSER-derived models was selected for subsequent simulations. The R400C mutant was constructed *in silico* using the mutagenesis function in PyMol.

3.3.4 Molecular Dynamics

All molecular dynamics (MD) simulations were performed in Gromacs 4.6.5.[158] Simulations employed the Gromos 54a7 force field parameter set with the SPC explicit solvent model, and heme-thiolate parameters adapted from published topologies.[159,160] Initial homology models were energy minimized using iterative steepest descent and conjugate gradient methods until convergence was achieved. Short (2.5 ps) equilibration trajectories were performed on each starting model using a 0.5 fs time step, and then two independent production trajectories (50 ns each) were generated with a 2 fs time step using an NVT (constant temperature) ensemble. Structures were extracted every 50 ps for analysis.

3.3.5 Statistics

Linear regression was used to determine the best-fit line with R square as the goodness of fit. Extra sum-of-squares F test was used to determine if the slope was significantly different from zero or different between the best-fit slopes from two different data sets. P value of less than 0.05 was considered statistically significant.

3.4 Results

3.4.1 Clinical Structure and Function

The proband is a 47-year-old woman, who is of German ancestry, and the only known affected member of her family. She first presented at age 25 with reduced visual acuity in the right eye of 20/50 (0.4 logMAR), and was diagnosed with crystalline retinopathy. Her history and review of systems was not consistent with hyperoxaluria, cystinosis, drug toxicity, talc retinopathy, or Sjogren-Larsson syndrome. She developed night vision difficulties at age 27, and

reported more rapid vision loss during the course of two pregnancies. Over the next twenty years, the vision in the right eye continued to decline to a current BCVA of 20/200 (1.0 logMAR), whereas the vision in the left eye did not begin to decline until age 30 and is currently her better-seeing eye with BCVA of 20/50 (0.4 logMAR) (Figure 3-1A). The progression of vision loss as measured by logMAR units was linearly correlated with age in each eye with goodness of fit (R^2 =0.9). The slopes of the best-fit line from each eye were significantly greater than zero (right eye, p =0.0017; left eye, p =0.0012), but were not significantly different than each other (p =0.15). The pooled slope equals +0.024 logMAR/year.

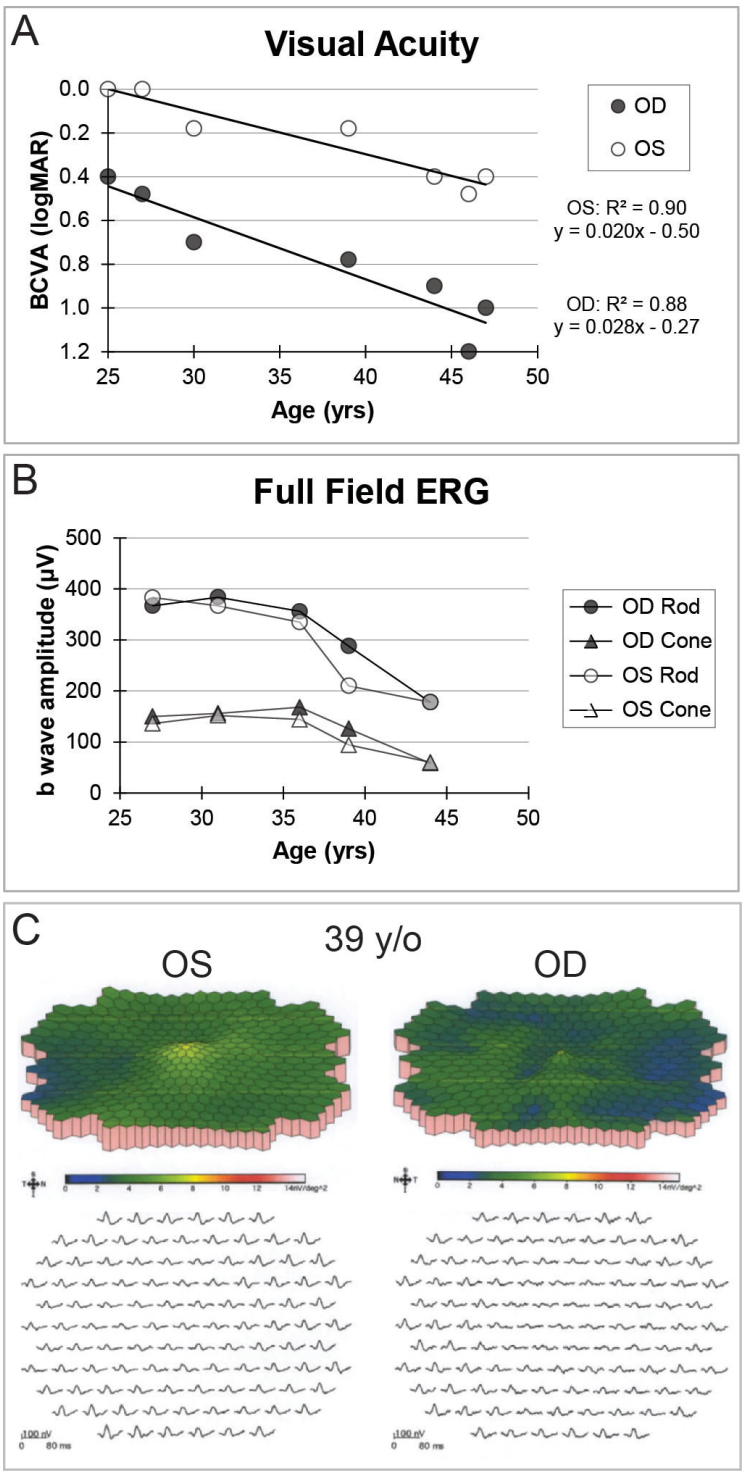

Figure 3-1. A. Best-corrected visual acuity (BCVA) over time with best-fit line depicting progressive decline with slope in each eye that was significantly different than zero, but not significantly different than each other. OD, right eye; OS, left eye; yrs, years. B. Both rod and cone photoreceptor-dependent full-field electroretinogram (ERG) responses declined after 36 years of age in each eye. µV, microvolt. C. Multifocal ERG showed diffuse attenuation that was worse in the right than left eye.

In contrast to the decline in visual acuity, ffERGs were normal in both eyes from 27 to 36 years of age, which was then followed by relatively symmetric progressive attenuation of rod-dependent and cone-dependent responses in both eyes (Figure 3-1B). At age 39, mfERG showed attenuated central macular cone-dependent function that was worse in the right than left eye (Figure 3-1C). Consistent with BCVA and mfERG, kinetic perimetry also showed asymmetric central and paracentral scotoma with respect to the III4e and V4e isopters that was worse in the right than left eye, which deepened and enlarged especially over the past several years (Figure 3-2A). The III4e isopter area plotted over time shows a progressively steep decline from age 39 to 46 (Figure 3-2B). Static perimetry (174 grid, GATE strategy) over the same time period similarly showed progressive constriction of both the central and peripheral fields (see supplemental online video). While retinal crystalline deposits were easily visualized on exam, color photography, and infrared imaging (Figure 3-3A-B), corneal limbal crystalline deposits did not manifest clinically until age 33. Wide-field AF revealed confluent hypoautofluroescence of the posterior pole, which correlated with extensive RPE atrophy in both eyes (Figure 3-3C). At 47 years of age, there was still some intact macular autofluorescence, which correlate with residual RPE and better visual acuity in the left eye. Early phase wide-field FA show confluent hyperfluorescent window defect of the posterior pole with patchy hypofluorescent choroidal atrophy (Figure 3-3D).

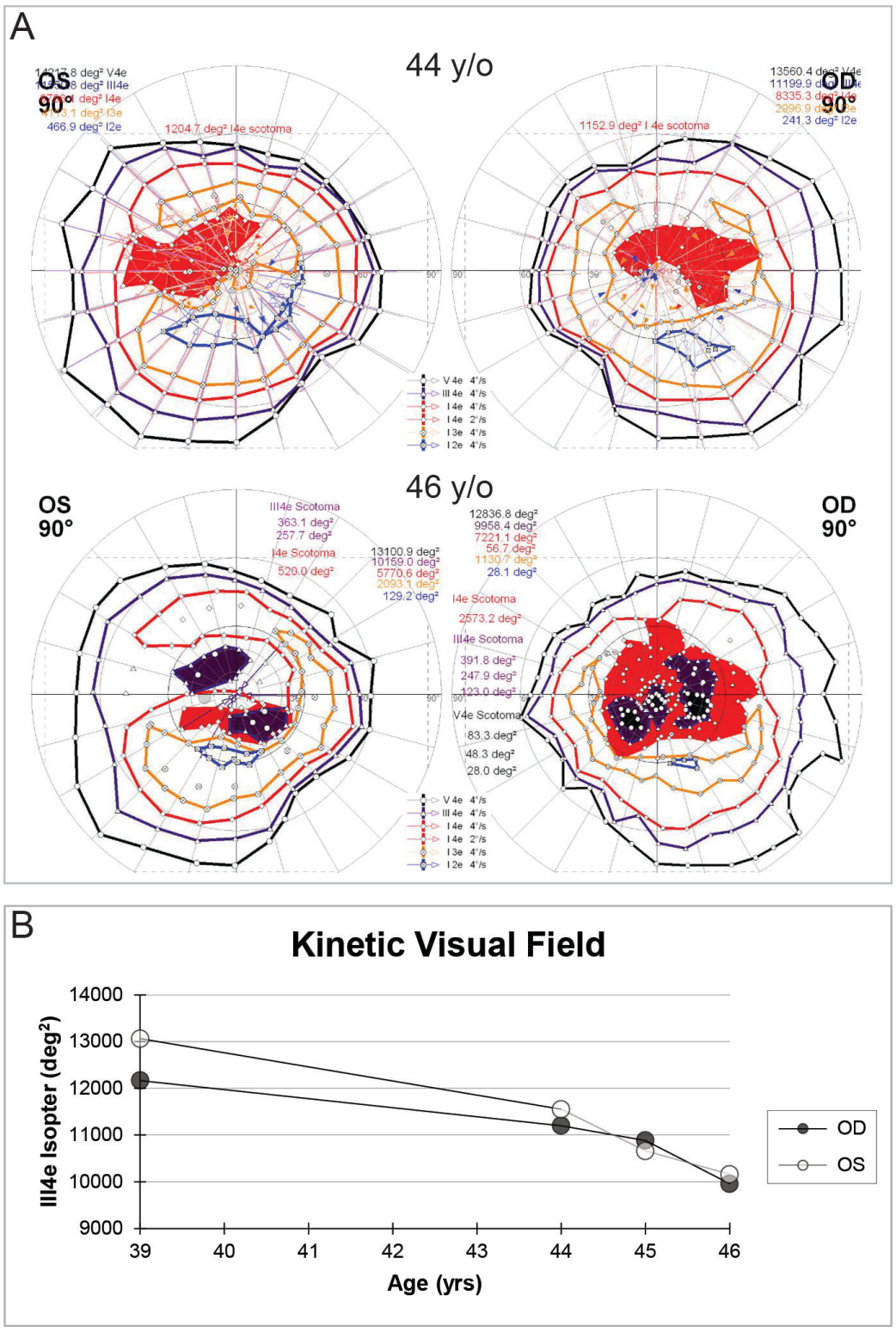

Figure 3-2. A. Kinetic perimetry shows rapid development of worsening central and pericentral scotoma over the course of two years. OD, right eye; OS, left eye; y/o, years old. B. The area of the III4e isopter plotted over time showed a progressive decline in both eyes. deg^2, squared degrees; yrs, years.

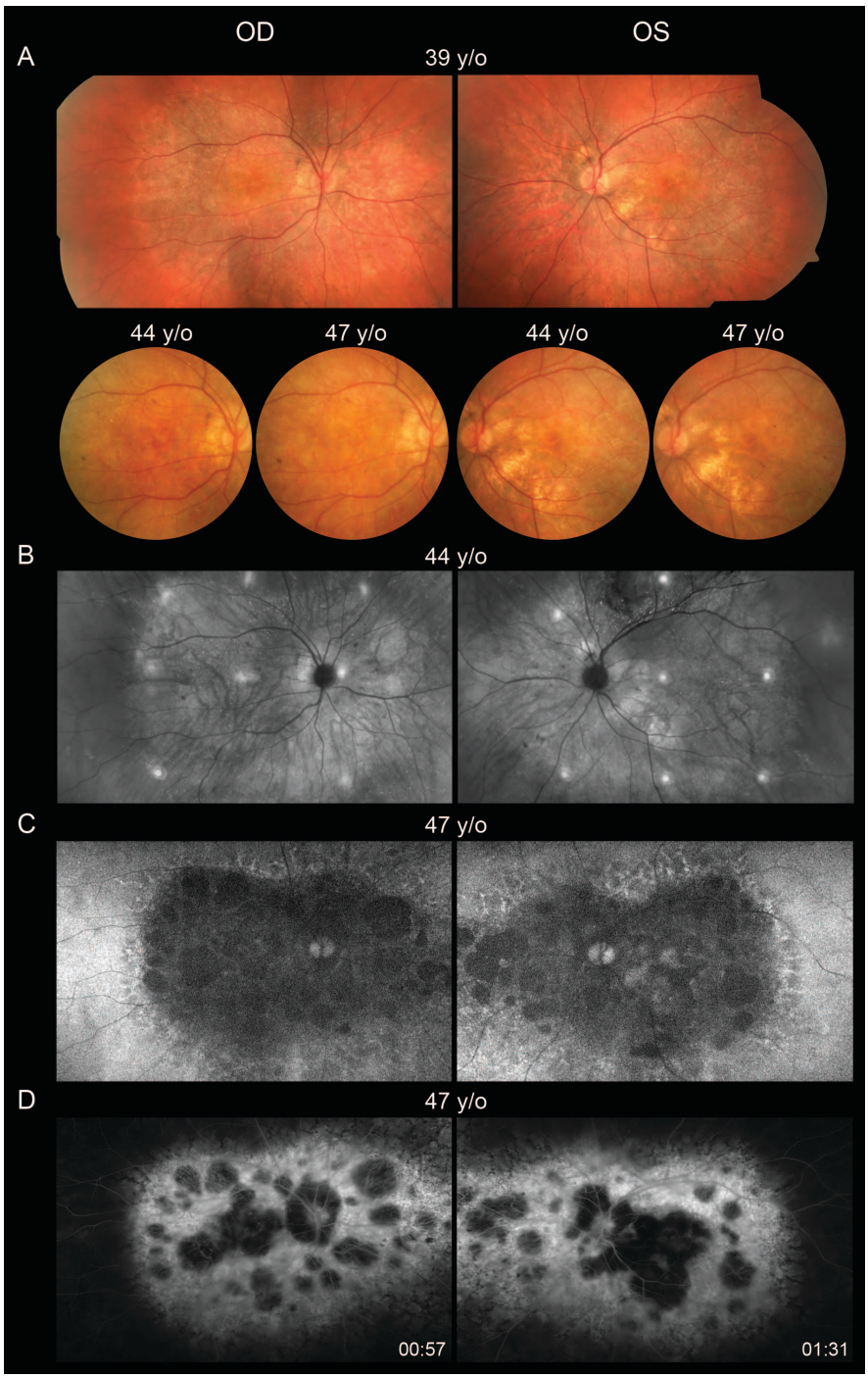

Figure 3-3. A. Color fundus photography show posterior pole crystalline deposits and confluent retinal atrophy, which progresses over time. OD, right eye; OS, left eye; y/o, years old. B. Montage of infrared images highlight the crystalline deposits and areas of retinal atrophy. C. Wide-field autofluorescence show confluent heterogeneous hypoautofluorescence throughout the posterior pole, which is surrounded by lacey hyperfluroescence throughout the mid-peripheral transition zone. D. Early phase wide-field fluorescein angiography show confluent hyperfluorescent window defect of the posterior pole with patchy hypofluorescent choroidal atrophy.

At 44 years of age, she developed cystoid macular edema (CME), which was worse in the right than left eye on OCT (**Figure 3-4**A). Treatment with topical carbonic anhydrase inhibitor, 2% dorzolamide ophthalmic solution, reduced the CME over the course of 6 months, but efficacy was limited by tachyphylaxis. At age 46, treatment with oral carbonic anhydrase inhibitor, acetazolamide 250 mg twice per day, for 6 months revealed near complete resolution of the CME in both eyes. However, during treatment her visual acuity was not significantly improved and eventually she could not tolerate the medication due to systemic side effects. Shortly thereafter, she underwent sinus surgery with a five-day course of oral corticosteroids, and reported that her visual acuity improved dramatically, suggesting an inflammatory component to her vision loss. Late phase FA showed macular petalloid leakage that was mainly in the right eye (**Figure 3-4**B). Subsequent treatment of CME with topical corticosteroids, prednisolone acetate 1% three times per day, and topical non-steroidal anti-inflammatory, bromfenac 0.9% twice per day, showed partial effect in the right eye, and no significant effect in the left eye (**Figure 3-4**A).

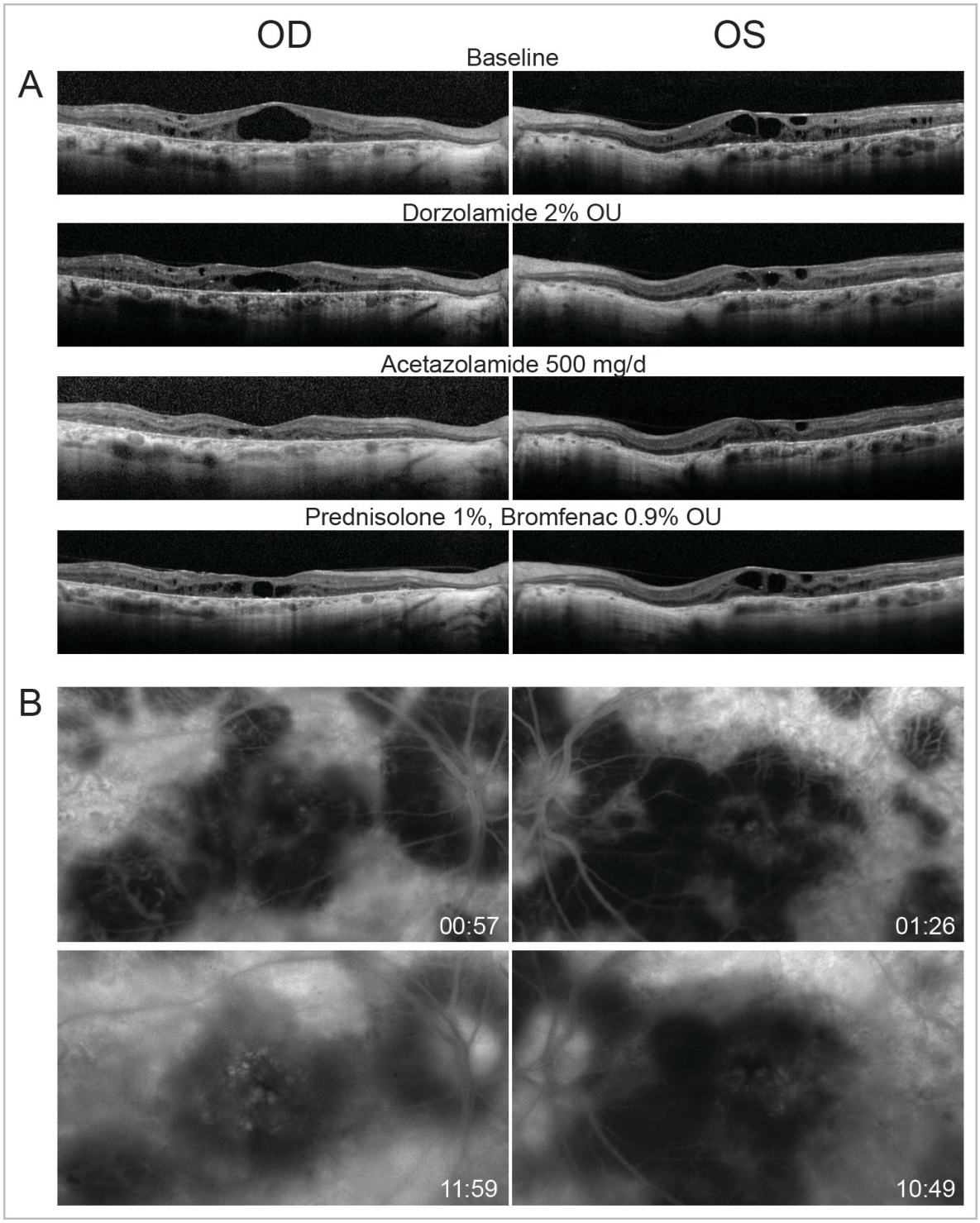

Figure 3-4. A. Optical coherence tomography. Horizontal linear B scans through the fovea show cystoid macular edema in both eyes at baseline, and response to treatment. Retinal pigment epithelial atrophy and outer retinal attenuation with outer retinal tubulations are also observed. OD, right eye; OS, left eye; OU, both eyes; mg/d, milligrams per day. B. Fluorescein angiography show late leakage mainly in the right eye. Hyperfluorescent window defect and hypofluroescent choroidal atrophy are also evident.

3.4.2 Gene Sequencing

Sequencing *CYP4V2* in this BCD patient showed a single point mutation located in Exon 9 (Figure 3-5). The mutation is a C > T change, which results in an arginine to cysteine amino acid change at nucleotide 400 in the protein. This R400C mutation was first reported by Lai et al, in 2007,[101] but in that case the mutation was compound heterozygous with R400H (Figure 3-6). This is the first report of a homozygous point mutation at this location.

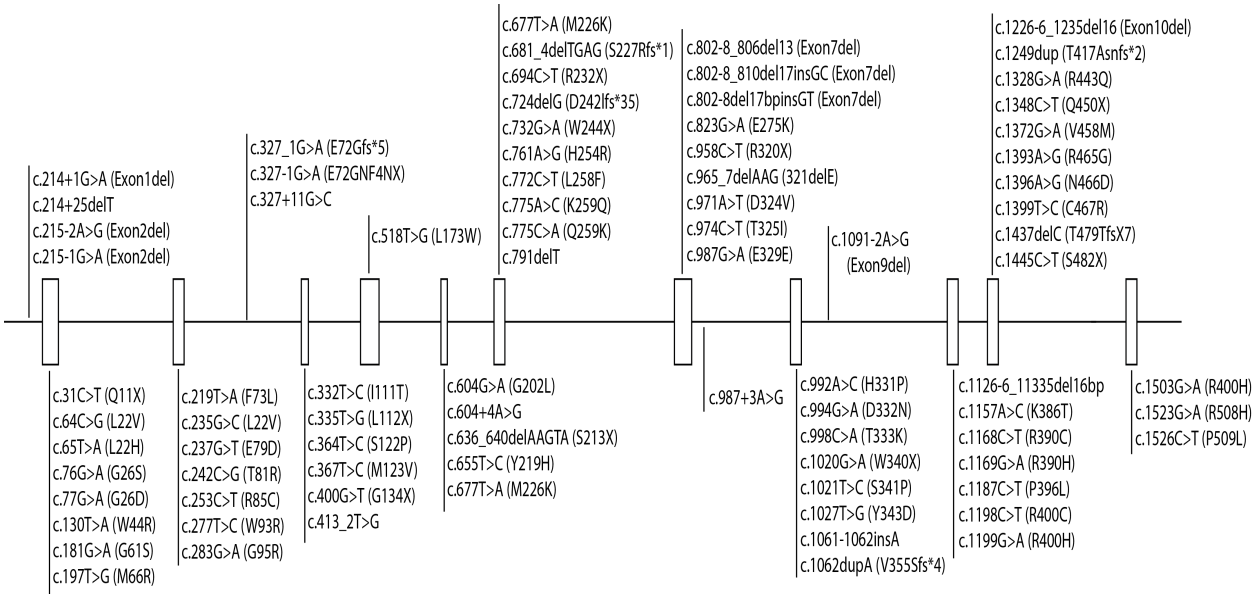

Figure 3-5. CYP4V2 mutations. To date, approximately 80 unique mutations of *CYP4V2* have been reported. At least one mutation has been reported in each of the eleven exons that comprise *CYP4V2*, and any are capable of causing BCD. The most commonly reported mutation is c.802-8_806del13 which results in deletion of Exon 7. The red box highlights the amino acid change that occurs as a result of the homozygous point mutation we describe here.

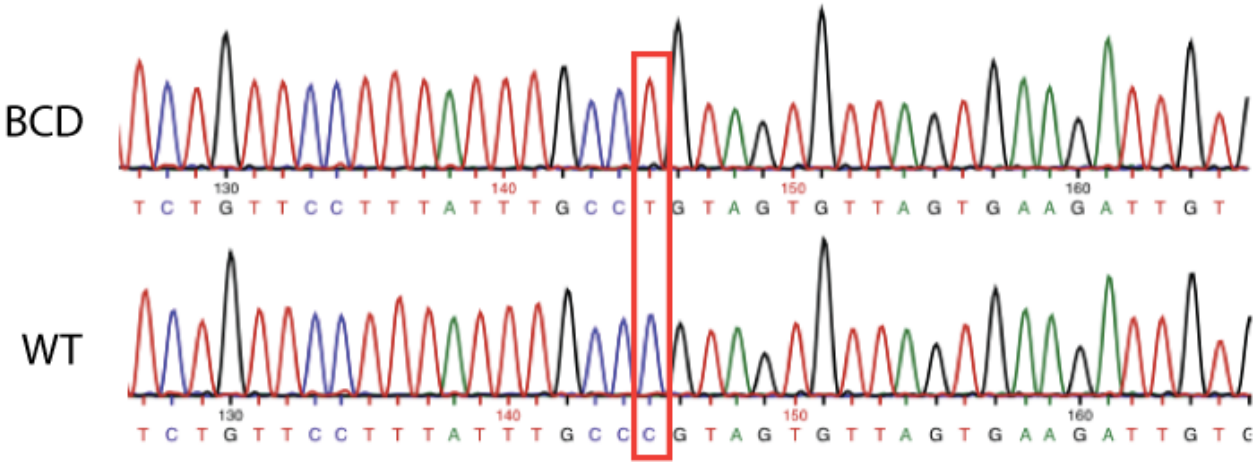

Figure 3-6. PCR sequencing of CYP4V2 in Exon 9. The top panel shows the gene sequence for the BCD patient, and the bottom panel shows the sequence in a healthy control. The red box indicates a homozygous C > T point mutation that leads to an arginine to cysteine amino acid change at nucleotide 400.

3.4.3 Protein Modeling

Molecular dynamics simulations indicate that our homology models of wild-type CYP4V2 and the R400C mutant are globally stable conformations on the timescales accessible to computation. As shown in Figure 3-7a, the root mean square deviation (RMSD) from the initial model, a measure of divergence from the starting state, rapidly (< 10 ns) equilibrates for each of our MD trajectories and then remains at that plateau for the duration of the simulation. This behavior is characteristic of well-behaved simulation systems, and suggests the energy-minimized and equilibrated conformations of CYP4V2 generated by our protocol are physically plausible models of the enzyme.

Computational modeling suggests an intriguing mechanism for the observed loss of function in the R400C mutant. In the wild-type homology model and MD trajectories, R400 is one of a handful of residues involved in hydrogen bonding interactions with the propionate side chains of the heme prosthetic group. The R400C mutant is no longer capable of hydrogen bonding to the propionate groups, as indicated by the increased distance to the heme plotted in

Figure 3-7b. One might expect the loss of this stabilizing interaction to perturb the local environment around the heme. Indeed, in one of our R400C simulations we observed a dramatic and rapid rearrangement of the heme: from its initial orientation facing the active site, the heme flips outward by ~70º so as to expose the propionate group to solvent (Figure 3-7c and Figure 3-7d). The loss of favorable R400–heme interactions thus appears to trigger a compensatory rearrangement of CYP4V2 that leaves it in a presumably inactive, or at least highly perturbed, state, with the heme iron partially occluded and facing away from the active site. Importantly, rearrangements of the protein backbone are limited to residues relatively close to the heme, with the overall fold of CYP4V2 being maintained in our simulation.

Of course, the biological situation is likely to be considerably more complex than the mechanism outlined in our MD trajectories, for several reasons. First, our initial structures are homology models that, while physically plausible and stable *in silico*, are necessarily more tentative guesses at the structure of CYP4V2 than an experimentally determined crystal structure would be. Second, our model makes no attempt to account for the effect of the biological environment, particularly incorporation into a membrane, on the structure of CYP4V2. Third, some CYP4B isoforms are known to display a significant degree of covalent heme adduction to a glutamate residue on the I-helix that would presumably decrease the likelihood of heme rearrangement upon the loss of hydrogen bonding to R400.[161] It is unclear to what extent CYP4V2 displays this modification, although the homologous glutamate (E329) is well placed to conjugate the heme in our homology model. If wild-type CYP4V2 does display a significant degree of covalent heme adduction, then the R400C mutant might exert its activity in two ways: by inhibiting the initial folding of the enzyme into a conformation capable of heme adduction, or by inactivating the fraction of CYP4V2 that fails to conjugate the heme even after proper

folding. In either case, our computational modeling provides clear support for the idea that R400 is a key residue in stabilizing the heme and positioning it for catalysis, and that the R400C mutant would be disrupted in its structure and function by the loss of a hydrogen bond donor in this position.

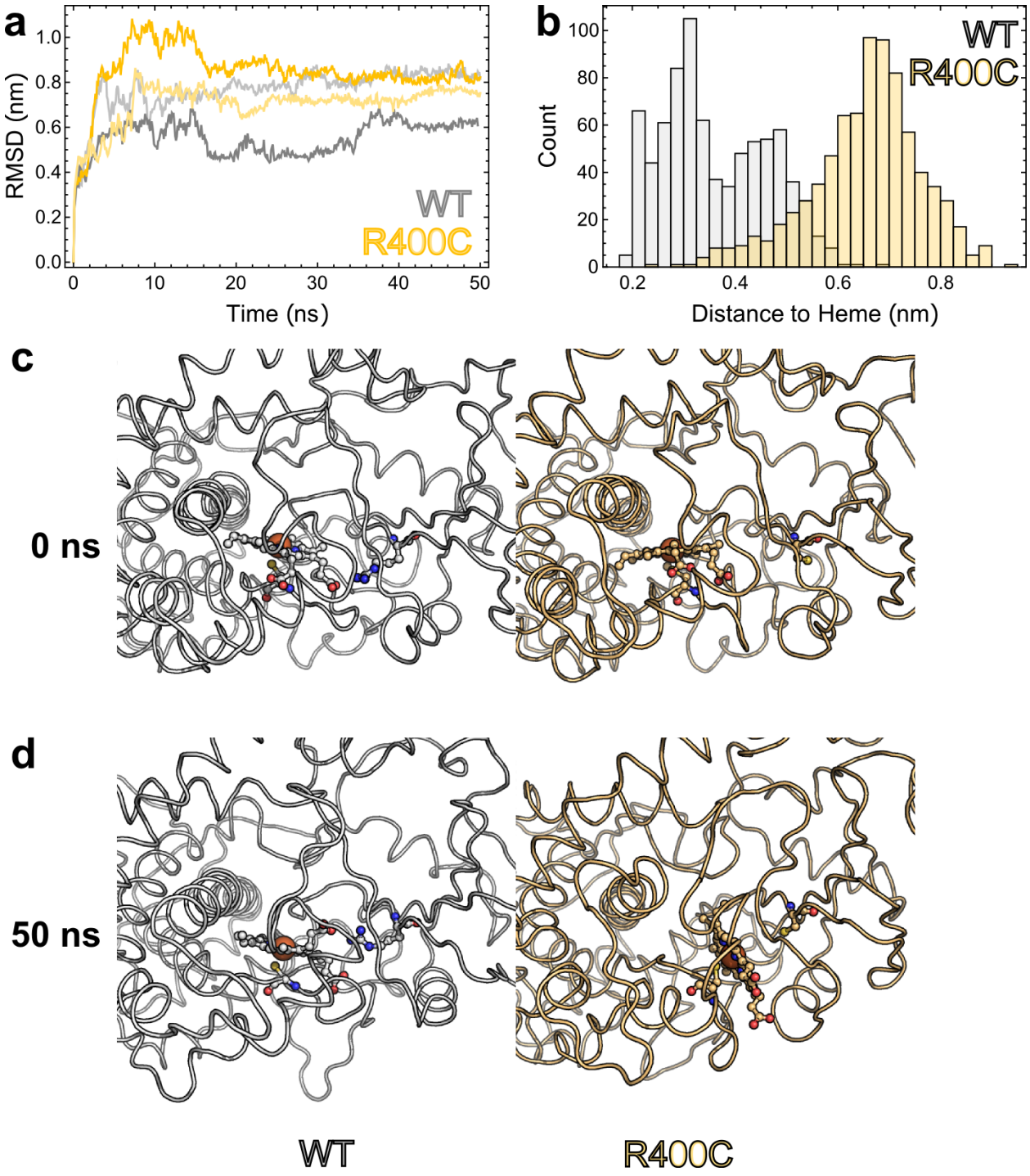

Figure 3-7. Computational comparison of wild-type CYP4V2 with the R400C mutant. A) Root mean square deviation of each trajectory from its starting structure serves to demonstrate that our homology models can feasibly be studied by computational means. The RMSD rapidly achieves a plateau, indicating that the protein as a whole has assumed a locally stable conformation *in silico*. B) Histogram of shortest distances between residue 400 and the heme for each frame of our wild-type and mutant simulations. The wild-type R400 interacts much more closely with the heme group, and spends the majority of its time within hydrogen-bonding distance of the heme

propionates. In contrast, the R400C mutant has lost these interactions and is much more distant from the heme. C) Initial states of our simulated system, with wild-type (white) on the left and R400C (pale orange) on the right. Both enzymes are in highly similar conformations, with the heme facing the active site and apparently available for catalysis. The peptide backbone is shown as a loop, while residue 400, the heme prosthetic group, and the thiolate ligand (C467) are depicted with ball-and-stick representation. D) An illustration of the dramatic changes that can result from the loss of R400. After 50 ns of simulation, the heme orientation is essentially unchanged in wtCYP4V2, but has everted by ~70º in the R400C mutant, presumably contributing to diminished stability or catalytic activity.

3.5 Discussion

The longitudinal case described here is one of the most detailed long-term (over twenty years) characterizations of structure and function in BCD, especially with regard to the correlation of visual acuity, visual fields, and ffERG. To-date, there have been only several other published cases of long-term studies in BCD ranging from 5 to 30 years.[126,162-164] Of those, only two others also report over two decades of clinical follow-up, namely Mansour and colleagues (25 years) and Bagolini & Ioli-Spada (30 years). Our case is consistent with these prior reports in that visual acuity declines with progression of RPE and choroid atrophy, but ffERG attenuation lags other measures of visual function. In agreement with other reports,[83,99] we also found mfERG was better correlated with visual acuity than ffERG in BCD.

In addition, we show that the rate of decline in visual acuity was surprisingly similar for each eye irrespective of the baseline vision, suggesting that the rate of macular degeneration is the same even if one eye lags the other. We also used wide-field AF and wide-field FA to show that RPE and choroidal atrophy in BCD was extensive and concentrated in the posterior pole up to the fifth decade of life. Moreover, we report for the first time, to our knowledge, the long term dynamics of full-field kinetic and static perimetry in BCD, which showed expanding and deepening paracentral and central scotomas. Long-term follow-up of the III4e isopter area revealed that the rate of constriction appeared to increase after age 44, which incidentally, is also

the age for which our patient developed CME. Indeed, it is unknown if treatment of CME had any effect on the rate of progression of either visual acuity or visual fields in this patient. As reported in other cases of BCD,[165] we show that carbonic anhydrase inhibitors were effective in reducing CME, but can be limited by tachyphylaxis and systemic side-effects. We also report for the first time, that topical anti-inflammatory medications may have a partial effect on CME that is associated with significant leakage on FA, but has no effect on non-leaking CME. The prevalence of non-neovascular BCD-associated CME is low and its pathogenesis is poorly understood,[166] however our experience in this case suggests a possible component of inflammation depending on the course of the disease progression. Additional studies in more patients will be required to further elucidate the role of anti-inflammatory therapy in BCD with CME.

3.5.1 Protein Model Limitations

This simulation is from a homology model, and there is not yet any independent experimental evidence that the starting configuration is accurate. Even starting from an accurate model, MD simulations are themselves not 100% accurate at predicting protein dynamics. Even if they were, 50ns is a very short timescale compared to the seconds and minutes that are relevant to catalysis, and longer simulations could show more diverse behavior. Finally, other CYP4s can (some fraction of the time) form a covalent linkage from the I-helix to the heme that could affect this behavior. We are currently working on simulations that include this covalent linkage. Despite these caveats, it's still plausible that a mutation such as R400C could disrupt the hydrogen bond network around the heme and significantly perturb 4V2 conformation and hence function, either during initial folding/heme incorporation, or for the mature protein.

3.6 Conclusion

In conclusion, we present a rare report of a very detailed long-term follow-up of BCD, utilizing visual function tests and multimodal imaging to provide insight into the dynamics of disease progression in BCD. This case of BCD is complicated by CME, which is responsive to carbonic anhydrase inhibitors and partially responsive to topical anti-inflammatory medications, suggesting a potential inflammatory component to the edema. Moreover, this is the first report of a homozygous R400C mutation in CYP4V2 with protein modeling showing a high likelihood of enzyme dysfunction.

3.7 Acknowledgments

3.7.1 Conflict of Interest

Dr. Weleber is a consultant to Novartis, Pfizer, and Wellstat; is a member of the scientific advisory board for Applied Genetic Technologies Corp; and serves on the scientific advisory board for the Foundation Fighting Blindness (the relationship has been reviewed and managed by Oregon Health and Science University). Dr. Weleber also reports having received grants and personal fees from the Foundation Fighting Blindness and Applied Genetic Technologies Corp, and other support from Sanofi-Fovea, all outside the submitted work. In addition, Dr. Weleber has a patent (US patent 8,657,446, Method and apparatus for visual field monitoring, also known as Visual Field Monitoring and Analysis, or VFMA, which has not been issued).

3.7.2 Funding

This work was supported by grants CD-NMT-0714-0648-OHSU (Dr Yang) from the Foundation Fighting Blindness, grant 1K08EY026650-01 from the National Institutes of Health (Dr Yang),

core grant P30EY010572 and unrestricted grant C-CL-0711-0534-OHSU01 from the Foundation Fighting Blindness (Casey Eye Institute), and an unrestricted grant from Research to Prevent Blindness (Casey Eye Institute).

Chapter 4

Epigenetic Regulation of Cytochrome P450 4V2

Catherine M. Lockhart, Krystle Okialda, Edward J. Kelly

The work presented in this chapter will be submitted for publication to

The Journal of Biological Chemistry

4.1 Introduction

Cytochrome P450 4V2 (CYP4V2) is one of 57 functional human isozymes in the cytochrome P450 superfamily of heme-containing monooxygenase enzymes with specificity for ω–hydroxylation of medium-chain fatty acids. CYP4V2 has known ω-hydroxylase activity for the docosanoids eicosapentaenoic acid (EPA, C20:5(n-3)) and docosahexaenoic acid (DHA, C22:6(n-3)) with kinetics comparable to CYP4F2.[9] To date, regulatory mechanisms of CYP4V2 have not been defined. A recent study found evidence in mice to suggest it is subject to regulation by a variety of factors, including specific hormones and diet.[167] Other members of the CYP4 family have been shown to be regulated by peroxisome proliferator-activated receptor alpha (PPARα), but CYP4V2 does not appear to be regulated this way.[168,169] Alternative mechanisms to transcriptional modulators include post-transcriptional regulation via microRNAs (miRNAs), which are small, non-coding RNAs that typically bind complementary sequences on the 3'-untranslated region (UTR) of messenger RNA (mRNA) and results in degradation of mRNA or repression of translation.[169] The 3'UTR of CYP4V2 is quite large, nearly twice the length of the open reading frame (2.8 kb versus 1.5 kb), and similar in size to CYP1B1 (3.1 kb), an enzyme known to be regulated by miRNA.[170]

One condition known to be due to mutations in the gene encoding CYP4V2 is Bietti's Crystalline Dystrophy, a rare, degenerative eye disease, but CYP4V2 may also be implicated in other conditions with varying pathological severity. A potential risk factor for deep venous thromboembolism is a common, non-synonymous polymorphism in CYP4V2 (rs13146272, K259Q),[125,171,172] which is in linkage disequilibrium with SNPs in two genes known to be related to coagulation, Factor XI (F11) and pre-kallikrein (KLKB1). This was first thought to explain the association between rs13146272 and DVT; however, more detailed genetic analysis showed

individuals possessing the A-C-T haplotype corresponding to CYP4V2 rs13146272, F11 rs2036914, F11 rs2289252 were at highest risk of deep venous thromboembolism.[171] This suggests there may be a modulating influence of the CYP4V2 SNP on the two more directly acting F11 polymorphisms. CYP4V2 expression has also been inversely correlated with tumor grade in breast cancer.[173] Better understanding of inter-individual variability in CYP4V2 expression in normal populations may also provide a foundation to understand the pathophysiology of these diseases. There is a growing body of research on the role of microRNAs (miRNAs) in the post-transcriptional regulation of various CYP isoforms.[174]

4.2 MicroRNA

MicroRNAs were first discovered in 1993 by researchers who found that a gene in *C. elegans* known to regulate larval development did not produce a protein, but instead produced two short RNA strands.[175] One strand was approximately 61 nucleotides long, predicted to form a stem loop and be the precursor to the other strand that was approximately 22 nucleotides long. The nucleotide sequences of these short RNA segments were complimentary to multiple sites in the 3' untranslated region (UTR) of the *lin-14* gene. It was further identified that when these regions in the 3'UTR were deleted through mutation, there was an abnormally high level of LIN-14 nuclear protein present in the cells.[176] This suggested a negative regulatory role associated with these 3'UTR sequences. Furthermore, it was shown that binding to these 3'UTR sequences reduced the amount of LIN-14 protein without affecting levels of the *lin-14* messenger RNA (mRNA).[177] These studies identified what would become the first in a class of small, regulatory RNAs that were later called microRNAs (miRNAs).

To initiate regulatory function, miRNA must be transcribed from genomic DNA in the nucleus of a cell.[177] Figure 4-1 illustrates the steps in transcription and regulatory function of

mature miRNA in mammalian cells. First, the miRNA gene is transcribed by RNA polymerase II into primary miRNA (pri-miRNA) that forms stem loop structures in the nucleus.[178] The pri-miRNA is cleaved into pre-miRNA by Drosha, and transported out of the nucleus into the cytosol by Exportin. In the cytosol, pre-miRNA is cleaved further by Dicer to produce a double-stranded segment of approximately 22 nucleotides in length.[177] The double stranded RNA segment is cleaved into a single stranded miRNA, which is incorporated into the RNA-induced silencing complex (RISC). RISC facilitates binding to the 3'UTR of the target mRNA, and once bound, the miRNA complex represses gene expression typically by either blocking the ribosome to prevent protein translation, or by accelerating degradation of the target mRNA.[177,178] It has been estimated that MicroRNAs target approximately 60% of the human transcriptome.[179]

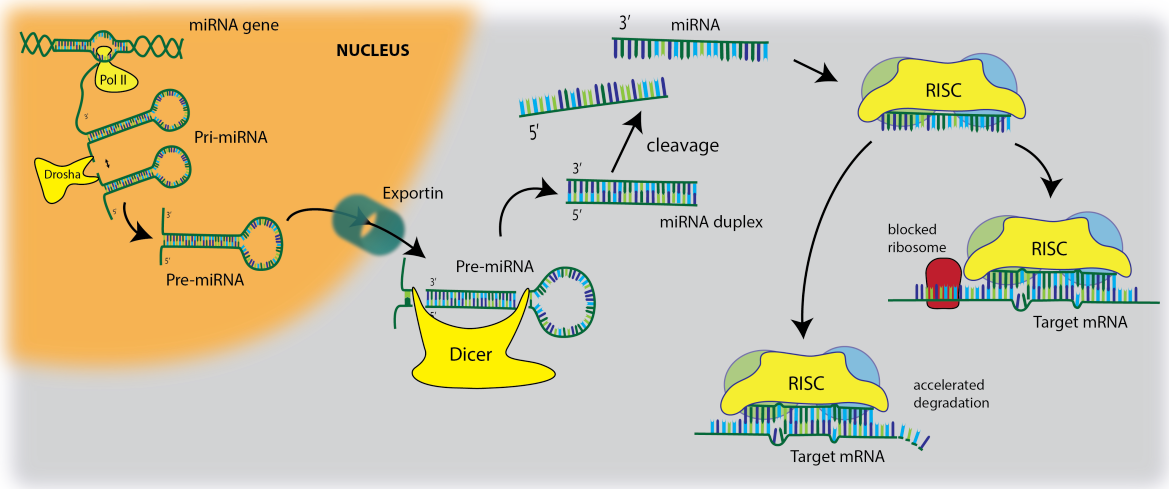

Figure 4-1. MicroRNA. The biogenesis and regulatory function of microRNA in human cells. The miRNA gene is first transcribed into RNA in the nucleus by RNA polymerase II (Pol II). The RNA transcript generally assume a stem loop structure, and is referred to as primary-miRNA (pri-miRNA). Pri-miRNA is then cleaved by Drosha into pre-miRNA, which is transported to the cytosol via Exportin. The pre-miRNA is cleaved further by Dicer, and the resulting miRNA duplex is cleaved into a single complement strand. The mature miRNA is incorporated into an RNA-induced silencing complex (RISC), which facilitates binding to the 3'UTR of mRNA in the cytosol. Once bound, the miRNA represses protein translation by either blocking the ribosomal activity, thus preventing translation, or through accelerated degradation of the target mRNA.

MicroRNAs are implicated in the regulation of a number of biological processes, such as development, cell differentiation, apoptosis, as well as contributing to the pathogenesis of human disease.[180-182] MicroRNAs may also regulate drug metabolizing enzymes by acting directly on their transcripts or indirectly by targeting factors, such as nuclear receptors and transcription factors, that regulate drug metabolizing enzymes.[174] Research efforts on the role of microRNA regulation of genes involved in drug/xenobiotic absorption, distribution, metabolism, and excretion is rapidly expanding, including their impact on cytochrome P450 function. Here we describe the selection and mechanistic evaluation of potential miRNA candidates in regulation of CYP4V2 expression.

4.3 Materials and Methods

4.3.1 Human Liver Samples

Human liver microsomes were prepared as described by Paine et al. (1997).[183] Total mRNA from the human livers was extracted and normalized to 200 ng/μL. Whole genome expression measurement was carried out using the Illumina HumanRef08 v.2 Expression BeadChips according to the manufacturer's protocol. All samples were measured in duplicate and each sample and replicate was randomized between processed batches of 24 arrays analyzed on different days. Raw signal intensity measurements were processed using the Illumina BeadStudio software v.2.3.41 using the 'average' normalization function and replicate data from each liver sample was averaged to obtain a final value. Use of the samples was classified as non-human subjects research by the University of Washington Human Subjects Division.

4.3.2 Antibody production and assessment of cross-reactivity

Anti-CYP4V2 antibody production was carried out by R&R Research (Stanwood, WA) using purified CYP4V2 as the antigen. Briefly, two rabbits were immunized with the purified CYP4V2 protein supplemented with complete adjuvant along with 3 boosts (1 mg total). Twelve weeks after initial immunization, the animals were sacrificed and sera isolated. Polyclonal IgG was isolated from the crude sera of pre- and post-immunized animals following fractionation with a saturated ammonium sulfate solution. The cross reactivity of the anti-CYP4V2 IgG towards other CYP4 enzymes (Supersomes® and purified CYP4B1 expressed in E.coli) was determined from Western blots of 0.2 pmol of purified CYP4V2, 1 pmol of Supersomes® (CYP4A11, CYP4F2, CYP4F3A, CYP4F3B, CYP4F12) and 1 pmol of purified rabbit CYP4B1.[9]

4.3.3 SDS-PAGE and Western Blot Analysis

The human liver microsomes (20 ug microsomal protein) were mixed with sample buffer (250 mM Tris pH 6.8, 8% SDS, 40% glycerol, 20% BME, 0.004% bromophenol blue) and boiled for 5 minutes. Samples were separated on 15% SDS-polyacrylamide gels (100 V for 90 min at room temperature) using running gel buffer (250 mM Trizma base, 200 mM glycine, 3.5 mM SDS) and transferred to nitrocellulose membranes (90 V for 90 min) using cold transfer buffer (25 mM Trizma base, 200 mM glycine, 5 M methanol). Following the transfer, membranes were blocked overnight at 4°C with Odyssey Blocking Buffer (LI-COR Biosciences, Lincoln, NE) containing 3% goat serum (Life Technologies, Grand Island, NY). Membranes were incubated with rabbit anti-human CYP4V2 in Odyssey Blocking Buffer (1:3,000) for 1 hour at room temperature and washed with TPBS (0.3% Tween-20 and 1X phosphate buffered

saline) and 50 mM sodium chloride (4X15 min). Following the washes, membranes were incubated with goat anti-rabbit IgG secondary antibody conjugated with IR680 dye (1:30,000; Fisher Scientific, Pittsburgh, PA). After washing with TPBS (4x15 min), the CYP4V2 bands were visualized and quantified using the Odyssey system after normalization to β-actin.

4.3.4 MicroRNA Microarray

Total RNA (containing the miRNA fraction) was isolated using the miRNeasy Mini kit (Qiagen Inc., Valencia, CA) according to the manufacturer's established protocol. The quality of the total RNA was evaluated using an Agilent 2100 Bioanalyzer (Agilent Technologies Inc., Palo Alto, CA). Only samples with high integrity and adequate quantity were used for further analysis. Initial miRNA microarray analysis was performed on six livers with the highest CYP4V2 mRNA levels and six livers with the lowest CYP4V2 mRNA levels, to determine differential expression of miRNAs between the two groups. The entire liver bank was subsequently analyzed by miRNA microarray to validate potential miRNA regulators identified in initial study.

The Functional Genomics and Proteomic Core Laboratory at the University of Washington (https://www.iths.org/resources/directory/listing/drc-quantitative-and-functional-proteomics-core-university-of-washington) used the GeneChip miRNA 2.0 Array (Affymetrix Inc., Santa Clara, CA) to measure levels of miRNA expression, following the manufacturer's established protocol to process the total RNA samples and arrays using the FlashTag Biotin HSR kit (Genisphere LLC, Hatfield, PA). Briefly, samples were processed with a poly(A) tailing reaction followed by ligation of the biotinylated signal molecule containing Genisphere's proprietary 3DNA dendrimer signal amplification technology to the target RNA sample.

Samples were then hybridized to the Affymetrix array, followed by washing, staining and scanning of the arrays which were carried out using the manufacturer's established protocols.

4.3.5 Luciferase Reporter Vectors

A luciferase reporter vector containing the entire human CYP4V2 mRNA 3'UTR (2.8 kb), including the candidate miR146b-5p binding site at nt 2115-2144, as identified using the online resource MicroInspector, a negative control empty vector, synthetic miRNAs and a miRNA inhibitor as bacterial stabs was obtained (GeneCopoeia, Rockville, MD). Figure 4-2 shows the plasmid maps for each vector.

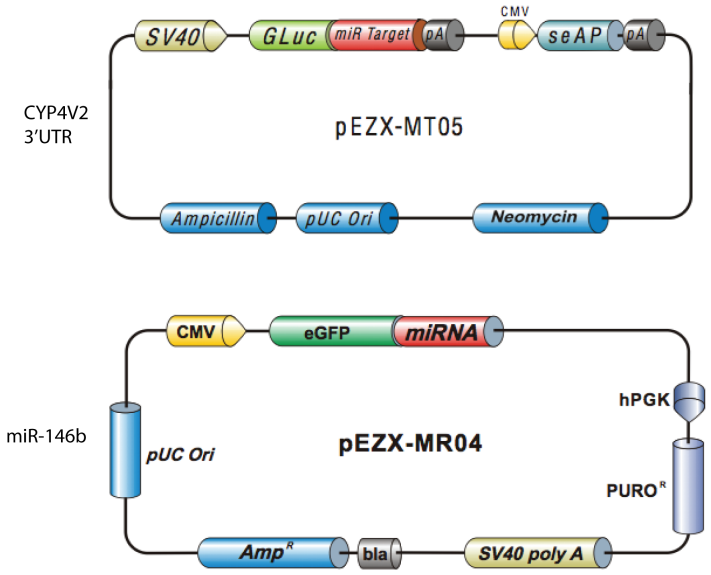

Figure 4-2. Plasmid maps for three constructs for transfection. (A) CYP4V2 mRNA 3'UTR with neomycin (G-418) resistance selection cassette. (B) synthetic miR-146b for overexpression with a puromycin resistance selection cassette. (C) shRNA inhibitor of miR-146b. Scrambled control vectors were identical except the genetic material is scrambled and thus inactive.

Samples from each bacterial stab were cultured overnight in Lennox LB Broth (Sigma-Aldrich, St. Louis, MO) at 37°C with moderate shaking. Plasmids were prepared from the

bacterial cultures using the Plasmid Midi kit (Qiagen Inc., Valencia, CA) according to the manufacturer's established protocol.

4.3.6 HepG2 Transfection and Luciferase Activity

HepG2 cells were cultured in Dulbecco's Modified Eagle Medium: Nutrient Mixture F-12 (DMEM/F12, Gibco-Life Technologies, Carlsbad, CA) supplemented with 10% Fetal Bovine Serum (FBS, Gibco-Life Technologies, Carlsbad, CA) and 1% penicillin/streptomycin (Gibco-Life Technologies, Carlsbad, CA).

HepG2 cells ($1 – 2 \times 10^4$ cells/well) were plated into 12-well plates and allowed to attach overnight to achieve approximately 40% confluence. The following day, cells were stably transfected with plasmids either containing the CYP4V2 3'UTR (n = 12 clones) or a scrambled negative control (n = 12 clones) using FuGene transfection reagent, following the manufacturer protocol (Promega, Madison, WI). Stable clones were selected over approximately two weeks by incubation in media as described above containing 1000 ng/mL G-418.

The procedure occurred in three steps: stable transfection with luciferase reporter clone, stable transfection to over-express miR-146b-5p, and transient transfection with a miR-146b-5p inhibitor (Figure 4-3).

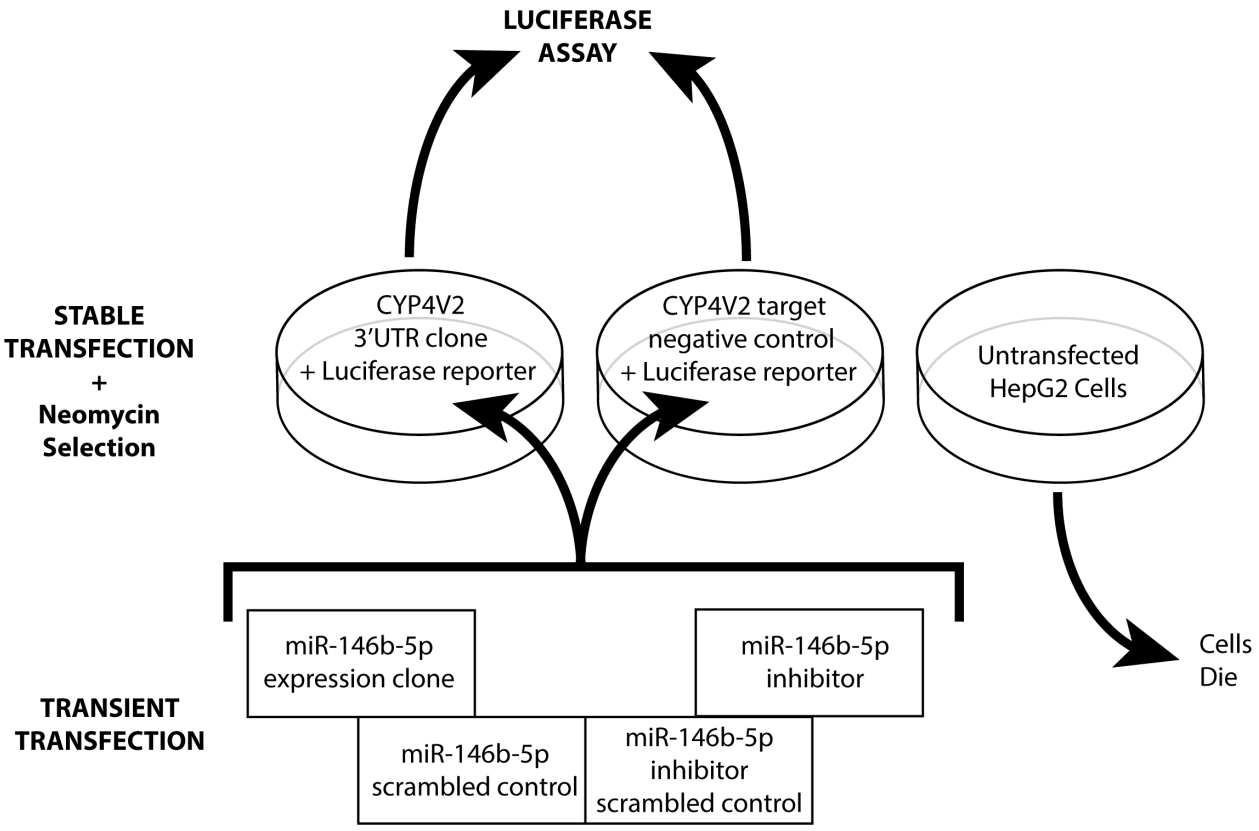

Figure 4-3. Luciferase experimental design. Experimental design for assessing the function of miR-146b-5p on the CYP4V2 3'UTR, utilizing luciferase reporter vector in a transfected HepG2 cell line.

Baseline luciferase and activity was evaluated using the SecretePair® Dual Luminescence Assay according to the manufacturer protocol (GeneCopoeia, Rockville, MD), and measured with a Synergy HTX plate reader (BioTek Instruments, Winooski, VT). Secreted alkaline phosphatase (SeAP) was also measured as a transfection efficiency control. Four clones from each cell line, transfected with the CYP4V2 target clone or scrambled negative control, were stably transfected with a miR-146b expression clone to over-express the miRNA, or a scrambled control, following the same protocol described above. Stable clones were selected under pressure with 4 ng/mL puromycin in the growth medium described above.

4.3.7 ARPE-19 Assay

4.3.7.1 ARPE-19 Culture and Transfection

ARPE-19 cells (American Type Culture Collection, Manassas, VA) were plated on a 16-well microscope slide, and allowed to expand to confluence. Cells were transfected with plasmids to overexpress miR-146b-5p, or a non-targeting control miRNA (Figure 4-4). Transfections were performed using FuGene (Promega, Madison, WI) transfection reagent at a 3:1 (FuGene:DNA) ratio following the manufacturer protocol. After 24 hours, the transfection medium was removed and replaced with standard growth medium. After an additional 72 hours, cells were fixed in methanol for 20 minutes, and rinsed in phosphate buffered saline (PBS).

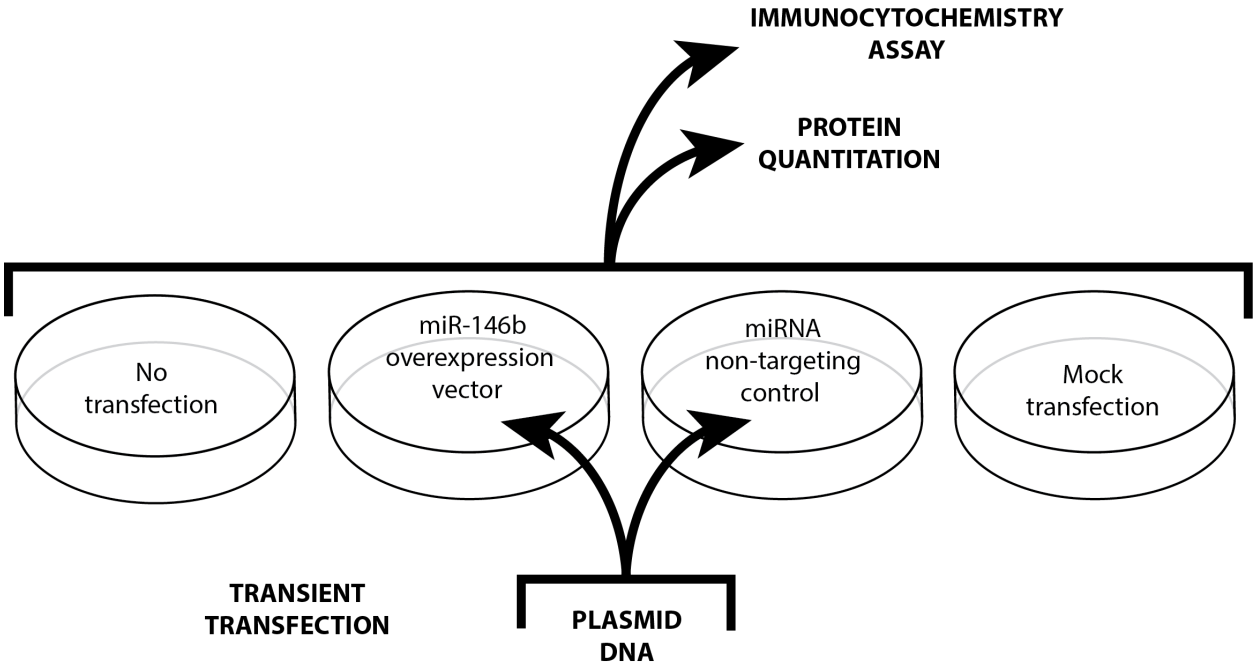

Figure 4-4. ARPE-19 transfection experimental design. Experimental design for assessing the mechanism of miR-146b-5p regulation of CYP4V2 protein expression in an immortal retinal pigmented epithelial cell line.

4.3.7.2 Immunocytochemical Staining.

After fixation in methanol for one hour, cells were rinsed and placed in blocking solution (recipe) for one hour before incubation with primary antibodies. ARPE-19 cells were first incubated for one hour at room temperature with anti-CYP4V2 and with a mouse monocolonal antibody for GFP (Thermo Fisher Scientific, Waltham, MA). The secondary antibody incubation was performed with a mixture of anti-rabbit IgG antibody conjugated with AlexaFluor593 (Thermo Fisher Scientific, Waltham, MA) and anti-mouse IgG antibody conjugated with AlexaFluor464 (Thermo Fisher Scientific, Waltham, MA). Cells were incubated for one hour at room temperature, before washing and sealing with a microscope cover slip. The processed samples were analyzed by using a Nikon Ti-S microscope (Nikon Instruments, Inc., Melville, NY, USA), and the ratio of CYP4V2 to GFP signal was determined in n = 10 cells per transfection, performed in triplicate using ImageJ software (National Institutes of Health, USA).[9]

4.3.7.3 ARPE-19 Protein Quantitation

ARPE-19 cells cultured under the conditions described above were dissociated using Trypsin – EDTA 0.05% (Gibco Life Technologies, Carlsbad, CA) rinsed, and concentrated into a cell pellet. Quantitation was done in collaboration with Dr. Bhagwat Prasad, who has completed design and production of a peptide specific for CYP4V2, allowing for absolute quantitation using validated LC-MS methods.[72] Two unique signature peptides (SVSEDCEVAGYR and TILSCILR) were selected for LC-MS/MS quantification of CYP4V2. The cells were homogenized in the homogenization buffer (Proteoextract kit, Calbiochem). The samples were then incubated with deoxycholate (denaturation), dithiothreitol (reduction), iodoacetamide (alkylation) in ammonium bicarbonate buffer (50 mM, pH 7.8). Methanol:water:chloroform

extraction was performed and the desalted sample pellet was then digested by trypsin (protein:trypsin ratio of 25:1) at 37 °C for 18 h. The reaction was stopped by 80% acetonitrile in water containing 0.1% formic acid. The samples were centrifuged at 4000 xg for 5 min and the supernatant was transferred to LC-MS vials. Targeted LC-MS/MS analysis was performed using AB Sciex 6500 triple-quadrupole mass spectrometer coupled to Acquity UPLC system.

4.3.8 Statistical Analysis

Linear regression analysis was performed using GraphPad Prism 5.0 to correlate CYP4V2 mRNA and CYP4V2 protein levels and miR-146b-5p expression and CYP4V2 protein levels.

4.4 Results

Human liver samples (n = 55) were obtained from the University of Washington School of Pharmacy Human Liver Tissue Bank (Seattle, WA). Donor demographics are shown in Table 4-1. Most donors were Caucasian, and ranged in age from seven to 70 years.

Table 4-1. Demographic characteristics of human liver donors (N = 55)

Age Range (years)		7 – 70
Sex (N)	Male	29
	Female	26
Ethnicity (N)	Caucasian	52
	Asian	1
	Black (non-Hispanic)	2

Western blotting of available human liver microsomes (n=10) from the two groups was done using purified CYP4V2 protein standards to quantify protein concentrations (Figure 4-5). CYP4V2 protein concentrations were normalized to amount of microsomal protein loaded (20

ug). The six liver samples with the highest (Group 1) and lowest (Group 2) CYP4V2 mRNA levels were selected for further analysis.

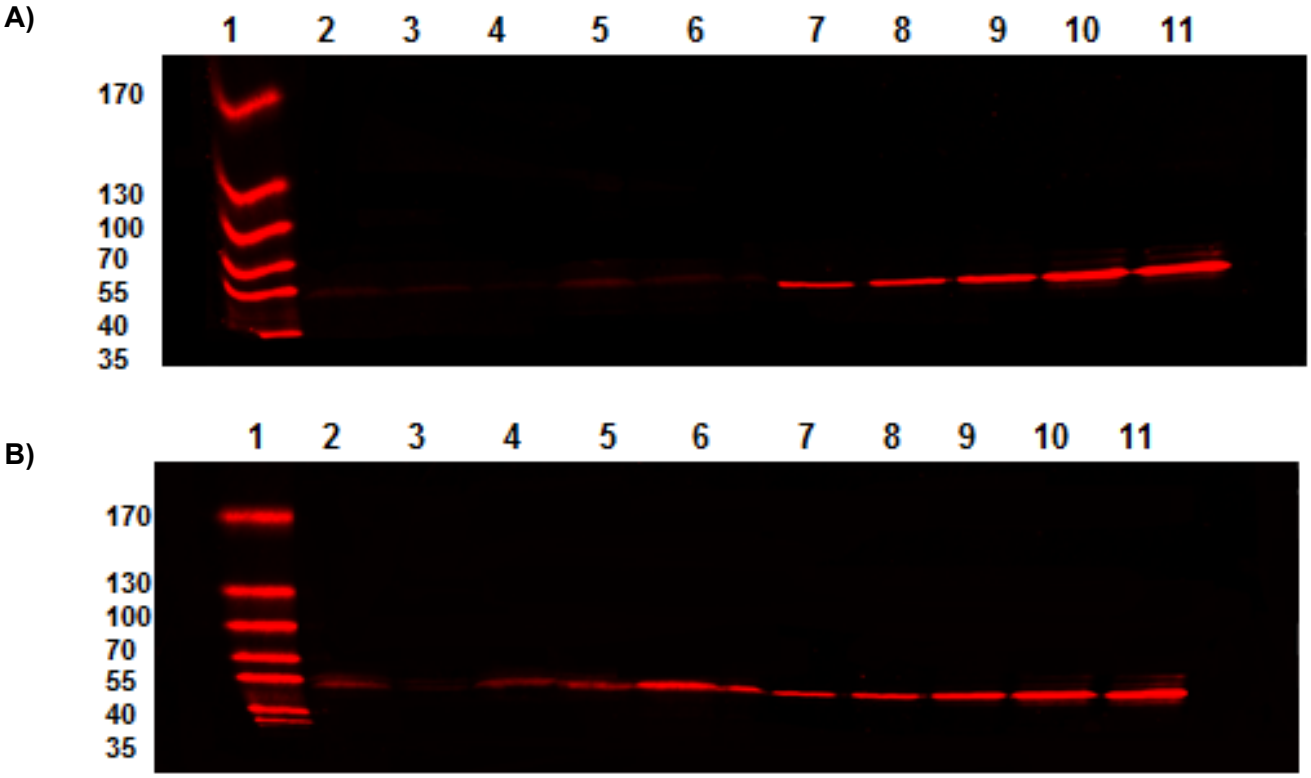

Figure 4-5. Western blot of human liver microsomes for CYP4V2 expression. Lane 1 contains the molecular weight marker, lanes 2 to 6 contain liver microsomes (20 ug microsomal protein), and lanes 7 to 11 contain purified CYP4V2 protein for quantification (0.0257 pmol, 0.1028 pmol, 0.4112 pmol, 0.257 pmol, 1.028 pmol). Livers with low CYP4V2 mRNA (Group 2) and high CYP4V2 mRNA (Group 1) are shown in Panels A and B, respectively.

The donors with the with the highest mRNA expression ranged in age from 21 to 59 years (5 males and 1 female), and those with the lowest mRNA expression ranged in age from nine to 53 years (3 males and 3 females). There were no noticeable trends in current medications, medical history, liver labs, and liver pathology between the two groups (Table 4-2).

Table 4-2. Donor demographics of liver samples with the lowest and highest CYP4V2 mRNA levels, listed in order of increasing CYP4V2 mRNA.

Group	Liver	Donor Age	Donor Sex	Medications	Medical History	Liver Labs	Liver Pathology	CYP4V2 mRNA
2	138	9 yr	F	dopamine, nipride, RBC, cefazolin	normal	abnormal	acute injury, split liver	607
2	161	53 yr	M	alcohol (1/2 bottle day), dopamine, insulin, clindamycin, cefuroxime	alcoholic, palsy symptoms, psoriasis, sleep apnea	normal	mild fatty	1016
2	120	45 yr	F	prozac, Li, sinequin, codeine, promethazine, dilantin (1 day), dopamine, insulin, gentamycin, mannitol, doxacurium, thyroxine	depression, prior hx of alcohol (> 10 yr ago)	normal	fatty	1135
2	113	9 yr	F	none	normal	normal	normal	1215
2	154	26 yr	M	marijuana, alcohol, dopamine, mannitol, insulin, dilantin (x2 days), phenobarb, clindamycin, zinacef, synthroid, cleocin, zantac	alcoholism, testicular carcinoma	abnormal	mild fatty	1324
2	114	19 yr	M	none	normal	normal	normal	1427
1	163	59 yr	M	unknown	unknown	unknown	fatty	3185
1	158	55 yr	M	nitroprusside, dopamine, insulin, clindamycin, cefuroxime	untreated hypertension	normal	mild fatty	3290
1	145	38 yr	M	cimetidine, diazepam, baclofen, dopamine, epinepherine,bretylium, atropine, succ, lidocaine, cefuroxime, clindamycin	quadriplegia (12 yr), multiple pneumonias	abnormal	fibrotic	3529
1	167	44 yr	M	unknown	unknown	unknown	normal (excellent)	3556
1	133	45 yr	F	dopamine, vasopressin, insulin, clindamycin, ceftriaxone, mannitol, dopamine	normal	normal	fatty	3788
1	102	21 yr	M	none	normal	normal	normal	4239

4.4.1 MicroRNA Microarray

A miRNA microarray analysis of the University of Washington, School of Pharmacy Human Liver Bank was conducted to identify miRNA candidates with potential to regulate CYP4V2. Tissues with known high and low expression of CYP4V2 mRNA were screened to identify potential regulatory miRNAs.

The differential microRNA expression for all 4,560 measured human probe sets on the Agilent microRNA microarray is shown in Figure 4-6. Group 1 (n=6) consists of human liver samples with the highest CYP4V2 mRNA expression, and Group 2 (n=6) consists of human liver samples with the lowest CYP4V2 mRNA expression as determined by the Illumina mRNA microarray data. Plotted on the x-axis is the signal intensity which indicates the relative miRNA expression, while the y-axis represents the fold-difference in expression between Groups 1 and 2. The miRNAs plotted above the top line are more highly expressed by 1.5-fold in Group 1, the samples with higher CYP4V2 mRNA levels. The miRNAs located below the bottom line are more highly expressed by 1.5-fold in Group 2, the livers with lower CYP4V2 mRNA levels. Highlighted in red are the four probes for miR-146b. Levels of both hsa-miR-146b-3p and hsa-miR-146b-5p were found to be statistically significantly higher in Group 2 (p-value < 0.05).

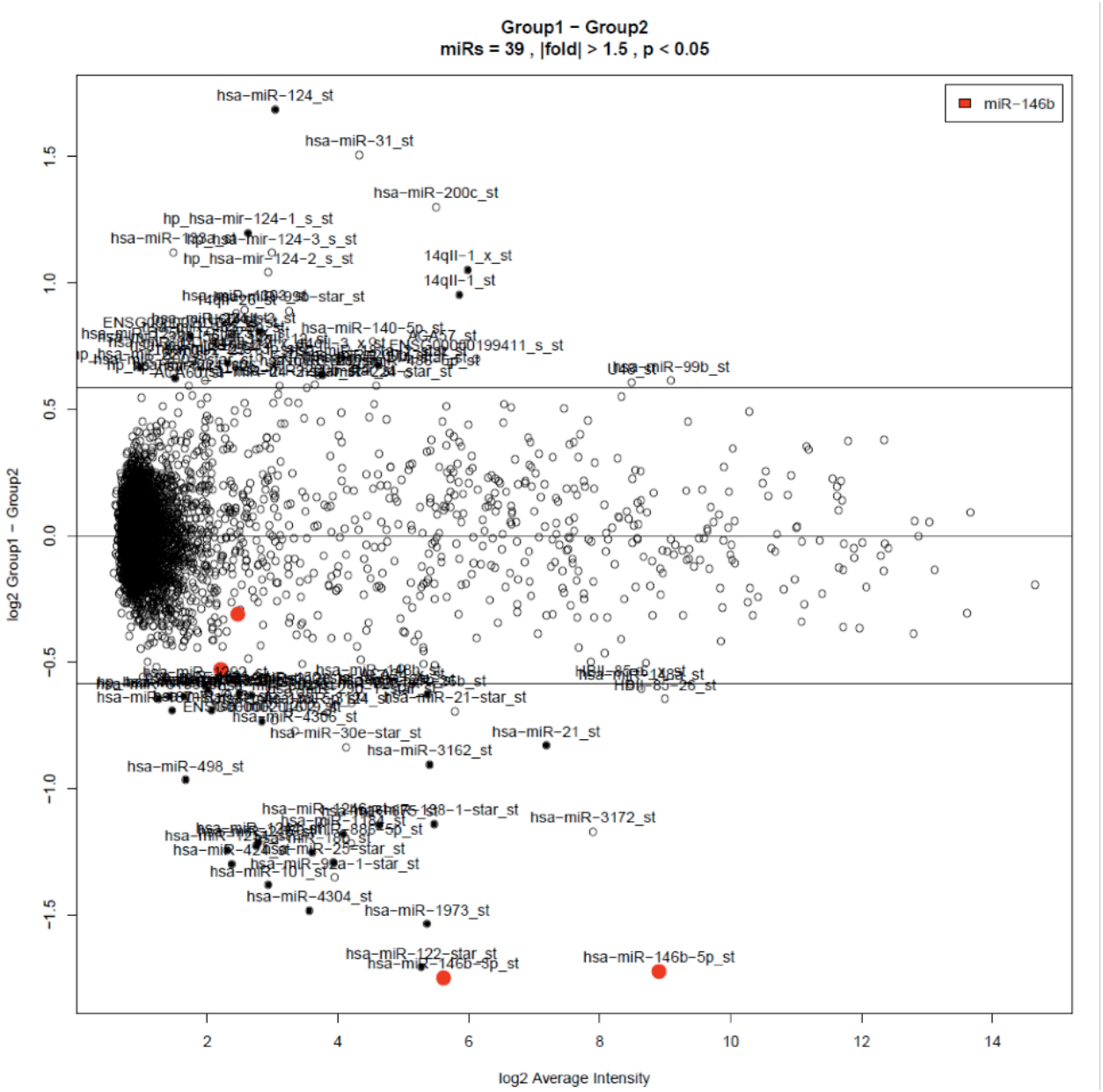

Figure 4-6. Microarray. miRNA gene expression analysis of UW liver bank samples comparing CYP4V2 mRNA high and low expressers. Members of the mir-146b family are indicated as red dots and a red star represents miR146b-5p as having the highest correlation.

An association was identified between increased levels of one miRNA (miR-146b-5p) and decreased steady-state levels of CYP4V2 mRNA (Figure 4-7). We examined the association of miR-146b-5p expression with CYP4V2 mRNA across the 55 human liver samples. The expression levels of miR-146b versus CYP4V2 mRNA, both expressed as the log2 absolute

normalized levels, show a distinct separation between Group 1 and Group 2 and a significant trend for decreased CYP4V2 expression with increased miR-146b levels.

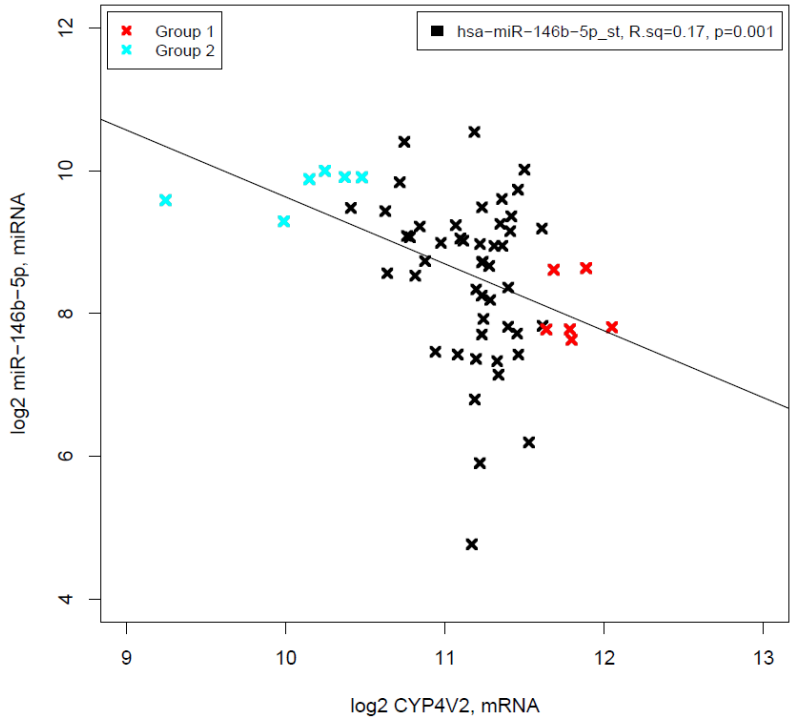

Figure 4-7. miR-146b-5p vs mRNA. Association of CYP4V2 expression and miR-146b-5p microRNA levels for 55 livers from the UW Human Liver Bank. The vertical axis displays the microRNA levels in the samples for miR-146b-5p, while the horizontal axis displays the mRNA expression for CYP4V2.

Consistent with the expected translational suppression of CYP4V2 mRNA by miRNA, Western Blot analysis verified CYP4V2 protein expression was positively correlated with CYP4V2 mRNA (R^2 = 0.472; p = 0.0282), and negatively correlated with miR-146b-5p (R^2 = 0.4254; p = 0.041) (Figure 4-8). It is not yet clear whether or not this regulation is due to direct binding to a complementary 3'-UTR region in CYP4V2 mRNA or a secondary effect. There is a potential miR-146b-5p binding site in the CYP4V2 3'-UTR at nucleotide 2115 suggesting microRNA may play a role in down-regulation of protein expression, which will be explored further in this study.

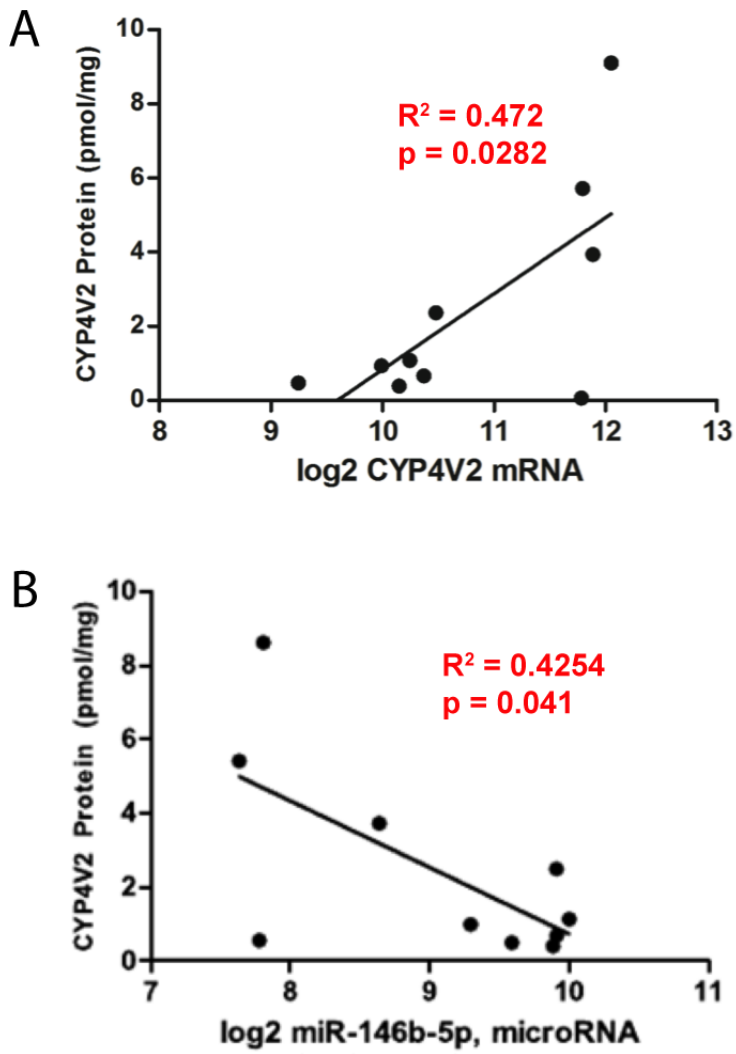

Figure 4-8. CYP4V2 protein vs mRNA and miR-146b-5p A) Association between CYP4V2 protein levels and mRNA levels. B) Association between CYP4V2 protein levels and miR-146b-5p expression.

4.4.2 In vitro Methods for Evaluating miR-146b-5p Regulation

4.4.2.1 HepG2 Transfection and Luciferase Activity

HepG2 cells were chosen initially because we showed they express endogenous miR-146b, albeit at lower levels than in human liver tissue (Figure 4-9). To validate the HepG2 perpetual cell line as an appropriate model to evaluate expression and suppression of gene regulation in hepatocytes, we analyzed the expression of miR-146b in HepG2 cells in

comparison with RNA isolated from samples from the University of Washington human liver tissue samples from the University of Washington School of Pharmacy liver bank. Expression was quantified by quantitative real time polymerase chain reaction (qRT-PCR; Applied Biosystems 7900HT RealTime PCR, Waltham, MA) using the ΔΔ Ct method, normalized to HepG2 cells with 18s as a housekeeping gene. Analysis showed miR-146b is expressed at levels less than one order of magnitude lower than human liver samples, but is still robustly expressed, suggesting HepG2 cells will be a viable *in vitro* model system for detecting expression changes with luciferase constructs.

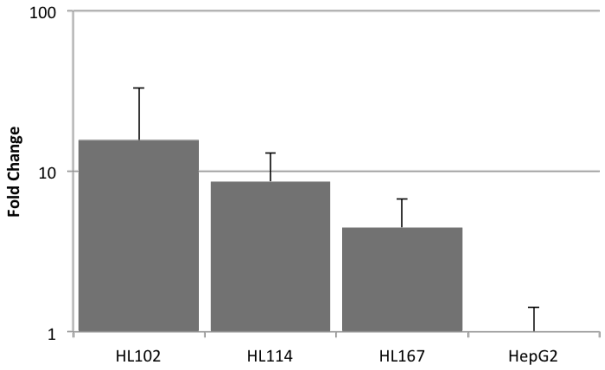

Figure 4-9. Relative expression of miR-146b in human liver tissue (HL102, HL114, HL167) and HepG2 cells. HepG2 cells express endogenous miR-146b, but at a lower level than in liver tissue.

As a carcinoma cell line they are immortal and readily cultured. There was no significant difference in luciferase activity between clones containing the CYP4V2 3'UTR and the scrambled control. Two clones from each cell line, transfected with the CYP4V2 target clone or scrambled negative control, were stably transfected with a miR-146b expression clone to over-express the miRNA or a non-targeting control miRNA. Figure 4-10 shows the transfection efficiency observed at Day 2, and at stable transfection.

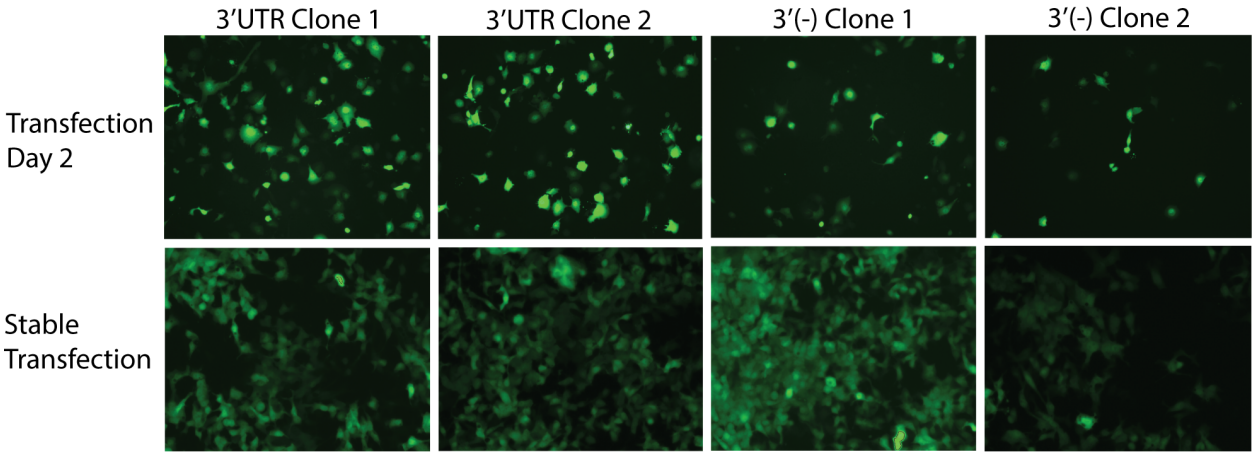

Figure 4-10. HepG2 transfection efficiency. A) Fluorescence after transfection with GFP(+) plasmids. The top row shows transfection efficiency on Day 2. The bottom row shows successful stable transfection after approximately two weeks.

Mean luciferase activity was normalized to secreted alkaline phosphatase (SEAP) levels. As expected, in clones that had been stably transfected with the complete CYP4V2 3'-UTR, overexpression of miR-146b led to lower luciferase activity compared to clones that were transfected with the scrambled 3'-UTR control vector (Figure 4-11, Panel A). This suggests greater suppression in cells that overexpress the miR-146b target sequence than those containing only endogenous genetic targets. Similarly, in clones that were transfected with the scrambled 3'-UTR control vector, thus only exhibiting endogenous target sequence, those that were subsequently transfected to overexpress miR-146b showed lower mean luciferase activity than those transfected with a non-targeting miRNA control (Figure 4-11, Panel B). This suggests that overexpression of miR-146b decreases endogenous CYP4V2 expression. Luciferase signal intensity showed trends similar to expectations; however, while the trends suggested a potential regulatory interaction, the data were extremely variable so no firm conclusions regarding the mechanism of interaction can be drawn from this experiment.

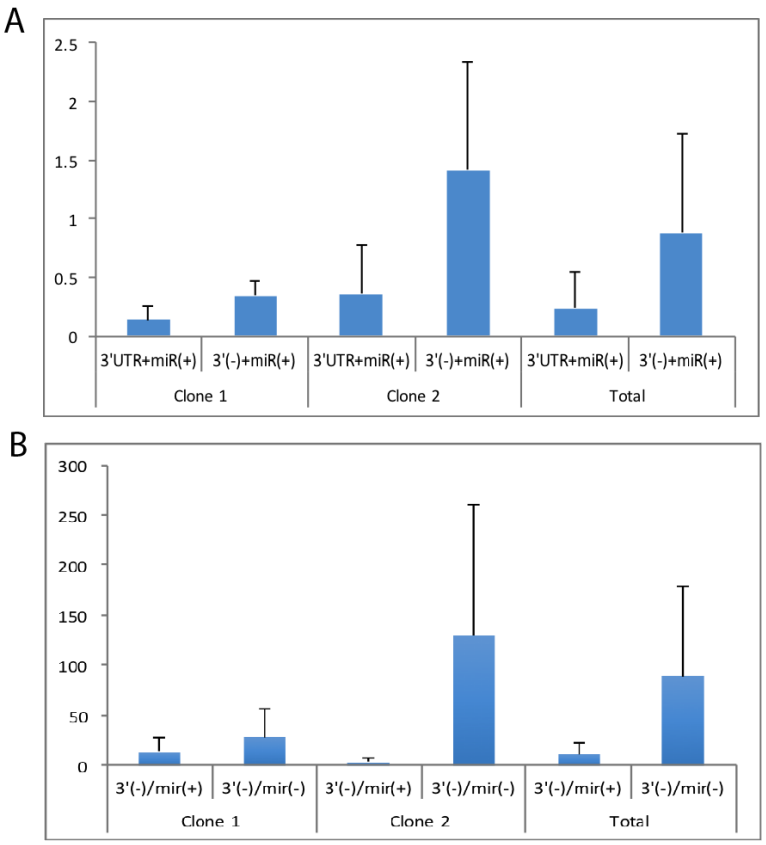

Figure 4-11. HepG2 luciferase activity. Mean, normalized luciferase activity measured in HepG2 cells that were stably transfected with clones containing the full CYP4V2 3'-UTR (3'UTR), or a scrambled 3'-UTR control (3'(-)). Cells were subsequently stably transfected to either overexpress miR-146b (miR(+)), or a non-targeted miRNA control (miR(-)).

4.4.2.2 ARPE-19 Transfection and Assay

ARPE-19 cells were transiently transfected with plasmids to either overexpress miR-146b, or plasmids containing a non-targeting miRNA control. Plasmids included a green fluorescent marker so transfection could be visually confirmed. Transfection efficiency was only approximately 10% - 20%, as shown by the green fluorescent marker, but it was sufficient for qualitatively assessing changes in CYP4V2 protein expression in transfected cells (Figure 4-12 and Figure 4-13).

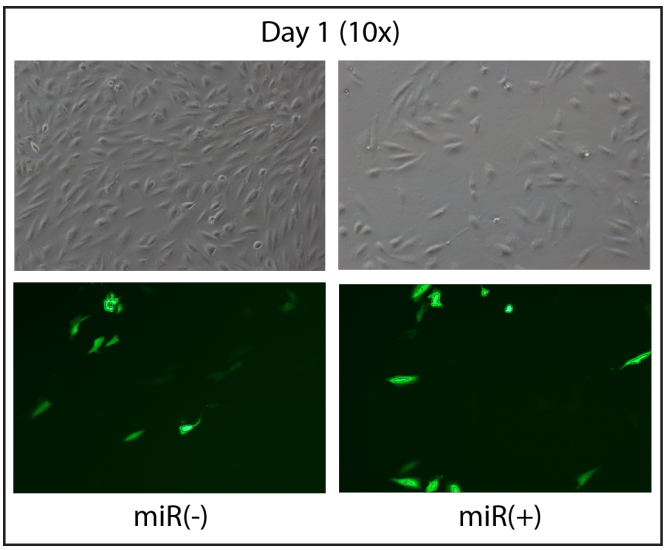

Figure 4-12. ARPE-19 transfection efficiency. Transfection efficiency after 24 hours under transfection conditions in the cells used for protein quantitation. The two images on the left are the brightfield and fluorescent images of the well containing cells transfected with the non-targeting miRNA control, and the two images on the right are the brightfield and fluorescent images of the well containing cells transfected to overexpress miR-146b. Images are at 10x magnification.

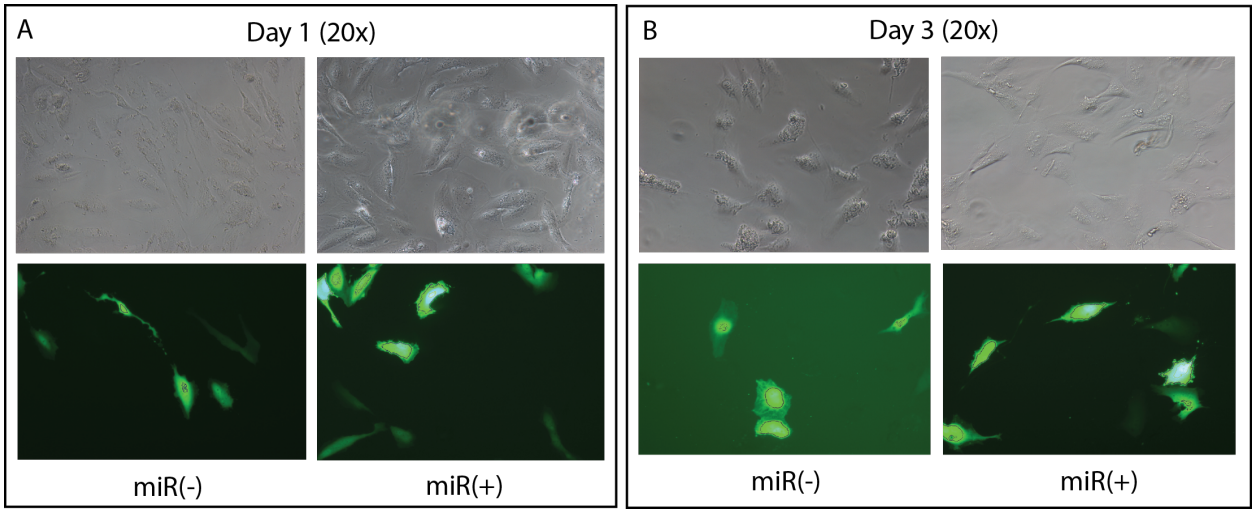

Figure 4-13. ARPE-19 transfection efficiency. Transfection efficiency after 24 hours under transfection conditions in the cells used for qualitative analysis. A) Immediately after transfection (Day 1), the two images on the left of Panel A are the brightfield and fluorescent images of the well containing cells transfected with the non-targeting miRNA control, and the two images on the right are the brightfield and fluorescent images of the well containing cells transfected to overexpress miR-146b. B) Day 3 after transfection before fixing. The two images on the left of Panel B are the brightfield and fluorescent images of the well containing cells transfected with the non-targeting miRNA control, and the two images on the right are the brightfield and fluorescent images of the well containing cells transfected to overexpress miR-146b. Images are at 20x magnification.

After immunocytochemistry preparation, cells were qualitatively analyzed for changes in CYP4V2 protein expression. The secondary to rabbit IgG was labeled with red fluorophore, which bound to the CYP4V2 primary antibody. Dual staining was conducted with a primary mouse monoclonal antibody to GFP to detect transfected cells. A secondary antibody to mouse IgG labeled with a green fluorphore bound to the GFP primary antibody. This dual staining was necessitated by the use of methanol fixation conditions, which gave optimal detection of CYP4V2 in ARPE-19 cells, but also resulted in denaturation and loss of endogenous GFP fluorescence.

Signal intensity is a measure of protein expression, and cells that did not undergo transfection had a signal of noticeably higher intensity than those that were transfected to overexpress miR-146b-5p (Figure 4-14). This suggests the regulatory influence of miR-146b-5p may be due to a direct interaction to repress protein expression.

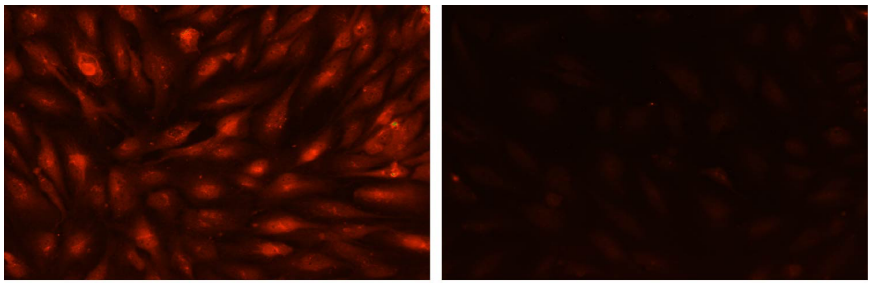

Figure 4-14. Results of ARPE-19 transfection. CYP4V2 protein expression was qualitatively compared in cells with no transfection to those that were transfected to overexpress miR-146b-5p.

I was unable to compare GFP fluorescence to CYP4V2 signal intensity in this experiment due to the loss of GFP fluorescence from the methanol fixation process. The experiment was repeated, and after methanol fixation, a primary antibody to GFP was added to the incubation to restore the signal. While the GFP signal was successfully restored, the CYP4V2 signal was

substantially weaker than shown above (Figure 4-14), so quantitation was potentially less reliable than if the signal were high as before. When comparing the average corrected total cell fluorescence, I found no clear difference in CYP4V2 expression in cells that were transfected to overexpress miR-146b-5p compared to those transfected with a non-targeting control miRNA (Figure 4-15). This may be due to sufficiently high endogenous expression of miR-146b-5p such that the difference in CYP4V2 expression was not adequately suppressed by our overexpression vector, or it may suggest a secondary mechanism of regulation.

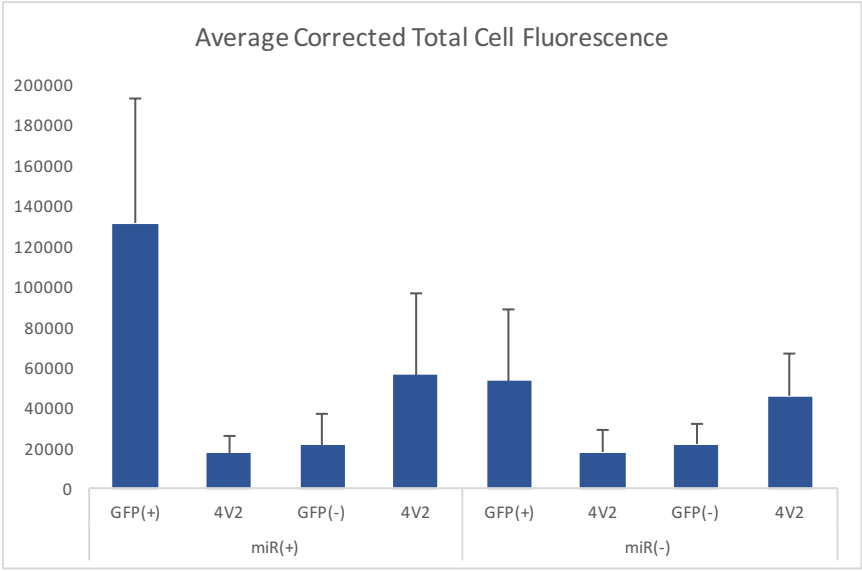

Figure 4-15. Average corrected total cell fluorescence for CYP4V2 in cells transfected (GFP(+)) or non-transfected (GFP(-)) with a vector to overexpress miR-146b-5p (miR(+)) or a non-targeting control vector (miR(-)).

However, when comparing the ratio of CYP4V2 signal normalized to GFP signal, there was a statistically significant difference in relative expression of CYP4V2 between cells transfected to overexpress miR-146b-5p to those transfected with a non-targeting control vector ($p = 0.00397$; Figure 4-16). For a direct regulatory interaction, we would expect the expression of CYP4V2 to be lower in cells transfected to overexpress miR-146b-5p, as shown in Figure 4-

16. There was no difference when comparing non-transfected cells in wells exposed to miR-146b-5p overexpression vector to non-transfected cells in well exposed to the non-targeting control (p = 0.148; Figure 4-16). This supports the possibility that miR-146b-5p may have a direct regulatory interaction with CYP4V2.

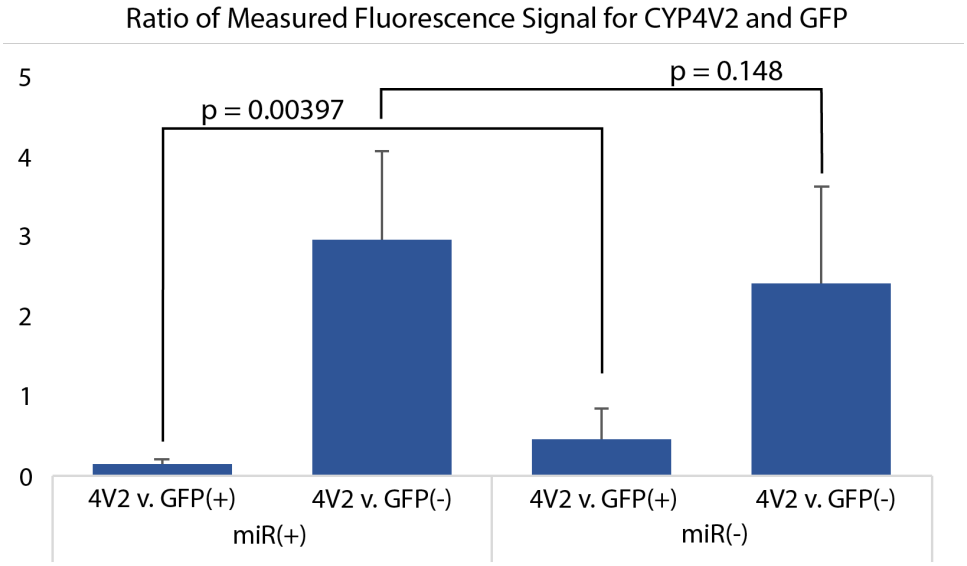

Figure 4-16. Ratio of measured fluorescence signal for CYP4V2 expression to GFP signal in cells transfected (GFP(+)) or non-transfected (GFP(-)) with a vector to overexpress miR-146b-5p (miR(+)) or a non-targeting control (miR(-)).

4.4.2.3 ARPE-19 Protein Quantitation

Two unique signature peptides (SVSEDCEVAGYR and TILSCILR) were selected for LC-MS/MS quantification of CYP4V2. Chromatograms from targeted LC-MS/MS analysis confirmed CYP4V2 protein expression in the samples of ARPE-19 cells with both signature peptides (Figure 4-17). The peak signal reflects protein expression, and the multiple peaks represent the fragment ions of the CYP4V2 surrogate peptides.

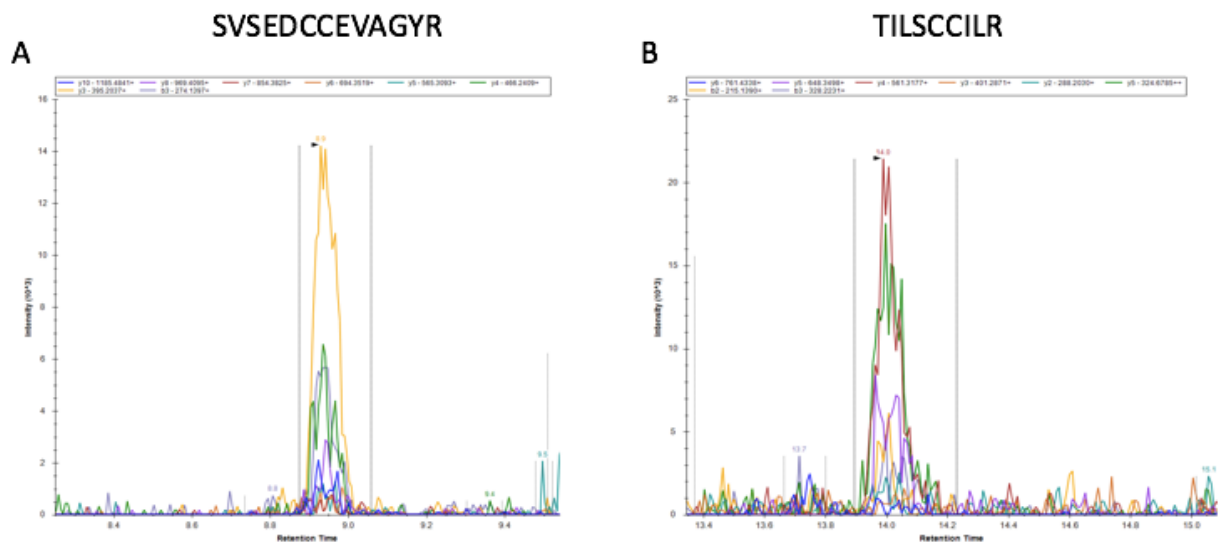

Figure 4-17. Chromatograms from targeted LC/MS-MS analysis. The peaks show expression of CYP4V2 protein from each of two unique signature peptides for representative ARPE-19 samples. A) Peptide SVSEDCCEVAGYR, B) Peptide TILSCCILR.

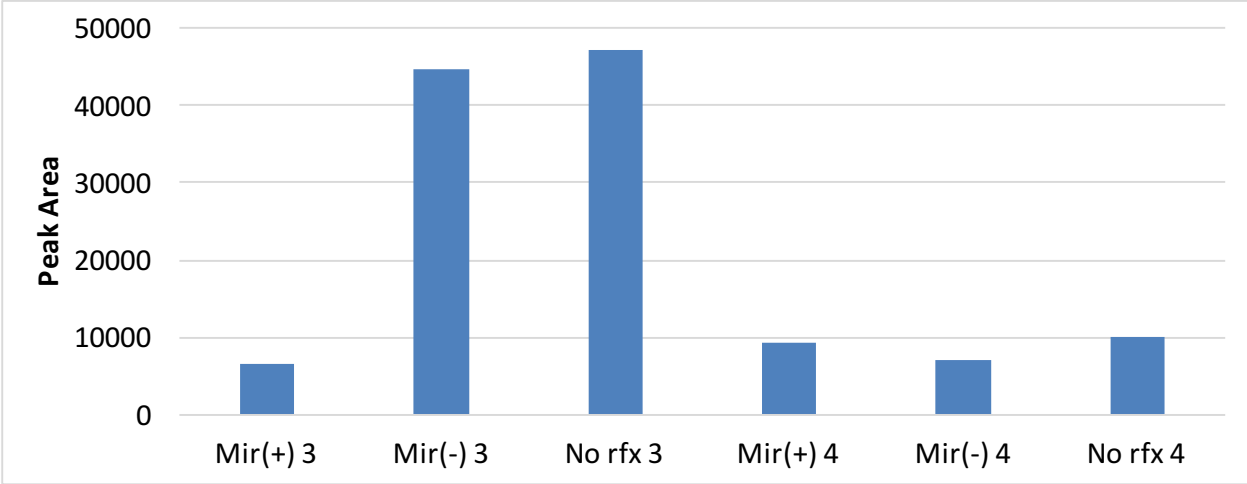

Figure 4-18. Average peak area of CYP4V2 surrogate peptides. Peak area reflects protein CYP4V2 expression. Mir(+) = miR-146b-5p overexpression, Mir(-) = non-targeting control, No rfx = non-transfected.

The average peak area of multiple unique fragments for each sample was calculated for each transfection condition (Figure 4-18). For the first set of samples (Transfection 3), protein expression was lowest in the cells that were transfected to overexpress miR-146b-5p (Mir(+) 3),

compared to cells transfected with a non-targeting scrambled control (Mir(-) 3) or non-transfected cells (No rfx 3). For the second set of samples (Transfection 4), there was no clear difference in protein expression between all three culture conditions (Figure 4-18; Mir(+) 4, Mir(-) 4, No rfx 4).

4.5 Discussion

The function and regulation of CYP4V2 in normal human physiology is not well understood. Here we describe a potential regulatory mechanism that influences expression of CYP4V2 *in vivo* through interaction with miR-146b-5p. Using liver tissue samples, we identified candidate miRNAs that had potential for regulatory interactions with the 3'UTR of CYP4V2, and showed that protein expression was positively associated with expression of mRNA, and negatively associated with miR-146b-5p, suggesting a repressive effect of the miRNA on CYP4V2. This interaction was further validated *in vitro* in ARPE-19 cells in which a qualitative analysis of fluorescence signal intensity suggested expression of CYP4V2 protein was decreased in cells transfected to overexpress miR146b-5p. Finally, absolute protein quantitation was evaluated using LC/MS-MS. The first set of samples showed reduced protein expression in the presence of overexpressed miR-146b-5p, as expected for a regulatory interaction. The second set of samples shown no clear difference in protein, and the overall expression was very low across all three culture conditions. According to qualitative assessment, transfection efficiency was similar between both sets of samples (Transfection 3 and 4), but it is possible the overall number of cells analyzed was different between the sets, or the overexpression of miR-146b-5p was insufficient to overcome the already low protein expression observed in the second set of samples. This experiment must be repeated to confirm our findings. The data presented here

provides evidence that miR-146b-5p does exert a regulatory effect on CYP4V2, and it appears to be a direct interaction.

Previous studies in our lab have shown that CYP4V2 is an ω–hydroxylase with substrate specificity for medium-chain fatty acids.[9,89] This work adds to our understanding of CYP4V2 in normal physiology, and may contribute to the identification of potential pathogenic process mediated by non-functional or poorly functioning CYP4V2.

Alterations in CYP4V2 expression may impact the viability of RPE cells. Retinal photoreceptor outer segments have the highest DHA content of any cell in vertebrates. Given that mammals have limited capacity to synthesize DHA, a key function of RPE cells is DHA uptake, recycling, and delivery to rod inner segments.[184] While DHA is a critical structural component of disk outer membrane phospholipid bilayers, it is also an important signaling molecule. That is, DHA serves as a precursor to cytoprotective docosanoids, including the protectins and resolvins.[185,186] Resolvin D1 (RvD1) and protectin D1 (PD1)/Neuroprotectin D1 (NPD1) are oxygenated metabolites of DHA that possess anti-inflammatory and immuno-regulatory properties.[93] Formation of both docosanoids PD1 and RVD1 goes through a common lipoxygenase-generated intermediate, 17S-hydroperoxy-DHA. Resolvin D1 is the result of reduction of the hydroperoxide, subsequent 5-lipoxygenase (5-LO) action to form the 7,8-epoxide, followed by hydrolysis.[187] Protectin D1/Neuroprotectin D1 are formed by hydrolysis of the 16,17-epoxide derived directly from 17S-hydroperoxy-DHA. These pathways are similar to leukotriene B4 formation from arachidonic acid. It is well established that inactivation of leukotriene B4 relies on initial ω-hydroxylation by CYP4F3A, a leukocyte-specific, splice variant of the CYP4F3 gene, followed by β-oxidation.[95] Therefore, analogous pathways could be

involved in the inactivation of the resolvins and protectins, and even DHA itself. In ARPE-19 cells, a human RPE cell line, the only CYP4 isozyme present is CYP4V2 (unpublished).

Interestingly, RvD1 was found to cause up-regulation of multiple miRNAs involved in the resolution of acute inflammation, including miR-146b.[188] This particular miRNA has been found to regulate a number of cytokines and signaling proteins involved in immune response, particularly the inhibition of NFκB signaling through the down-regulation of interleukin-1 receptor-associated kinase-1 and TNF receptor-associated factor 6 proteins, two key adapter molecules involved in the IRAK/ NFκB pathway causing inflammation.[189] Increased levels of miR-146b-5p were seen after 8 hr treatment with 100 ng/mL lipopolysaccharide (LPS) in transfected myeloid cell lines THP-1, U937, HL-60, and WEHI-3.[189] However, the opposite trend was seen *in vivo*. Schmidt et al. administered a 4-hour infusion of 2 ng/kg LPS to healthy volunteers and observed a decrease in miR-146b-5p in polymorphonuclear leukocytes.[190] This discrepancy with miR-146b-5p levels can be potentially explained by a couple reasons. First, measurement of miR-146b-5p was conducted in different cell types in the two studies, and it is possible that response to LPS administration may be different in leukocytes compared to monocytes, as proposed by Schmidt et al. But a more likely reason may be the disparity in dose between the *in vitro* studies and human studies. Using a 3 L blood volume, a dose of 2 ng/kg would yield concentrations >20,000-fold lower *in vivo* compared to the *in vitro* studies. This suggests that upon exposure to low doses of LPS, miR-146b-5p levels would decrease to facilitate the acute inflammatory response cascade. At higher doses of LPS, or continued exposure and inflammation, miR-146b-5p levels are increased to begin the resolution phase, thus preventing chronic inflammation. This hypothesis is supported by studies exploring the protective role of miR-146b-5p against inflammation.

Chronic, low-grade inflammation is associated with a number of disease states, including obesity, with studies showing that dysregulation of miRNA expression can be linked to this condition.[191] Globular adiponectin, a known anti-diabetic adipokine solely expressed in monocytes/macrophages, possesses anti-inflammatory properties by causing induction of interleukin-1 receptor-associated kinase-3, a key inhibitor of the IRAK/ NFκB pathway.[192] Globular adiponectin is associated with obesity-related inflammation and has been found to be present in lower levels in obese patients.[192] In addition, Hulsmans et al. observed decreased expression of miR146b-5p in circulating monocytes of obese patients and proposed that miR-146b-5p is a significant contributor to the anti-inflammatory action of globular adiponectin.[193]

Additional studies have demonstrated the importance of miR-146b-5p in inflammation. For example, Takahashi et al. conducted microRNA expression profiling in cord blood cells to elucidate the molecular mechanisms underlying the decreased immune function in cord blood cells compared to adult peripheral blood. They observed differential expression of miR-146b-5p in cord blood cells versus adult peripheral blood cells, including decreased miR-146b-5p expression in CD14+ cord blood cells in response to treatment with the pro-inflammatory cytokine, interferon (IFN)-γ.[194] In addition, miR-146b decreased protein expression of the pro-inflammatory interleukin-8 (IL8) and Chemokine (C-C motif) ligand 5 (CCL5), potent chemoattractants driving leukocytes into sites of inflammation.[195]

Deregulation of miRNAs, including miR-146b-5p, has also been implicated in many types of cancers. *In vitro* studies have shown that overexpression of miR-146b-5p causes a decrease in cell migration and invasion in various cancer cell types and matrix metalloproteinase *MMP16* and epidermal growth factor receptor *EGFR* genes were identified as targets of miR-146b-5p.[196-199] In contrast, miR-146b-5p did not have a significant effect on the cellular

proliferation, migration, or invasiveness of A549 lung cancer cells, despite being highly expressed in recurrent disease following surgical removal of non-small cell lung cancer tumors.[200,201] Research by Garcia et al. suggest an increased expression of miR-146b-5p *in vitro* in basal-like mammary cancer cell lines and *in vivo* in triple negative breast tumor tissues, and this overexpression is associated with down-regulation of the *BRCA1* gene.[202] Pallante et al. also observed higher levels of miR-146b-5p in papillary thyroid carcinoma cells[203] This was followed by Geraldo et al. uncovered the potential oncogenic role of miR-146b-5p as a negative regulator of the transforming growth factor β pathway, via repression of the SMAD4 gene (SMAD family member 4) in thyroid cancer.[203,204]

The inflammatory response is important for protection and host defense but is a process that must be tightly regulated. Uncontrolled inflammation leads to a number of diseases: classic ones, such as psoriasis, periodontal disease and arthritis, as well as obesity and cancer.[205] Thus, resolution of inflammation is important to maintain homeostasis.[206] Resolvins are key players in this resolution phase, exerting anti-inflammatory and immunoregulatory effects by decreasing neutrophil infiltration, regulating cytokines and reactive oxygen species.[207] These properties of resolvins are consistent with the anti-inflammatory effects of miR-146b-5p. Thus, RvD1 increases miR-146b expression, which would allow miR-146b to target genes involved in the immune system and control inflammation and resolution.

In our work, miR-146b-5p was associated with both CYP4V2 mRNA and protein levels. Thus, increased expression of miR-146b-5p may result in a down-regulation of CYP4V2 expression. These data provide preliminary evidence that epigenetic regulation of CYP4V2 by miRNA may explain the inter-individual variability in the human liver tissue bank. Whether miR-146b-5p is exerting its effects directly on CYP4V2 via the putative binding site in the 3'-

UTR must still be elucidated. Such experiments could include, but are not limited to: 1. targeted over-expression of miR-146b-5p or siRNA directed towards miR-146b-5p via transfection into primary human hepatocytes; and 2. use of Luciferase reporter vectors containing the wild-type CYP4V2 3'-UTR compared to mutated miR-146b-5p target sequence in appropriate cell lines (e.g. primary hepatocytes or ARPE-19 cells).

The negative association between miR-146b-5p and CYP4V2 raises the question of what role CYP4V2 may have in docosanoid signaling pathways. It is plausible that this signaling circuit acts to decrease CYP4V2 mRNA and protein and attenuate ω-hydroxylation-mediated inactivation of RvD1 during the resolution phase of the inflammatory response (Figure 19). Investigating potential CYP4V2-catalyzed metabolism of RvD1 may help elucidate the role of CYP4V2 in the acute inflammatory process and provide more insight into the mechanistic causes of BCD.

Chapter 5

Future Directions – Gene Replacement Therapy for Ocular Disease

5.1 Introduction

To date, nearly 90 different eye diseases have been identified that are caused by genetic mutations or chromosomal abnormalities (Table 5-1).[208] Additionally, there are well over 150 other genetically-mediated disorders that include an ocular component in the pathology. In most cases, these diseases are classified as rare, meaning they affect fewer than 200,000 individuals in the United States.[209] These diseases are challenging from a therapeutic standpoint due in part to the pathological complexity of genetic disease, and, for ocular diseases, the challenge of delivering therapeutic agents to a physiologically isolated organ system.

Since the eye is so well protected, treatment options and routes of administration are limited by minimal transfer between ocular spaces and systemic circulation. This is due in part to a robust blood-retinal barrier (BRB) that functions similarly to the blood-brain barrier in protecting vulnerable ocular tissues from both endogenous and xenobiotic compounds circulating systemically. The BRB is described in Chapter 1 (Figure 1-5), with the inner BRB formed by tight junctions and transporters located on retinal capillaries, and the outer BRB formed by the RPE cells at the base of the retina.[46]

Table 5-1. Ocular diseases and disorders that are known to be associated with genetic mutations.

DISORDER	KNOWN GENES OR CHROMOSOMAL ABNORMALITY INVOLVED	MODE OF INHERITANCE	EYE FINDING
Achromatopsia	CNGA3, CNGB3	AR	Photophobia, day blindness, nystagmus, colorblindness, myopia
Aniridia	PAX6, ELP4	AD, or trauma	Cataract, glaucoma, Peter's anomaly, corneal clouding
Anterior Segment Mesenchymal Dysgenesis	FOXE3, PITX3	AD	Cataract, corneal opacity, dysgenesis of ocular anterior segment
Avellino Corneal Dystrophy (Combined Granular-Lattice Corneal Dystrophy)	TGFBI	AD	Hyaline changes in anterior stroma, fusiform amyloid deposits in deeper stroma
Axenfeld-Rieger Syndrome	PITX2, FOXC1	AD	Prominent Schwalbe line, iris dysplasia, iris strands, corectopia, polycoria, glaucoma, strabismus, hypertelorism, telecanthus

DISORDER	KNOWN GENES OR CHROMOSOMAL ABNORMALITY INVOLVED	MODE OF INHERITANCE	EYE FINDING
Best Macular Dystrophy	BEST1	AD	Yellow pigmented macular lesion, cystoid macular degeneration
Bietti Crystalline Corneoretinal Dystrophy	CYP4V2	AR	Retinal degeneration, choroidal vessel sclerosis, crystalline corneal deposits, marginal corneal dystrophy, night blindness
Blepharophimosis, Ptosis, and Epicanthus Inversus (BPES)	FOXL2	AD (50% de novo)	Blepharophimosis, ptosis, epicanthus inversus, telecanthus, microphthalmia, microcornea, strabismus, hypermetropia, nystagmus, pronounced convex arched eyebrows
Blue-Cone Monochromacy	OPN1LW, OPN1MW	XLR	Blue cone type colorblindness, photophobia, nystagmus, myopia, macular pigment epithelial changes
Choroideremia	CHM	XLD	Choroidoretinal degeneration, night blindness, visual field constriction
Colorblindness, Deutan	OPN1MW	X-linked	Green colorblindness
Colorblindness, Protan	OPN1LW	X-linked	Red colorblindness
Colorblindness, Tritanopic	OPN1SW	AD	Abnormal blue and yellow vision
Cone-Rod Dystrophy	Numerous	AD, AR, X-linked	Dyschromatopsia, photophobia, nystagmus, maculopathy, progression to night blindness later
Congential Fibrosis Of Extraocular Muscles	KIF21A, PHOX2A, ARIX, TUBB3	AD, AR	Ptosis, ophthalmoplegia
Congenital Nystagmus	Numerous	AD, AR, X-linked	Pendular and horizontal nystagmus, head turn, strabismus
Congenital Stationary Night Blindness	Numerous	AD, AR, X-linked	Night blindness, myopia
Cornea Plana	KERA	AR	Hyperopia, hazy corneal limbus, corneal opacities, thin cornea
Costeff Syndrome	OPA3	AR	Optic atrophy
Doyne Honeycomb Dystrophy (Malattia Leventinese)	EFEMP1	AD	Retinal degeneration
Duane-Radial Ray Syndrome	SALL4	AD	Strabismus, Duane anomaly, globe retraction and palpebral fissure narrowing on adduction, optic disc hypoplasia, iris coloboma, retinal coloboma, epicanthal folds, hypertelorism, cataracts, microphthalmia
Ectopia Lentis Et Pupillae	ADAMTSL4	AR	Ectopic lens and pupil, cataract, myopia, abnormal appearing iris, increased corneal diameter, retinal detachment
Ectopia Lentis, Familial	FBN1	AD	Congenital lens dislocation
Ectopia Lentis, Isolated	ADAMTSL4	AR	Lens dislocation
Enhanced S-Cone Syndrome	NR2E3	AR	Vitreoretinal degeneration, retinoschisis, hemeralopia, macular edema, cataract, night blindness

DISORDER	KNOWN GENES OR CHROMOSOMAL ABNORMALITY INVOLVED	MODE OF INHERITANCE	EYE FINDING
Epithelia Basement Membrane Corneal Dystrophy (Map-Dot-Fingerprint Corneal Dystrophy)	TGFBI	AD	Map lines-dots-fingerprint lines epithelial corneal changes, recurrent corneal erosions
Fish-Eye Disease	LCAT	AR	Corneal opacities
Fuch's Endothelial Corneal Dystrophy	Numerous	AD	Corneal endothelial guttata, stromal edema, endothelial cell death, hypertrophy and polymorphism
Glaucoma, Congenital	CYP1B1, MYOC	AR	Buphthalmos, increased intraocular pressure, corneal haze, myopia
Glaucoma, Open Angle Juvenile Onset	MYOC, CYP1B1	AD	Increased intraocular pressure, myopia
Glaucoma, Open Angle Adult Onset	OPTN, ASB10, WDR36	AD	Increased intraocular pressure, myopia
Granular Corneal Dystrophy (Groenouw Type I)	TGFBI	AD	Opacities in stromal layer
Gyrate Atrophy	OAT	AR	Progressive chorioretinal degeneration, night blindness, myopia, cataracts
Jalili Syndrome	CNNM4	AR	Cone-rod dystrophy, nystagmus, photophobia, bull's eye macular lesion, progressive central vision loss, night blindness, optic pale disc
Kearns-Sayre Syndrome	Multiple	Mitochondrial	Ptosis, progressive external ophthalmoplegia, pigmentary retinopathy
Lattice Corneal Dystrophy	TGFBI	AD	Lattice pattern of amyloid deposits in stromal layer, recurrent corneal erosions
Leber Congenital Amaurosis	Numerous	AD, AR	Pigmentary retinopathy, photophobia, cataract, nystagmus, eye poking, diminished electroretinogram
Leber Hereditary Optic Neuropathy	MTND1, MTND4, MTND5, MTND6	Mitochondrial	Progressive blurred vision, optic atrophy, vascular tortuosity of central retinal vessels, circumpapillary telangiectatic macroangiopathy, retinal nerve fibers swelling
Macular Degeneration, Age-Related	Numerous	-	Degeneration of macula that affects central vision
Macular Corneal Dystrophy (Groenouw Type Ii)	CHST6	AR	Gray-white punctate opacities in stromal layer that extent to peripheral cornea with lack of clear spaces between opacities
Marcus Gunn Phenomenon	-	?AD	Unilateral congenital ptosis, elevation of ptotic lid upon movement of lower jaw
Meesmann Corneal Dystophy	KRT3, KRT12	AD	Punctate opacities in corneal epithelium, photophobia, astigmatism
Neuropathy, Ataxia, And Retinitis Pigmentosa (Narp)	MT-ATP6	Mitochondrial	Retinopathy, nystagmus, sluggish pupils
Normal-Tension Glaucoma		-	Glaucoma with no elevated intraocular pressure

DISORDER	KNOWN GENES OR CHROMOSOMAL ABNORMALITY INVOLVED	MODE OF INHERITANCE	EYE FINDING
Norrie Disease	NDP	XLR	Retinal detachment, microphthalmia, retinal dysplasia, corneal and vitreous opacities, cataract, optic atrophy
Occult Macular Dystophy	RP1L1	AD	Progressive decreased vision, reduced focal macular electroretinogram
Ocular Albinism	GPR143	X-linked	Nystagmus, decreased iris pigment, translucent iris, foveal hypoplasia, strabismus, translucent iris, nystagmus, photophobia, high refractive erros
Oculocutaneous Albinism	TYR, OCA2, TYRP1, or SLC45A2, MC1R	AR	Nystagmus, decreased iris pigment, translucent iris, foveal hypoplasia, strabismus, white hair and skin, translucent iris, nystagmus, photophobia, high refractive erros
Oguchi Disease	SAG, GRK1	AR	Congenital stationary night blindness, golden yellow fundus in light that disappears in dark adaptation (Mizuo-Nakamura phenomenon)
Optic Atrophy	Numerous	AD, AR, X-linked	Optic nerve pallor, cataract
Peters' Anomaly	PAX6, PITX2, CYP1B1, FOXC1	AD, AR	Central corneal leukoma, absent Descemet membrand and posterior stroma, iris and lens attachments to posterior cornea
Peters-Plus Syndrome (Krause-Kivlin Syndrome)	B3GALTL	AR	Peter's anomaly, nystagmus, glaucoma, cataract, myopia, coloboma, upslanting palpebral fissures, ptosis, hypertelorism
Pigment Dispersion Syndrome	-	AD	Glaucoma, myopia, pigment granules on corneal endothelium, iris transillumination defects, concave iris, increased pigmentation of trabecular meshwork, deposited pigment on Schwalbe's line
Pseudoexfoliation Syndrome	LOXL1	AD	Glaucoma, white flaky deposits on anterior lens and pupillary border of iris, iris transillumination defects, pigmented granules on trabecular meshwork, poor pupillary response in dilation, weak zonules
Reis-Bucklers Corneal Dystrophy	TGFBI	AD	Reticular opacities in Bowman's layer, recurrent corneal erosions
Retinitis Pigmentosa	Numerous	AD, AR, XLR	Progressive retinal degeneration, night blindness, constricted visual fields, dyschromatopsia, cystoid macular edema, pigment clumps in retina, attenuated retinal vessels, waxy pallor of optic disc, cataracts
Retinoblastoma	RB1	AD, sporadic	Leukcoria, strabismus, retinal detachment, glaucoma, pseudouveitis, proptosis, hyphema, orbital cellulitis, red painful eye
Retinoschisis, Juvenile X Linked	RS1	X-linked	Retinoschisis, retinal detachment, nystagmus, vitreous hemorrhage, cystic maculopathy
Schnyder Corneal Dysrophy	UBIAD1	AD	Corneal clouding in stroma yellow-white crystal deposits

DISORDER	KNOWN GENES OR CHROMOSOMAL ABNORMALITY INVOLVED	MODE OF INHERITANCE	EYE FINDING
Senior-Loken Syndrome	NPHP1, NPHP4 SDCCAG8, WDR19, CEP290, IQCB1	AR	Tapetoretinal degeneration, photophobia, nystagmus, hyperopia, flat electroretinogram
Septic-Optic Dysplasia (De Morsier Syndrome)	HESX1, OTX2, SOX2	AD, AR, sporadic	Optic nerve hypoplasia, nystagmus
Sorsby Fundus Dystrophy	TIMP3	AD	Progressive macular dystrophy, Night blindness
Stargardt Disease/Fundus Flavimaculatus	ABCA4 (majority cases), ELOVL4, PROM1	AD, AR	Progressive macular dystophy, central retinal atrophy, macular flecks, later disease onset and scattered flecks with Fundus Flavimaculatus
Syndromic Microphthalmia 1 (Lenz Microphthalmia Syndrome)	NAA10	X-linked	Anophthalmia, microphthalmia, microcornea, ptosis, colobomas
Syndromic Microphthalmia 2 (Oculofaciocardiodental Syndrome)	BCOR	XLD	Microphthalmia, microcornea, cataract, thick eyebrows, ptosis, bleparophimosis, strabismus
Syndromic Microphthalmia 3 (Microphthalmia And Esophageal Atresia Syndrome)	SOX2	AD	Anophthalmia, microphthalmia, coloboma, optic nerve hypoplasia
Syndromic Microphthalmia 4	-	X-linked	Anophthalmia, ankyloblepharon
Syndromic Microphthalmia 5	OTX2	AD	Anophthalmia, microphthalmia, microcornea, retinal dystrophy, optic nerve hypoplasia, colobomas
Syndromic Microphthalmia 6	BMP4	AD	Anophthalmia, microphthalmia
Syndromic Microphthalmia 7 (Midas Syndrome)	HCCS	XLD	Microphthalmia, cataracts, coloboma, sclerocornea, pigmentary retinopathy
Syndromic Microphthalmia 8	-	AD	Microphthalmia, Microcornea, short palpebral fissures
Syndromic Microphthalmia 9 (Matthew-Wood Syndrome)	STRA6	AR	Anophthalmia, microphthalmia, coloboma, optic nerve hypoplasia, blepharophimosis, broad eyebrows
Syndromic Microphthalmia 10	-	-	Microphthalmia
Syndromic Microphthalmia 11	VAX1	AR	Microphthalmia, optic nerve hypoplasia
Syndromic Microphthalmia 12	RARB	AD	Anophthalmia, microphthalmia
Syndromic Microphthalmia 13	HMGB3	X-linked	Microphthalmia, microcornea, ptosis, coloboma, nystagmus, esotropia
Syndromic Microphthalmia 14	MAB21L2	-	Microphthalmia, coloboma
Thiel-Behnke Corneal Dystrophy	TGFBI	AD	Honeycomb-shaped opacities in Bowman's layer, recurrent corneal erosions
Usher Syndrome	11 genes, majority of cases due to MYO7A, USH2A	AR	retinitis pigmentosa, cataracts

DISORDER	KNOWN GENES OR CHROMOSOMAL ABNORMALITY INVOLVED	MODE OF INHERITANCE	EYE FINDING
Vitelliform Macular Dystrophy, Adult-Onset	PRPH2, BEST1	AD	Yellow pigmented macular lesion, choroidal neovascularization, central retinal pigment epithelium atrophy
Wagner Syndrome	VCAN	AD	Myopia, vitreoretinal degeneration, chorioretinal atrophy, glaucoma, retinal detachment
Watson Syndrome	NF1	AD	Lisch nodules
Wolfram Syndrome	WFS1, CISD2	AR	Pigmentary retinopathy, optic atrophy, nystagmus, ptosis

AD = autosomal dominant; AR = autosomal recessive

One solution to bypass the BRB is to inject therapeutic agents directly into the vitreous humor where there is direct access to the internal ocular tissues (Figure 5-1). This approach has proven effective in several treatments including vascular endothelial growth factor inhibitors (anti-VEGF) such as Lucentis® (ranibizumab) used for age-related macular degeneration and diabetic macular edema.[210]

Another approach is to inject therapeutic agents into the subretinal space for direct delivery to the retinal pigmented epithelial (RPE) cells or photoreceptors located deep within the retina (Figure 5-1). There are inherent risks associated with subretinal injections as the process involves injecting a bleb beneath the retina, which results in an artificial, temporary retinal detachment. Usually this detachment self-corrects and there is no lasting damage, but there is an increased risk of permanent retinal damage, or damage that requires surgical intervention to correct.[211,212] For aggressive diseases such as Leber's congenital amaurosis (LCA) the risk may be acceptable, but for more slowly progressing diseases a less risky administration may be preferred.

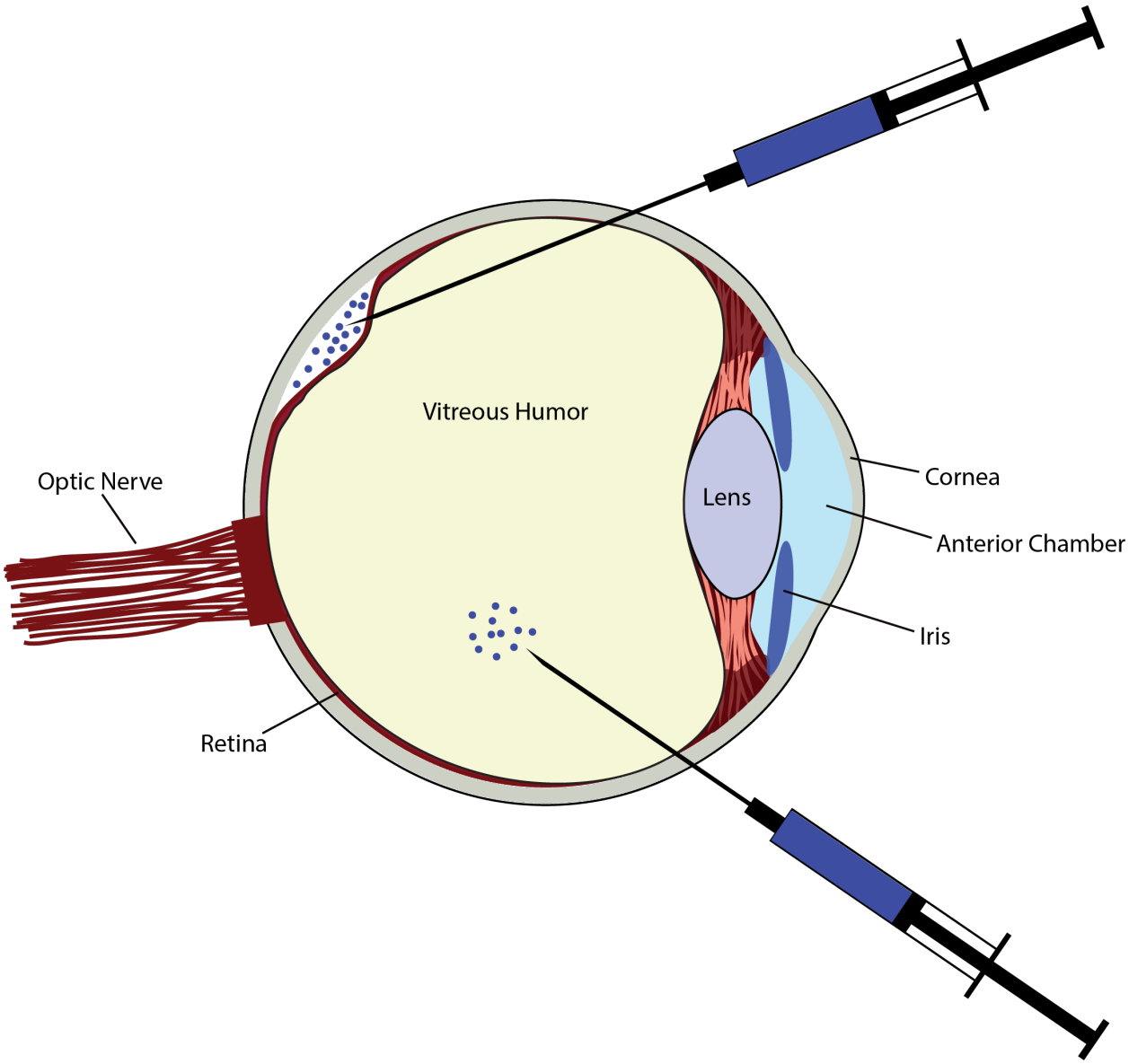

Figure 5-1. Ocular drug delivery. To bypass the blood-retinal barrier (BRB), therapeutic agents have been injected directly into the vitreous humor, or into the sub-retinal space for direct delivery to ocular tissues.

There are challenges, however, when the target is the RPE cells located at the deepest point of the retina (Figure 5-2).[46] The retina consists of several layers of neuronal tissues, as well as an inner limiting membrane located on the surface of the retina.[213] These barriers make delivery of therapeutic moieties a challenge for reaching the RPE cells from the intravitreal space.

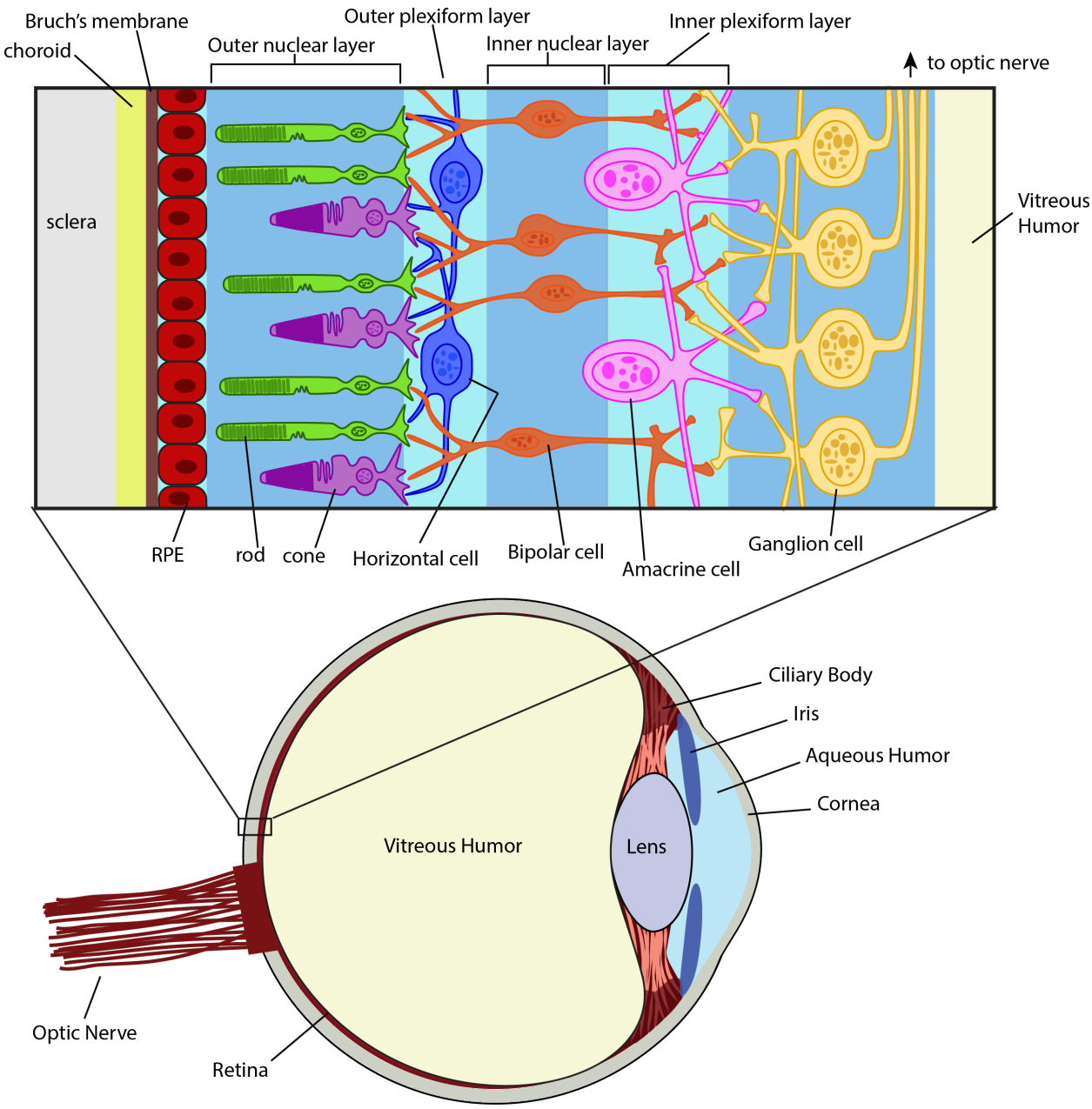

Figure 5-2. Anatomical structure of the retina. The retina (blowout panel) is a complex tissue comprised of layers of cells built on the structural foundation of the sclera, choroid and Bruch's membrane. The retinal pigmented epithelial (RPE) cells provide a base layer to support the structure and function of photoreceptor cells (rods and cones) located in the outer nuclear layer. When light enters the eye, it penetrates the retinal tissue and is absorbed by photoreceptor cells where it is converted into an electrical signal. A series of nerve-type cells (horizontal, bipolar and amacrine cells) form the outer plexiform, inner nuclear and inner plexiform layers, and are responsible for transmitting the electrical signal to the ganglion cells in the innermost layer of the retina. Ganglion cells connect to the optic nerve and transmit the visual signal to the brain. Adapted from reference [46].

5.2 Approaches to Gene Therapy

Adeno-associated viruses (AAV) were first identified in 1965 when they were isolated as contaminants in a preparation of simian adenovirus.[214] AAVs are members of the *Dependovirus* genus in the family *Parvoviridae*, and are non-pathogenic in human hosts.[215]

5.2.1 Adeno-Associated Virus Vectors for Ocular Delivery

AAV vectors have been identified as robust vehicles for delivery of human DNA to targeted ocular cells without causing peripheral pathology, including delivery after intravitreal administration.[211,213,216-219] Unlike adenovirus, which can cause immunogenicity in the host, AAVs show no pathology so exposing ocular tissue to these vectors is not a significant safety concern.[216] There are 9 predominant serotypes at this time (AAV 1 through 9), with others being identified regularly in the literature, but AAV2 has been most studied as a gene delivery vector.[220,221] As research into AAV vector design continues to mature, there are a variety of engineered vectors currently being used to facilitate more precise cellular targeting.[220] Modifications are primarily focused on alterations in the capsid proteins, and generally fall under four categories: transcapsidation, in which the primary genetic information of one serotype is packaged inside the capsid of a different serotype; adsorption modification, in which targeting peptides are adsorbed on the surface of the capsid; mosaic, in which a mixture of capsid proteins from different serotypes are combined; and chimeric, in which a foreign protein sequence is inserted into the open reading frame of the capsid gene.[220] Therapeutic AAV-mediated gene delivery is proving useful in treating ocular diseases with their capability to target many cell types, and ability to carry payload sufficiently large to deliver genetic material.

5.3 Treatment of Ocular Disorders

5.3.1 Leber's Congenital Amaurosis

Some success has been achieved by subretinal injections of adeno-associated virus (AAV) vectors containing a payload of human DNA for direct gene delivery to the RPE cells.[222-225] Early and late phase clinical trials have been conducted to evaluate the safety and efficacy of subretinal gene delivery therapy in patients with Leber's congenital amaurosis (LCA) using rAAV2/2 serotype vectors to target the RPE cells.[226]

LCA is a rare disease, affecting approximately 1 in 80,000 individuals.[227] The disease is caused by mutations in any of 13 genes, following an autosomal recessive inheritance pattern.[227,228] Approximately ten percent of LCA patients have mutations in the *RPE65* gene, which encodes the protein RPE65 that is essential in regeneration of visual pigments and recharging the light sensitivity of photoreceptors.[229] This causative mutation was first identified in 1997, and is perhaps the best characterized mutation in LCA.[230] Defective *RPE65* is the target of gene augmentation therapy currently undergoing clinical trials. LCA begins in childhood with severe visual impairment and night blindness. Retinal degeneration progresses over time until the patient is completely blind by the time they reach 20 to 30 years of age.[231]

5.3.1.1 Phase I Clinical Trials

A Phase I trial was conducted at the Children's Hospital of Philadelphia to evaluate the most effective dose of the AAV2 vector packaged with wild-type, human cDNA for *RPE65* (AAV2-hRPE65v2).[225,228] A total of 12 LCA patients, aged 8 to 44 years, with a confirmed *RPE65* mutation were enrolled to receive treatment at one of three dosage levels in the eye that was determined to have the worst function. Patients underwent a standard three-port pars plana

vitrectomy, and the AAV vector was injected in a volume of 150 μL (low and medium-dose) or 300 μL (high-dose) directly into the subretinal space (Error! Reference source not found.). All induced retinal detachments resolved within 14 hours after surgery. Treatment was well tolerated, with no reported adverse events, and no harmful immune responses were detected.[228] Beginning approximately two weeks after surgery, all patients reported improved vision in dim lighting. Change in visual acuity was measurable and substantial in three low-dose patients, three medium-dose patients, and one high-dose patient. All patients experienced improved visual field, and there was no clear dose-response to safety or efficacy.[228] Response to treatment was dependent upon the extent of existing retinal degeneration, so typically the older patients with more pronounced degeneration had a lesser response than younger patients who had more retinal tissue that was still viable. The results overall showed improvement in visual function after treatment.

Another Phase I clinical trial was conducted in 15 patients in whom a recombinant AAV2 vector containing functional human *RPE65* (rAAV2-RPE65) was administered subretinally in the worse-functioning eye.[232-235] This study was an open-label study and patients received one of four different dosages in volumes ranging from 150 μL to 450 μL administered at one or two retinal sites.[235] Ocular adverse events occurred in nine patients, all related to the surgical procedure and not the AAV2 vector itself, and there was no systemic effect. Adverse events included extended retinal detachment in one patients that was repaired surgically, choroidal effusion in one patient that was treated and fully resolved after 238 days, ocular hypotension occurred in four patients during days two through five in the postoperative period which resolved naturally, and ocular hypertension was observed in three patients due to topical steroid use after surgery.[235] In all patients, light sensitivity improved significantly in the treated during the

postoperative period (1-6 months), with no change in the control eye, and visual field expanded in relation to the treated area. Visual acuity improved in treated eyes, but not to the extent commonly considered clinically significant. Three patients were observed longitudinally for up to six years and underwent clinical evaluation.[234] In all three patients, visual sensitivity increased by six months after treatment, and slowly continued to expand for up to three years, but then began to decline. The reason for the decline is not yet clear, although the authors suggested an association with thickness of the outer nuclear layer, which showed steady decline during the time when sensitivity changes were occurring. Furthermore, in spite of increased sensitivity, the rate of photoreceptor loss remained the same between treated and untreated eyes.[233,234]

A very small Phase I trial was conducted during the same period as those reported above to assess the safety and efficacy of subretinal injection of a recombinant AAV2 vector modified to carry the human *RPE65* gene (AAV2-CB^{SB}-h*RPE65*).[223,224,236,237] Three sequential patients aged 21 to 24 years were administered a uniocular dose (150 µL total volume) containing AAV2-CB^{SB}-h*RPE65* and followed for safety and tolerability, as well as any changes in clinical eye exam.[224] Administration of the vector was well tolerated by all three patients, with no clinically significant ocular or systemic abnormalities observed. At the 90-day follow-up, one patient had foveal thinning, but there were foveal abnormalities observed in that patient at baseline that may have been due to inherent retinal degeneration. Visual acuity improved from baseline for all patients, and all three self-reported improved vision in dim lighting.[224] The biophysical kinetics of photoreceptor resensitization was improved based on overcoming the biochemical blockade caused by dysfunctional RPE65 enzyme, but the recovery time of rods in these patients was still very slow.[223] In normal eyes, rods regain full light sensitivity in less than one hour, but in the treated eyes it took at least eight hours to regain sensitivity. Long-term follow-up of these three

patients showed the improvements in visual sensitivity observed at 3 months were still observed at 12- and 18- months post-administration.[236,237]

5.3.1.2 Phase I-II Clinical Trial

A Phase I-II open-label clinical trial was conducted first in three patients, then expanded to include 12 patients who were administered recombinant AAV2/2 vectors packaged with functional human complementary DNA (cDNA).[222,226] Vector administration was well tolerated and there were only mild ocular adverse events reported, including transient intraocular inflammation, and no systemic effects were reported.[226] Patients underwent clinical assessment at baseline, then at regular intervals for up to three years after vector administration. Retinal sensitivity improved in all but one patient, but visual acuity did not change. Long-term results showed that eyesight and light sensitivity shows improvement for up to three years before the benefit begins to decline.[226]

5.3.1.3 Phase III Clinical Trials

Phase III, open-label, randomized clinical trials are currently underway to further evaluate the safety and efficacy of gene therapy in patients age 3 years or older. This trial is ongoing, but results have not yet been reported at the time of this dissertation.

5.3.2 Colorblindness

Color blindness, or color vision deficiency, is a common disorder affecting approximately 1 in 12 men, and 1 in 200 women.[238] Usually a genetic condition, red-green color blindness is the most common single locus genetic disorder,[239] although other causes of color blindness include trauma, chronic illnesses including diabetes mellitus, glaucoma, macular

degeneration, and Parkinson's disease, and medications such as some antibiotics and hypertension treatments.[238] In humans, color vision arises from the presence of three types of cone photoreceptor cells that are sensitive to either short-, middle-, or long-wavelengths of light.[240] Red-green colorblindness occurs when either the long- or middle-wavelength-sensitive photopigments are absent.[239] The apparent neural-plasticity in the visual cortex as invited the possibility of curing color blindness through gene replacement therapy.[241]

Researchers at the University of Washington showed they were able to restore color vision behavior in adult squirrel monkeys that were missing the L-opsin gene sensitive to the long-wavelength stimulus.[239,241] Some female squirrel monkeys have full, trichromatic color vision, but males are red-green color blind. Before treatment, the monkeys were trained to respond to a color-vision test in which patches of color were displayed on a computer screen in which the background mosaic was grey. Colorblind monkeys were unable to distinguish colors in the blue-green and red-violet spectra. Monkeys were treated with subretinal administration of AAV2/5 vectors containing a functional human L-opsin gene. After treatment, monkeys repeatedly performed the computer-based color vision test, and by 20 weeks after treatment they exhibited behavior of trichromacy, or normal color vision.[239,241] This work provides promising evidence that gene replacement therapy may be a viable treatment for color blindness in humans.

5.4 Implications in Bietti's Crystalline Dystrophy

Bietti's crystalline dystrophy (BCD) is a rare, degenerative eye disease caused by genetic mutations in *CYP4V2* that result in non-functional CYP4V2 enzyme. As a genetically mediated disease, it is a potential candidate for gene replacement therapy similar to that of LCA. Like the RPE65 deficiency, the CYP4V2 deficiency is believed to manifest in the RPE, as the primary site of CYP4V2 expression in the human eye.

I have described the characterization of our *Cyp4v3*$^{-/-}$ mouse model (Chapter 2), which presents a viable preclinical animal platform to enable *in vivo* testing of potential therapeutic moieties. This will allow for a pilot study to assess the safety and efficacy of administering AAV vectors carrying a payload of a functional *CYP4V2* gene, delivered subretinally or intravitreally (Figure 5-1). With the success described above in LCA and color blindness, gene replacement therapy is a viable treatment approach that should be tested in a pilot study using our knockout mice. If the functional *CYP4V2* can be successfully delivered to RPE cells, it is likely that with a well-defined vector, the endogenous cellular machinery would commence production of health CYP4V2 enzyme. In spite of our limited understanding of the specific role played by CYP4V2 in the pathophysiology of BCD, it is conceivable that gene replacement therapy could augment the expression of CYP4V2 with functional enzyme. At the very least, it is reasonable to postulate that the course of disease could be modified by either decreasing disease progression or attenuation of the phenotypic abnormalities.

There are inherent risks in administering gene replacement therapy into the eye, with a risk of exposing vulnerable ocular tissue to xenobiotic pathogens and mechanical disruption of the eye. Studies described here have shown the relative safety of administering AAV vectors to successfully target cells located deep within the retina, so it is unlikely that the safety concerns will be sufficient to limit testing in BCD. Aside from gene replacement, there may be small molecule therapeutic moieties that could be able to treat the abnormal, crystalline, lipid deposits that were evident in retinas of our knockout mice. If the degeneration is due, at least in part, to the aberrant deposition of lipid-based aggregates, it is possible that disrupting the aggregation or deposition could slow disease progression. More work is needed to better understand the

mechanism behind the pathology to better identify therapeutic targets, but with the preclinical model presented here, there is now a viable means for investigating treatment options.

5.5 Conclusion

Gene replacement therapy is gaining traction as a viable treatment for some genetically-mediated ocular disorders such as Leber's congenital amaurosis (LCA) and color blindness. Since the eye is a physiologically isolated system, it is often difficult to deliver adequate treatment through systemic pathways. Therefore, it is reasonable, and in some cases necessary, to bypass the blood retinal barrier to deliver therapeutic agents directly to the ocular tissues by intravitreal or subretinal injection. Clinical studies in human LCA patients have shown promise with subretinal injection of recombinant AAV2 vectors that deliver functional human *RPE65* genes to retinal pigmented epithelial cells. After treatment, patients showed improved light sensitivity and improved visual acuity that persisted for up to three years before vision decline resumed. Similarly, preclinical studies in non-human primates have shown subretinal administration of recombinant AAV2/5 vectors containing functional human L-opsin genes restores normal color vision behavior.

While these studies have shown promise, research is still evolving. As we are able to better understand ocular physiology, and the targeted delivery capabilities of AAV vectors, researchers are hopeful that this may be a viable mechanism for treating otherwise untreatable diseases. There are still many questions surrounding the viability and persistence of gene replacement therapy in the eye, but these early studies show promise as a means of treating other genetically mediated ophthalmic diseases. There are opportunities for research in alternative ocular injection sites that are less invasive and may carry lower risk for complications than direct subretinal delivery. For aggressive blinding diseases such as LCA, the risk may be acceptable,

but for less sever diseases, or those with a longer temporal progression, it may be preferable to develop treatments that will target the retinal pigmented epithelium or other deep retinal tissues after intravitreal injection. Work is ongoing in this field, but there are exciting developments and opportunities for investigating this innovative treatment for ocular disease. The work described in this dissertation provides a foundation for better understanding the pathophysiology of BCD, and a viable platform for testing a promising therapeutic option in gene replacement therapy.

Chapter 6

Summary and General Conclusions

The work presented in this dissertation explores the physiological function of cytochrome P450 4V2 (CYP4V2), one of 57 known heme-containing oxidase enzymes. A member of family 4 due to its fatty-acid ω–hydroxylation activity, CYP4V2 is not well characterized in normal physiology, much less the deficiencies that arise due to lack of function in Bietti's crystalline dystrophy (BCD). We also sought to characterize the aberrant characteristics of CYP4V2 associated with a homozygous point mutation we identified in a patient with BCD. Additionally, the murine ortholog of CYP4V2 is Cyp4v3, so we developed and characterized a *Cyp4v3*$^{-/-}$ mouse model to serve as a preclinical platform for understanding the pathophysiology and phenotypic abnormalities observed in BCD. This mouse model can also be used to explore therapeutic options, including gene replacement therapy, for this devastating disease.

Overall, we showed that *Cyp4v3*$^{-/-}$ mice recapitulate the most significant elements of the phenotype observed in BCD, particularly the development of glistening yellow-white crystalline deposits in the retinal tissue, a defining characteristic of BCD. In a patient with BCD, we successfully determined her genotype, the first homozygous point mutation that had previously only been reported as one allele in a compound heterozygous patient. We also were the first to develop a sequence homology model describing the functional deficiency caused by this homozygous point mutation. In an effort to elucidate the biochemistry of CYP4V2 in normal physiological function, we showed strong evidence that CYP4V2 is influenced by regulatory pressure of microRNA (miR-146b-5p). Finally, we described rationale for conducting a pilot gene replacement therapy study in our knockout mouse model using an adeno-associated virus (AAV) vector packaged with functional CYP4V2 cDNA.

In Chapter 2, we showed that *Cyp4v3*$^{-/-}$ mice display the hallmark yellow-white crystalline deposits that define BCD, with a temporal progression similar to that observed in

BCD patients. Furthermore, these knockout mice have a systemic dyslipidemia that reflects some of the lipid imbalance that occurs in BCD patients, although the specific lipids that are abnormal in mice differ somewhat to those observed in humans, the overall dyslipidemia is consistent. Previously, it was not possible to analyze the composition of the crystalline deposits that develop in BCD patients due to the lack of available tissue from diseased eyes. Due to the progressive retinal degeneration that occurs as a result of this disease, the crystalline deposits disappear as the degeneration becomes extensive, so cadaver eye tissue from BCD patients no longer displays the crystalline deposits. With the generation of our knockout mouse model, we were able to conduct experiments to evaluate the general histology and biochemistry of the crystalline deposits. We showed through immunohistochemistry and transmission electron microscopy that the crystalline abnormalities are likely lipid-based, which correlates with the known substrate specificity of CYP4V2 for medium-chain fatty acids. We do not yet know the exact composition of those lipid deposits, but lipidomic studies are ongoing to characterize the lipid abnormalities present in the ocular tissue of these mice.

In addition to fundus images that revealed the presence of crystalline deposits in the retina of this mouse model, we have conducted additional tests for visual acuity and function, in collaboration with colleagues at Oregon Health and Science University. Electroretinograms showed the electrical conductivity of the retinas of 12- and 18-month old mice reflected normal retinal function. Visual acuity, as measured by optokinetic reflext testing, also showed results within the range of normal mice based on the age. Finally, optical coherence tomography (OCT) images were collected to evaluate the structural characteristics of retinal tissue, and to identify if the lipid-based crystalline deposits that were present in histological sections were also visible *in vivo* with cross-sectional retinal images. There were no obvious abnormalities visible with the

OCT imagery, but it is possible that the scale of the lipid deposits identified in histological sections were too flat in conformation to be detected on the relative scale of OCT images. It is not clear if these normal findings reflect a difference in disease pathogenesis observed in mice compared to that in humans, or if the means of evaluation are not appropriate for identifying the functional characteristics and phenotype that we hope to express. With the presence of a clear temporal progression of crystalline deposits, however, we have a platform that would be a viable model for conducting pilot studies of gene replacement therapy to investigate any influence on disease phenotype or progression. Then this preclinical model can be used to further describe the abnormalities that emerge as a result of BCD, as that is not yet understood.

In Chapter 3, we sought to identify the genotype of a patient with BCD who had not had here genetic sequence successfully analyzed before. We found that she was homozygous for a point mutation resulting in replacement of arginine with cysteine at nucleotide 400 that has previously only been described as a component of a compound heterozygous patient. We developed a sequence homology model to compare the estimated wild-type CYP4V2 structure with that of a model reflecting the point mutation in our patient. We showed that the arginine likely mediates an essential hydrogen-bonding interaction with the heme moiety, such that when that interaction is lost with cysteine in that position, the putative active site defined by the heme moiety falls out of position, or fails to be incorporated.

In Chapter 4, we sought to identify potential regulatory pathways that govern CYP4V2 homeostasis in normal physiology. Using human liver tissue from the University of Washington liver bank, we conducted a microarray analysis to screen microRNAs with the potential for a regulatory interaction with CYP4V2 and identified miR-146b-5p as a candidate. In liver tissue samples, we showed that expression of CYP4V2 mRNA was positively associated with

expression of CYP4V2 protein, and that expression of CYP4V2 protein was negatively associated with miR-146b-5p expression. These results suggest a potential regulatory interaction such that miR-146b-5p suppresses expression of CYP4V2. From these data we were unable to discern the mechanism of regulation, whether or not it arose from a direct interaction between miR-146b-5p and the 3'UTR of CYP4V2, which is a typical binding site for microRNA.

To further characterize the regulatory mechanism, we transfected HepG2 cells and ARPE-19 cells with plasmids to overexpress miR-146b-5p. If there is a direct interaction with the 3'UTR of CYP4V2 mRNA, we expected to see decreased expression, measured by fluorescence intensity, of CYP4V2 in cells that overexpressed miR-146b-5p. HepG2 cells were stably transfected, while ARPE-19 cells were transiently transfected and then analyzed for luciferase or fluorescent activity, respectively. Luciferase activity from stably transfected HepG2 cells showed trends toward decreased expression in cells that overexpressed miR-146b-5p, but the data were extremely variable so is inconclusive whether direct binding by miR-146b-5p to the 3'UTR of CYP4V2 causes the regulatory effects. We transiently transfected ARPE-19 cells, the primary site of CYP4V2 expression in the eye, to evaluate miR-146b-5p interaction in cells that are most physiologically relevant to BCD. Transfection efficiency of ARPE-19 cells was fair, at approximately 20%. Visually, CYP4V2 expression as identified by a red fluorescent signal in our assay, appeared to be higher in non-transfected cells than in those transfected to overexpress miR-146b-5p; however, when fluorescence intensity was directly measured the results were similar between cells that had been transfected to overexpress miR-146b-5p and those transfected with a non-binding control. Therefore, it is still not clear whether the mechanism of regulation is mediated by direct binding to the CYP4V2 3'UTR or via a secondary pathway. Absolute protein quantitation suggested that CYP4V2 protein expression may be

decreased in cells transfected to overexpress miR-146b-5p, compared to controls, but the analysis needs to be repeated to confirm the initial results.

Chapter 5 describes the state of gene therapy as it relates to ocular diseases. There have been some promising results in Leber's congenital amaurosis (LCA) patients treated with adeno-associated virus (AAV) mediated gene delivery administered in the subretinal space. There has also been success in treating colorblindness with gene-replacement therapy, as described by colleagues in ophthalmology at the University of Washington. This provides a promising approach for treatment of BCD, which can be evaluated in our preclinical knockout mouse model. Work toward conducting a pilot study is ongoing, but we are hopeful that a successful study is feasible and will provide valuable information on pathogenesis as well as treatment options for this devastating disease.

In summary, this dissertation presented a collection of studies aimed at better characterizing CYP4V2 in normal physiological function, and to begin to elucidate the aberrant physiology observed in BCD. We developed a knockout mouse model that recapitulates the hallmark phenotype observed in BCD, and is a promising preclinical model for further evaluation of the pathophysiology of BCD, as well as a platform for screening potential therapeutic options, including gene replacement therapy or treatment with small molecule candidates.

References

1. Kumar S. Comparative modeling and molecular docking of orphan human CYP4V2 protein with fatty acid substrates: Insights into substrate specificity. Bioinformation 2011;7:360-5.
2. Rettie AE, Kelly EJ. The CYP4 Family. In: Ioannides C, ed. Issues in Toxicology Cytochrome P450: Role in the metabolism and toxicity of drugs and other xenobiotics. London: Royal Society of Chemistry; 2008.
3. Kirischian NL, Wilson JY. Phylogenetic and functional analyses of the cytochrome P450 family 4. Molecular phylogenetics and evolution 2012;62:458-71.
4. Benenati G, Penkov S, Muller-Reichert T, Entchev EV, Kurzchalia TV. Two cytochrome P450s in Caenorhabditis elegans are essential for the organization of eggshell, correct execution of meiosis and the polarization of embryo. Mechanisms of development 2009;126:382-93.
5. Benenati G, Penkov S, Müller-Reichert T, Entchev EV, Kurzchalia TV. Two cytochrome P450s in Caenorhabditis elegans are essential for the organization of eggshell, correct execution of meiosis and the polarization of embryo. Mechanisms of Development 2009;126:382-93.
6. Mackay DS, Halford S. Focus on Molecules: Cytochrome P450 family 4, subfamily V, polypeptide 2 (CYP4V2). Exp Eye Res 2011.
7. Rettie AE, Kelly, E.J. The CYP4 Family. In: Ioannides C, ed. Issues in Toxicology Cytochome P450: Role in the metabolism and toxicity of drugs and other xenobiotics. London: Royal Society of Chemistry; 2008.
8. Nakano M, Kelly EJ, Rettie AE. Expression and Characterization of CYP4V2 as a Fatty Acid -Hydroxylase. Drug Metab Dispos 2009;37:2119-22.
9. Nakano M, Kelly EJ, Wiek C, Hanenberg H, Rettie AE. CYP4V2 in Bietti's crystalline dystrophy: ocular localization, metabolism of omega-3-polyunsaturated fatty acids, and functional deficit of the p.H331P variant. Molecular pharmacology 2012;82:679-86.
10. D'Andre HC, Paul W, Shen X, et al. Identification and characterization of genes that control fat deposition in chickens. J Animal Sci Biotechnol 2013;4:43.
11. Lai TY, Chu KO, Chan KP, et al. Alterations in serum fatty acid concentrations and desaturase activities in Bietti crystalline dystrophy unaffected by CYP4V2 genotypes. Investigative ophthalmology & visual science 2010;51:1092-7.
12. Lee J, Jiao X, Hejtmancik JF, Kaiser-Kupfer M, Chader GJ. Identification, Isolation, and Characterization of a 32-kDa Fatty Acid-Binding Protein Missing from Lymphocytes in Humans with Bietti Crystalline Dystrophy (BCD). Mol Genet Metab 1998;65:143-54.
13. Lee J, Jiao X, Hejtmancik JF, et al. The metabolism of fatty acids in human Bietti crystalline dystrophy. Investigative ophthalmology & visual science 2001;42:1707-14.
14. Safdar H, Cleuren ACA, Cheung KL, et al. Regulation of the *F11, Klkb1, Cyp4v3* gene cluster in livers of metabolically challenged mice. PLoS ONE 2013;8:e74637.
15. Li A, Jiao X, Munier FL, et al. Bietti Crystalline Corneoretinal Dystrophy is caused by mutations in the novel gene *CYP4V2*. Am J Hum Genet 2004;74:817-26.
16. Stark K, Guengerich FP. Characterization of Orphan Human Cytochromes P450. Drug Metab Rev 2007;39:627-37.
17. Li A, Jiao X, Munier FL, et al. Bietti crystalline corneoretinal dystrophy is caused by mutations in the novel gene CYP4V2. American journal of human genetics 2004;74:817-26.

18. Kelly EJ, Nakano M, Rohatgi P, Yarov-Yarovoy V, Rettie AE. Finding Homes for Orphan Cytochrome P450s: CYP4V2 and CYP4F22 in Disease States. Mol Intervention 2011;11:124-32.
19. Chung JK, Shin JH, Jeon BR, Ki CS, Park TK. Optical coherence tomographic findings of crystal deposits in the lens and cornea in Bietti crystalline corneoretinopathy associated with mutation in the CYP4V2 gene. Japanese journal of ophthalmology 2013;57:447-50.
20. Garcia-Garcia G-P, Lopez-Garrido M-P, Martinez-Rubio M, Moya-Moya M-A, Belmonte-Martinez J, Escribano J. Genotype-Phenotype Analysis of Bietti Crystalline Dystrophy in a Family with the *CYP4V2* Ile111Thr Mutation. Cornea 2013;0:1-7.
21. Rossi S, Testa F, Li A, et al. Clinical and genetic features in Italian Bietti crystalline dystrophy patients. Br J Ophthalmol 2012;97:174-9.
22. Rossi S, Testa F, Li A, et al. An Atypical Form of Bietti Crystalline Dystrophy. Ophthalmic Genet 2011;32:118-21.
23. Xiao X, Mai G, Li S, Guo X, Zhang Q. Identification of CYP4V2 mutation in 21 families and overview of mutation spectrum in Bietti crystalline corneoretinal dystrophy. Biochem Biophys Res Commun 2011;409:181-6.
24. Haddad NMN, Waked N, Bejjani R, et al. Clinical and molecular findings in three Lebanese families with Bietti crystalline dystrophy: report on a novel mutation. Mol Vis 2012;18:1182-8.
25. Jin Z-B, Ito S, Saito Y, Inoue Y, Yanagi Y, Nao-i N. Clinical and Molecular Findings in Three Japanese Patients with Crystalline Retinopathy. Japanese journal of ophthalmology 2006;50:426-31.
26. Lai TYY, Ng TK, Tam POS, et al. Genotype Phenotype Analysis of Bietti's Crystalline Dystrophy in Patients with CYP4V2 Mutations. Invest Ophthalmol Vis Sci 2007;48:5212-20.
27. Lee KY, Koh AH, Aung T, et al. Characterization of Bietti crystalline dystrophy patients with CYP4V2 mutations. Investigative ophthalmology & visual science 2005;46:3812-6.
28. Lin J, Nishiguchi KM, Nakamura M, Dryja TP, Berson EL, Miyake Y. Recessive mutations in the CYP4V2 gene in East Asian and Middle Eastern patients with Bietti crystalline corneoretinal dystrophy. Journal of medical genetics 2005;42:e38.
29. Liu DN, Liu Y, Meng XH, Yin ZQ. The characterization of functional disturbances in Chinese patients with Bietti's crystalline dystrophy at different fundus stages. Graefes Arch Clin Exp Ophthalmol 2011;250:191-200.
30. Mamatha G, Umashankar V, Kasinathan N, et al. Molecular screening of the *CYP4V2* gene in Bietti crystalline dystrophy that is associated with choroidal neovascularization. Mol Vis 2011;17:1970-7.
31. Parravano M, Sciamanna M, Giorno P, Boninfante A, Varano M. Bietti crystalline dystrophy: a morpho-functional evaluation. Doc Ophthalmol 2011;124:73-7.
32. Porter LF, Urquhart JE, O'Donoghue E, et al. Identification of a Novel Locus for Autosomal Dominant Primary Open Angle Glaucoma on 4q35.1-q35.2. Invest Ophthalmol Vis Sci 2011;52:7859-65.
33. Shan M, Dong B, Zhao X, et al. Novel mutations in teh *CYP4V2* gene associated wtih Bietti crystalline corneoretinal dystrophy. Mol Vis 2005;11:738-43.
34. Wada Y, Itabashi T, Sato H, Kawamura M, Tada A, Tamai M. Screening for Mutations in CYP4V2 Gene in Japanese Patients With Bietti's Crystalline Corneoretinal Dystrophy. Am J Ophthalmol 2005;139:894-9.

35. Wang Y, Guo L, Cai S-P, et al. Exome Sequencing Identifies Compound Heterozygous Mutations in CYP4V2 in a Pedigree with Retinitis Pigmentosa. PLoS ONE 2012;7:e33673.
36. Yokoi Y, Sato K, Aoyagi H, Takahashi Y, Yamagami M, Nakazawa M. A Novel Compound Heterozygous Mutation in the CYP4V2 Gene in a Japanese Patient with Bietti's Crystalline Corneoretinal Dystrophy. Case Reports Ophthalmol 2011;2:296-301.
37. Yokoi Y, Nakazawa M, Mizukoshi S, Sato K, Usui T, Takeuchi K. Crystal deposits on the lens capsules in Bietti crystalline corneoretinal dystrophy associated with a mutation in the CYP4V2 gene. Acta Ophthalmol 2009;88:607-9.
38. Zenteno JC, Ayala-Ramirez R, Graue-Wiechers F. Novel CYP4V2 Gene Mutation in a Mexican Patient with Bietti's Crystalline Corneoretinal Dystrophy. Curr Eye Res 2008;33:313-8.
39. Song Y, Mo G, Yin G. A novel mutation in the CYP4V2 gene in a Chinese patient with Bietti's crystalline dystrophy. International ophthalmology 2013;33:269-76.
40. Yin H, Jin C, Fang X, et al. Molecular analysis and phenotypic study in 14 Chinese families with Bietti crystalline dystrophy. PloS one 2014;9:e94960.
41. Halford S, Liew G, Mackay DS, et al. Detailed Phenotypic and Genotypic Characterization of Bietti Crystalline Dystrophy. Ophthalmology 2014.
42. Bezemer ID, Bare LA, Doggen CJM, et al. Gene variants associated wtih deep vein thrombosis. JAMA 2008;299:1306-14.
43. Austin H, De Staercke C, Lally C, Bezemer ID, Rosendaal FR, Hooper WC. New gene variants associated with venous thrombosis: a replication study in White and Black Americans. Journal of Thrombosis and Haemostasis 2011;9:489-95.
44. Murray GI, Patimalla S, Stewart KN, Miller ID, Heys SD. Profiling the expression of cytochrome P450 in breast cancer. Histopathology 2010;57:202-11.
45. Chen M-S, Hou P-K, Tai T-Y, Lin B. Blood-Ocular Barriers. Tzu Chi Med J 2008;20:25-34.
46. Nakano M, Lockhart CM, Kelly EJ, Rettie AE. Ocular cytochrome P450s and transporters: roles in disease and endobiotic and xenobiotic disposition. Drug metabolism reviews 2014;46:247-60.
47. Bishop PN. Structural macromolecules and supramolecular organisation of the vitreous gel. Progress in retinal and eye research 2000;19:323-44.
48. Cunningham ET, Augsburger JJ, Z.M. C, Pavesio C. Chapter 7. Uveal Tract & Sclera. In: Riordan-Eva P, Cunningham ET, Jr. , eds. Vaughan & Asbury's General Ophthalmology, 18e New York, NY: McGraw-Hill; 2011.
49. Riordan-Eva P. Chapter 1. Anatomy & Embryology of the Eye. In: Riordan-Eva P, Cunningham ET, Jr, eds. Vaughan & Asbury's General Ophthalmology, 18e. New York, NY: McGraw-Hill; 2011.
50. Fletcher EC, Chong N, Augsburger JJ, Correa ZM. Chapter 10. Retina. In: Riordan-Eva P, Cunningham ET, Jr, eds. Vaughan & Asbury's General Ophthalmology. New York, NY: McGraw-Hill; 2011.
51. Strauss O. The Retinal Pigment Epithelium. In: Kolb H, Fernandez E, Nelson R, eds. Webvision: The Organization of the Retina and Visual System. Salt Lake City (UT)1995.
52. Ganea E, Harding JJ. Glutathione-related enzymes and the eye. Current eye research 2006;31:1-11.
53. Ueta T, Inoue T, Furukawa T, et al. Glutathione peroxidase 4 is required for maturation of photoreceptor cells. The Journal of biological chemistry 2012;287:7675-82.

54. Biswell R. Chapter 6. Cornea. In: Riordan-Eva P, Cunningham ET, Jr, eds. Vaughan & Asbury's General Ophthalmology, 183. New York, NY: McGraw-Hill; 2011.
55. Harper RA, Shock JP. Chapter 8. Lens. In: Riordan-Eva P, Cunningham ET, Jr, eds. Vaughan & Asbury's General Ophthalmology, 18e. New York, NY: McGraw-Hill; 2011.
56. Fu Y. Phototransduction in Rods and Cones. In: Kolb H, Fernandez E, Nelson R, eds. Webvision: The Organization of the Retina and Visual System. Salt Lake City (UT)1995.
57. Wolf G. The visual cycle of the cone photoreceptors of the retina. Nutrition reviews 2004;62:283-6.
58. Cunha-Vaz J. The blood-ocular barriers. Survey of ophthalmology 1979;23:279-96.
59. Cunha-Vaz JG. The blood-retinal barriers system. Basic concepts and clinical evaluation. Experimental eye research 2004;78:715-21.
60. Dahlin A, Geier E, Stocker SL, et al. Gene expression profiling of transporters in the solute carrier and ATP-binding cassette superfamilies in human eye substructures. Molecular pharmaceutics 2013;10:650-63.
61. Jain-Vakkalagadda B, Dey S, Pal D, Mitra AK. Identification and functional characterization of a Na+-independent large neutral amino acid transporter, LAT1, in human and rabbit cornea. Investigative ophthalmology & visual science 2003;44:2919-27.
62. Jain-Vakkalagadda B, Pal D, Gunda S, Nashed Y, Ganapathy V, Mitra AK. Identification of a Na+-dependent cationic and neutral amino acid transporter, B(0,+), in human and rabbit cornea. Molecular pharmaceutics 2004;1:338-46.
63. Dey S, Patel J, Anand BS, et al. Molecular evidence and functional expression of P-glycoprotein (MDR1) in human and rabbit cornea and corneal epithelial cell lines. Investigative ophthalmology & visual science 2003;44:2909-18.
64. Karla PK, Pal D, Mitra AK. Molecular evidence and functional expression of multidrug resistance associated protein (MRP) in rabbit corneal epithelial cells. Experimental eye research 2007;84:53-60.
65. Karla PK, Pal D, Quinn T, Mitra AK. Molecular evidence and functional expression of a novel drug efflux pump (ABCC2) in human corneal epithelium and rabbit cornea and its role in ocular drug efflux. International journal of pharmaceutics 2007;336:12-21.
66. Chen P, Chen H, Zang X, et al. Expression of efflux transporters in human ocular tissues. Drug metabolism and disposition: the biological fate of chemicals 2013;41:1934-48.
67. Barot M, Gokulgandhi MR, Pal D, Mitra AK. Mitochondrial localization of P-glycoprotein and peptide transporters in corneal epithelial cells--novel strategies for intracellular drug targeting. Experimental eye research 2013;106:47-54.
68. Mannermaa E, Vellonen KS, Urtti A. Drug transport in corneal epithelium and blood-retina barrier: emerging role of transporters in ocular pharmacokinetics. Advanced drug delivery reviews 2006;58:1136-63.
69. Hosoya K, Tomi M. Advances in the cell biology of transport via the inner blood-retinal barrier: establishment of cell lines and transport functions. Biological & pharmaceutical bulletin 2005;28:1-8.
70. Hosoya K, Tachikawa M. Inner blood-retinal barrier transporters: role of retinal drug delivery. Pharmaceutical research 2009;26:2055-65.
71. Zhang T, Xiang CD, Gale D, Carreiro S, Wu EY, Zhang EY. Drug transporter and cytochrome P450 mRNA expression in human ocular barriers: implications for ocular drug disposition. Drug metabolism and disposition: the biological fate of chemicals 2008;36:1300-7.

72. Prasad B, Evers R, Gupta A, et al. Interindividual variability in hepatic organic anion-transporting polypeptides and P-glycoprotein (ABCB1) protein expression: quantification by liquid chromatography tandem mass spectroscopy and influence of genotype, age, and sex. Drug metabolism and disposition: the biological fate of chemicals 2014;42:78-88.
73. Bietti G. Ueber familiaeres vorkommen von “retinitis punctata albescens” (verbunden mit “dystrophia marginalis cristallinea corneae”), glitzern des glaskoerpers und anderen degenerativen augenveraenderungen. Klin Mbl Augenheilk 1937;99:21.
74. Chan WM, Pang CP, Leung AT, Fan DS, Cheng AC, Lam DS. Bietti crystalline retinopathy affecting all 3 male siblings in a family. Archives of ophthalmology 2000;118:129-31.
75. Kaiser-Kupfer MI, Chan CC, Markello TC, et al. Clinical biochemical and pathologic correlations in Bietti's crystalline dystrophy. American journal of ophthalmology 1994;118:569-82.
76. Hartong DT, Berson EL, Dryja TP. Retinitis pigmentosa. Lancet 2006;368:1795-809.
77. Mataftsi A, Zografos L, Milla E, Secretan M, Munier FL. Bietti's crystalline corneoretinal dystrophy: a cross-sectional study. Retina 2004;24:416-26.
78. Okialda KA, Stover NB, Weleber RG, Kelly EJ. Bietti Crystalline Dystrophy. In: Pagon RA, Adam MP, Ardinger HH, et al., eds. GeneReviews(R). Seattle (WA)1993.
79. Kelly EJ, Nakano M, Rohatgi P, Yarov-Yarovoy V, Rettie AE. Finding homes for orphan cytochrome P450s: CYP4V2 and CYP4F22 in disease states. Molecular interventions 2011;11:124-32.
80. Ayata A, Tatlipinar S, Unal M, Ersanli D, Bilge AH. Autofluorescence and OCT features of Bietti's crystalline dystrophy. The British journal of ophthalmology 2008;92:718-20.
81. Fong AM, Koh A, Lee K, Ang CL. Bietti's crystalline dystrophy in Asians: clinical, angiographic and electrophysiological characteristics. International ophthalmology 2009;29:459-70.
82. Garcia-Garcia GP, Lopez-Garrido MP, Martinez-Rubio M, Moya-Moya MA, Belmonte-Martinez J, Escribano J. Genotype-phenotype analysis of Bietti crystalline dystrophy in a family with the CYP4V2 Ile111Thr mutation. Cornea 2013;32:1002-8.
83. Rossi S, Testa F, Li A, et al. Clinical and genetic features in Italian Bietti crystalline dystrophy patients. The British journal of ophthalmology 2013;97:174-9.
84. Rossi S, Testa F, Li A, et al. An atypical form of Bietti crystalline dystrophy. Ophthalmic genetics 2011;32:118-21.
85. Astuti GD, Sun V, Bauwens M, et al. Novel insights into the molecular pathogenesis of CYP4V2-associated Bietti's retinal dystrophy. Molecular genetics & genomic medicine 2015;3:14-29.
86. Spector RH. Visual Fields. In: Walker HK, Hall WD, Hurst JW, eds. Clinical Methods: The History, Physical, and Laboratory Examinations. 3rd ed. Boston1990.
87. Saatci AO, Doruk HC, Yaman A, Oner FH. Spectral domain optical coherence tomographic findings of bietti crystalline dystrophy. Journal of ophthalmology 2014;2014:739271.
88. Lee J, Jiao X, Hejtmancik JF, Kaiser-Kupfer M, Chader GJ. Identification, isolation, and characterization of a 32-kDa fatty acid-binding protein missing from lymphocytes in humans with Bietti crystalline dystrophy (BCD). Molecular genetics and metabolism 1998;65:143-54.

89. Nakano M, Kelly EJ, Rettie AE. Expression and characterization of CYP4V2 as a fatty acid omega-hydroxylase. Drug metabolism and disposition: the biological fate of chemicals 2009;37:2119-22.
90. Stark K, Guengerich FP. Characterization of orphan human cytochromes P450. Drug metabolism reviews 2007;39:627-37.
91. Mackay DS, Halford S. Focus on molecules: cytochrome P450 family 4, subfamily V, polypeptide 2 (CYP4V2). Experimental eye research 2012;102:111-2.
92. Gordon WC, Bazan NG. Visualization of [3H]docosahexaenoic acid trafficking through photoreceptors and retinal pigment epithelium by electron microscopic autoradiography. Investigative ophthalmology & visual science 1993;34:2402-11.
93. Ariel A, Serhan CN. Resolvins and protectins in the termination program of acute inflammation. Trends in immunology 2007;28:176-83.
94. Bazan NG. Neuroprotectin D1-mediated anti-inflammatory and survival signaling in stroke, retinal degenerations, and Alzheimer's disease. Journal of lipid research 2009;50 Suppl:S400-5.
95. Christmas P, Ursino SR, Fox JW, Soberman RJ. Expression of the CYP4F3 gene. tissue-specific splicing and alternative promoters generate high and low K(m) forms of leukotriene B(4) omega-hydroxylase. The Journal of biological chemistry 1999;274:21191-9.
96. Gekka T, Hayashi T, Takeuchi T, Goto-Omoto S, Kitahara K. CYP4V2 mutations in two Japanese patients with Bietti's crystalline dystrophy. Ophthalmic research 2005;37:262-9.
97. Gocho K, Kameya S, Akeo K, et al. High-Resolution Imaging of Patients with Bietti Crystalline Dystrophy with CYP4V2 Mutation. Journal of ophthalmology 2014;2014:283603.
98. Haddad NM, Waked N, Bejjani R, et al. Clinical and molecular findings in three Lebanese families with Bietti crystalline dystrophy: report on a novel mutation. Molecular vision 2012;18:1182-8.
99. Halford S, Liew G, Mackay DS, et al. Detailed phenotypic and genotypic characterization of bietti crystalline dystrophy. Ophthalmology 2014;121:1174-84.
100. Jin ZB, Ito S, Saito Y, Inoue Y, Yanagi Y, Nao-i N. Clinical and molecular findings in three Japanese patients with crystalline retinopathy. Japanese journal of ophthalmology 2006;50:426-31.
101. Lai TY, Ng TK, Tam PO, et al. Genotype phenotype analysis of Bietti's crystalline dystrophy in patients with CYP4V2 mutations. Investigative ophthalmology & visual science 2007;48:5212-20.
102. Chung SH, Gillies M, Sugiyama Y, Zhu L, Lee SR, Shen W. Profiling of microRNAs involved in retinal degeneration caused by selective Muller cell ablation. PloS one 2015;10:e0118949.
103. Liu DN, Liu Y, Meng XH, Yin ZQ. The characterization of functional disturbances in Chinese patients with Bietti's crystalline dystrophy at different fundus stages. Graefe's archive for clinical and experimental ophthalmology = Albrecht von Graefes Archiv fur klinische und experimentelle Ophthalmologie 2012;250:191-200.
104. Mamatha G, Umashankar V, Kasinathan N, et al. Molecular screening of the CYP4V2 gene in Bietti crystalline dystrophy that is associated with choroidal neovascularization. Molecular vision 2011;17:1970-7.
105. Manzouri B, Sergouniotis PI, Robson AG, Webster AR, Moore A. Bietti crystalline retinopathy: report of retinal crystal deposition in male adolescent siblings. Archives of ophthalmology 2012;130:1470-3.

106. Meng XH, Guo H, Xu HW, et al. Identification of novel CYP4V2 gene mutations in 92 Chinese families with Bietti's crystalline corneoretinal dystrophy. Molecular vision 2014;20:1806-14.
107. Nakamura M, Lin J, Nishiguchi K, Kondo M, Sugita J, Miyake Y. Bietti crystalline corneoretinal dystrophy associated with CYP4V2 gene mutations. Advances in experimental medicine and biology 2006;572:49-53.
108. Park YJ, Hwang DJ, Seong MW, Park SS, Woo SJ. Bietti Crystalline Retinopathy Confirmed by Mutation of CYP4V2 Gene in a Korean Patient. Korean journal of ophthalmology : KJO 2016;30:81-3.
109. Parravano M, Sciamanna M, Giorno P, Boninfante A, Varano M. Bietti crystalline dystrophy: a morpho-functional evaluation. Documenta ophthalmologica Advances in ophthalmology 2012;124:73-7.
110. Porter LF, Urquhart JE, O'Donoghue E, et al. Identification of a novel locus for autosomal dominant primary open angle glaucoma on 4q35.1-q35.2. Investigative ophthalmology & visual science 2011;52:7859-65.
111. Shan M, Dong B, Zhao X, et al. Novel mutations in the CYP4V2 gene associated with Bietti crystalline corneoretinal dystrophy. Molecular vision 2005;11:738-43.
112. Tian R, Wang SR, Wang J, Chen YX. Novel CYP4V2 mutations associated with Bietti crystalline corneoretinal dystrophy in Chinese patients. International journal of ophthalmology 2015;8:465-9.
113. Wada Y, Itabashi T, Sato H, Kawamura M, Tada A, Tamai M. Screening for mutations in CYP4V2 gene in Japanese patients with Bietti's crystalline corneoretinal dystrophy. American journal of ophthalmology 2005;139:894-9.
114. Wang Y, Guo L, Cai SP, et al. Exome sequencing identifies compound heterozygous mutations in CYP4V2 in a pedigree with retinitis pigmentosa. PloS one 2012;7:e33673.
115. Xiao X, Mai G, Li S, Guo X, Zhang Q. Identification of CYP4V2 mutation in 21 families and overview of mutation spectrum in Bietti crystalline corneoretinal dystrophy. Biochemical and biophysical research communications 2011;409:181-6.
116. Yin X, Yang L, Chen N, et al. Identification of CYP4V2 mutation in 36 Chinese families with Bietti crystalline corneoretinal dystrophy. Experimental eye research 2016;146:154-62.
117. Yokoi Y, Nakazawa M, Mizukoshi S, Sato K, Usui T, Takeuchi K. Crystal deposits on the lens capsules in Bietti crystalline corneoretinal dystrophy associated with a mutation in the CYP4V2 gene. Acta ophthalmologica 2010;88:607-9.
118. Yokoi Y, Sato K, Aoyagi H, Takahashi Y, Yamagami M, Nakazawa M. A Novel Compound Heterozygous Mutation in the CYP4V2 Gene in a Japanese Patient with Bietti's Crystalline Corneoretinal Dystrophy. Case reports in ophthalmology 2011;2:296-301.
119. Zenteno JC, Ayala-Ramirez R, Graue-Wiechers F. Novel CYP4V2 gene mutation in a Mexican patient with Bietti's crystalline corneoretinal dystrophy. Current eye research 2008;33:313-8.
120. Teeuw ME, Henneman L, Bochdanovits Z, et al. Do consanguineous parents of a child affected by an autosomal recessive disease have more DNA identical-by-descent than similarly-related parents with healthy offspring? Design of a case-control study. BMC medical genetics 2010;11:113.
121. Azoulay L, Chaumet-Riffaud P, Jaron S, et al. Threshold levels of visual field and acuity loss related to significant decreases in the quality of life and emotional states of patients with retinitis pigmentosa. Ophthalmic research 2015;54:78-84.

122. Langelaan M, de Boer MR, van Nispen RM, Wouters B, Moll AC, van Rens GH. Impact of visual impairment on quality of life: a comparison with quality of life in the general population and with other chronic conditions. Ophthalmic epidemiology 2007;14:119-26.
123. Park SJ, Ahn S, Woo SJ, Park KH. Extent of Exacerbation of Chronic Health Conditions by Visual Impairment in Terms of Health-Related Quality of Life. JAMA ophthalmology 2015;133:1267-75.
124. Facts about Bietti's crystalline dystrophy. (Accessed August 7, 2014, at http://www.nei.nih.gov/Health/biettis/index.asp.)
125. Bezemer ID, Bare LA, Doggen CJ, et al. Gene variants associated with deep vein thrombosis. Jama 2008;299:1306-14.
126. Bernauer W, Daicker B. Bietti's corneal-retinal dystrophy. A 16-year progression. Retina 1992;12:18-20.
127. Furusato E, Cameron JD, Chan CC. Evolution of Cellular Inclusions in Bietti's Crystalline Dystrophy. Ophthalmology and eye diseases 2010;2010:9-15.
128. Crouthamel MH, Kelly EJ, Ho RJ. Development and characterization of transgenic mouse models for conditional gene knockout in the blood-brain and blood-CSF barriers. Transgenic research 2012;21:113-30.
129. Parkinson OT, Liggitt HD, Rettie AE, Kelly EJ. Generation and characterization of a Cyp4b1 null mouse and the role of CYP4B1 in the activation and toxicity of Ipomeanol. Toxicological sciences : an official journal of the Society of Toxicology 2013;134:243-50.
130. Matyash V, Liebisch G, Kurzchalia TV, Shevchenko A, Schwudke D. Lipid extraction by methyl-tert-butyl ether for high-throughput lipidomics. Journal of lipid research 2008;49:1137-46.
131. Alpers CE, Hudkins KL, Pritzl P, Johnson RJ. Mechanisms of clearance of immune complexes from peritubular capillaries in the rat. The American journal of pathology 1991;139:855-67.
132. Flurkey K, Currer J, Harrison D. The mouse in aging research. In: Fox J, ed. The Mouse in Biomedical Research. 2nd ed. Burlington, MA: American College Laboratory Animal Medicine (Elesvier); 2007:637-72.
133. Curcio CA, Johnson M, Rudolf M, Huang JD. The oil spill in ageing Bruch membrane. The British journal of ophthalmology 2011;95:1638-45.
134. Curcio CA, Johnson M, Huang JD, Rudolf M. Apolipoprotein B-containing lipoproteins in retinal aging and age-related macular degeneration. Journal of lipid research 2010;51:451-67.
135. Fliesler SJ, Anderson RE. Chemistry and metabolism of lipids in the vertebrate retina. Progress in lipid research 1983;22:79-131.
136. Spite M, Claria J, Serhan CN. Resolvins, specialized proresolving lipid mediators, and their potential roles in metabolic diseases. Cell metabolism 2014;19:21-36.
137. Weylandt KH, Chiu CY, Gomolka B, Waechter SF, Wiedenmann B. Omega-3 fatty acids and their lipid mediators: towards an understanding of resolvin and protectin formation. Prostaglandins & other lipid mediators 2012;97:73-82.
138. Duffield JS, Hong S, Vaidya VS, et al. Resolvin D series and protectin D1 mitigate acute kidney injury. Journal of immunology 2006;177:5902-11.
139. Wang Y, Wang VM, Chan CC. The role of anti-inflammatory agents in age-related macular degeneration (AMD) treatment. Eye 2011;25:127-39.
140. Young RW. Shedding of discs from rod outer segments in the rhesus monkey. Journal of ultrastructure research 1971;34:190-203.

141. Mehlem A, Hagberg CE, Muhl L, Eriksson U, Falkevall A. Imaging of neutral lipids by oil red O for analyzing the metabolic status in health and disease. Nature protocols 2013;8:1149-54.
142. Young B, Eggenberger E, Kaufman D. Current electrophysiology in ophthalmology: a review. Current opinion in ophthalmology 2012;23:497-505.
143. Tullis BE, Ryals RC, Coyner AS, et al. Sarpogrelate, a 5-HT2A Receptor Antagonist, Protects the Retina From Light-Induced Retinopathy. Investigative ophthalmology & visual science 2015;56:4560-9.
144. Lyubarsky AL, Pugh EN, Jr. Recovery phase of the murine rod photoresponse reconstructed from electroretinographic recordings. The Journal of neuroscience : the official journal of the Society for Neuroscience 1996;16:563-71.
145. Pennesi ME, Cho JH, Yang Z, et al. BETA2/NeuroD1 null mice: a new model for transcription factor-dependent photoreceptor degeneration. The Journal of neuroscience : the official journal of the Society for Neuroscience 2003;23:453-61.
146. Fujimoto JG, Pitris C, Boppart SA, Brezinski ME. Optical coherence tomography: an emerging technology for biomedical imaging and optical biopsy. Neoplasia 2000;2:9-25.
147. Pennesi ME, Michaels KV, Magee SS, et al. Long-term characterization of retinal degeneration in rd1 and rd10 mice using spectral domain optical coherence tomography. Investigative ophthalmology & visual science 2012;53:4644-56.
148. Lockhart CM, Nakano M, Rettie AE, Kelly EJ. Generation and characterization of a murine model of Bietti crystalline dystrophy. Investigative ophthalmology & visual science 2014;55:5572-81.
149. Umino Y, Frio B, Abbasi M, Barlow R. A two-alternative, forced choice method for assessing mouse vision. Advances in experimental medicine and biology 2006;572:169-72.
150. Umino Y, Solessio E, Barlow RB. Speed, spatial, and temporal tuning of rod and cone vision in mouse. The Journal of neuroscience : the official journal of the Society for Neuroscience 2008;28:189-98.
151. Wong AA, Brown RE. Visual detection, pattern discrimination and visual acuity in 14 strains of mice. Genes, brain, and behavior 2006;5:389-403.
152. Ng DS, Lai TY, Ng TK, Pang CP. Genetics of Bietti Crystalline Dystrophy. Asia-Pacific journal of ophthalmology 2016.
153. Weleber RG, Smith TB, Peters D, et al. VFMA: Topographic Analysis of Sensitivity Data From Full-Field Static Perimetry. Translational vision science & technology 2015;4:14.
154. Marmor MF, Fulton AB, Holder GE, et al. ISCEV Standard for full-field clinical electroretinography (2008 update). Documenta ophthalmologica Advances in ophthalmology 2009;118:69-77.
155. Oh KT, Weleber RG, Stone EM, Oh DM, Rosenow J, Billingslea AM. Electroretinographic findings in patients with Stargardt disease and fundus flavimaculatus. Retina 2004;24:920-8.
156. Hood DC, Bach M, Brigell M, et al. ISCEV standard for clinical multifocal electroretinography (mfERG) (2011 edition). Documenta ophthalmologica Advances in ophthalmology 2012;124:1-13.
157. Zhang Y. I-TASSER server for protein 3D structure prediction. BMC bioinformatics 2008;9:40.
158. Pronk S, Pall S, Schulz R, et al. GROMACS 4.5: a high-throughput and highly parallel open source molecular simulation toolkit. Bioinformatics 2013;29:845-54.

159. Oda A, Yamaotsu N, Hirono S. New AMBER force field parameters of heme iron for cytochrome P450s determined by quantum chemical calculations of simplified models. Journal of computational chemistry 2005;26:818-26.
160. Roberts AG, Cheesman MJ, Primak A, Bowman MK, Atkins WM, Rettie AE. Intramolecular heme ligation of the cytochrome P450 2C9 R108H mutant demonstrates pronounced conformational flexibility of the B-C loop region: implications for substrate binding. Biochemistry 2010;49:8700-8.
161. Baer BR, Schuman JT, Campbell AP, et al. Sites of covalent attachment of CYP4 enzymes to heme: evidence for microheterogeneity of P450 heme orientation. Biochemistry 2005;44:13914-20.
162. Jurklies B, Jurklies C, Schmidt U, Wessing A, Bornfeld N. [Corneoretinal dystrophy (Bietti)-- Long-term course of one patient over a period of 30 years, and interindividual variability of clinical and electrophysiological findings in two patients]. Klinische Monatsblatter fur Augenheilkunde 2001;218:562-9.
163. Mansour AM, Uwaydat SH, Chan CC. Long-term follow-up in Bietti crystalline dystrophy. European journal of ophthalmology 2007;17:680-2.
164. Sanchez Vicente JL, Herrador Montiel A, Diez-Garretas C, Guiote Linares JR. [Bietti's crystalline dystrophy. A 5-year progression]. Archivos de la Sociedad Espanola de Oftalmologia 2001;76:323-6.
165. Broadhead GK, Chang AA. Acetazolamide for cystoid macular oedema in Bietti crystalline retinal dystrophy. Korean journal of ophthalmology : KJO 2014;28:189-91.
166. Li Q, Li Y, Zhang X, et al. Utilization of Fundus Autofluorescence, Spectral Domain Optical Coherence Tomography, and Enhanced Depth Imaging in the Characterization of Bietti Crystalline Dystrophy in Different Stages. Retina 2015;35:2074-84.
167. Safdar H, Cleuren AC, Cheung KL, et al. Regulation of the F11, Klkb1, Cyp4v3 gene cluster in livers of metabolically challenged mice. PloS one 2013;8:e74637.
168. Muerhoff AS, Williams DE, Reich NO, CaJacob CA, Ortiz de Montellano PR, Masters BS. Prostaglandin and fatty acid omega- and (omega-1)-oxidation in rabbit lung. Acetylenic fatty acid mechanism-based inactivators as specific inhibitors. The Journal of biological chemistry 1989;264:749-56.
169. Okialda KA. Screening for microRNA regulators of an orphan cytochrome P450 4V2 (CYP4V2): a thesis submitted in partial fulfillment of the requirements for the degree of Master of Science in Pharmaceutics.: University of Washington; 2012.
170. Tsuchiya Y, Nakajima M, Takagi S, Taniya T, Yokoi T. MicroRNA regulates the expression of human cytochrome P450 1B1. Cancer research 2006;66:9090-8.
171. Li Y, Bezemer ID, Rowland CM, et al. Genetic variants associated with deep vein thrombosis: the F11 locus. J Thromb Haemost 2009;7:1802-8.
172. Tregouet DA, Heath S, Saut N, et al. Common susceptibility alleles are unlikely to contribute as strongly as the FV and ABO loci to VTE risk: results from a GWAS approach. Blood 2009;113:5298-303.
173. Murray GI, Patimalla S, Stewart KN, Miller ID, Heys SD. Profiling the expression of cytochrome P450 in breast cancer. Histopathology 2010;57:202-11.
174. Yokoi T, Nakajima M. Toxicological implications of modulation of gene expression by microRNAs. Toxicol Sci 2011;123:1-14.
175. Lee RC, Feinbaum RL, Ambros V. The C. elegans heterochronic gene lin-4 encodes small RNAs with antisense complementarity to lin-14. Cell 1993;75:843-54.

176. Wightman B, Burglin TR, Gatto J, Arasu P, Ruvkun G. Negative regulatory sequences in the lin-14 3'-untranslated region are necessary to generate a temporal switch during Caenorhabditis elegans development. Genes & development 1991;5:1813-24.
177. Bartel DP. MicroRNAs: genomics, biogenesis, mechanism, and function. Cell 2004;116:281-97.
178. Pillai RS. MicroRNA function: multiple mechanisms for a tiny RNA? Rna 2005;11:1753-61.
179. Friedman RC, Farh KK, Burge CB, Bartel DP. Most mammalian mRNAs are conserved targets of microRNAs. Genome Res 2009;19:92-105.
180. Kloosterman WP, Plasterk RH. The diverse functions of microRNAs in animal development and disease. Dev Cell 2006;11:441-50.
181. Carthew RW, Sontheimer EJ. Origins and Mechanisms of miRNAs and siRNAs. Cell 2009;136:642-55.
182. Krol J, Loedige I, Filipowicz W. The widespread regulation of microRNA biogenesis, function and decay. Nat Rev Genet 2010;11:597-610.
183. Paine MF, Khalighi M, Fisher JM, et al. Characterization of interintestinal and intraintestinal variations in human CYP3A-dependent metabolism. The Journal of pharmacology and experimental therapeutics 1997;283:1552-62.
184. Gordon WC, Rodriguez de Turco EB, Bazan NG. Retinal pigment epithelial cells play a central role in the conservation of docosahexaenoic acid by photoreceptor cells after shedding and phagocytosis. Current Eye Research 1992;11:73-83.
185. Serhan CN, Hong S, Gronert K, et al. Resolvins: a family of bioactive products of omega-3 fatty acid transformation circuits initiated by aspirin treatment that counter proinflammation signals. J Exp Med 2002;196:1025-37.
186. Bazan NG. Neuroprotectin D1-mediated anti-inflammatory and survival signaling in stroke, retinal degenerations, and Alzheimer's disease. J Lipid Res 2009;50 Suppl:S400-5.
187. Dangi B, Obeng M, Nauroth JM, et al. Metabolism and biological production of resolvins derived from docosapentaenoic acid (DPAn-6). Biochemical pharmacology 2009.
188. Recchiuti A, Krishnamoorthy S, Fredman G, Chiang N, Serhan CN. MicroRNAs in resolution of acute inflammation: identification of novel resolvin D1-miRNA circuits. The FASEB Journal 2010;25:544-60.
189. Taganov KD, Boldin MP, Chang KJ, Baltimore D. NF-kappaB-dependent induction of microRNA miR-146, an inhibitor targeted to signaling proteins of innate immune responses. Proceedings of the National Academy of Sciences of the United States of America 2006;103:12481-6.
190. Schmidt WM, Spiel AO, Jilma B, Wolzt M, Muller M. In vivo profile of the human leukocyte microRNA response to endotoxemia. Biochem Biophys Res Commun 2009;380:437-41.
191. Hulsmans M, De Keyzer D, Holvoet P. MicroRNAs regulating oxidative stress and inflammation in relation to obesity and atherosclerosis. Faseb J 2011;25:2515-27.
192. Hulsmans M, Geeraert B, De Keyzer D, et al. Interleukin-1 receptor-associated kinase-3 is a key inhibitor of inflammation in obesity and metabolic syndrome. PLoS One 2012;7:e30414.
193. Hulsmans M, Van Dooren E, Mathieu C, Holvoet P. Decrease of miR-146b-5p in Monocytes during Obesity Is Associated with Loss of the Anti-Inflammatory but Not Insulin Signaling Action of Adiponectin. PLoS One 2012;7:e32794.

194. Takahashi N, Nakaoka T, Yamashita N. Profiling of immune-related microRNA expression in human cord blood and adult peripheral blood cells upon proinflammatory stimulation. Eur J Haematol 2012;88:31-8.
195. Majno G. Inflammation and infection: historic highlights. Monographs in pathology 1982:1-17.
196. Xia H, Qi Y, Ng SS, et al. microRNA-146b inhibits glioma cell migration and invasion by targeting MMPs. Brain Res 2009;1269:158-65.
197. Katakowski M, Zheng X, Jiang F, Rogers T, Szalad A, Chopp M. MiR-146b-5p suppresses EGFR expression and reduces in vitro migration and invasion of glioma. Cancer Invest 2010;28:1024-30.
198. Hurst DR, Edmonds MD, Scott GK, Benz CC, Vaidya KS, Welch DR. Breast cancer metastasis suppressor 1 up-regulates miR-146, which suppresses breast cancer metastasis. Cancer Research 2009;69:1279-83.
199. Lin F, Wang X, Jie Z, et al. Inhibitory effects of miR-146b-5p on cell migration and invasion of pancreatic cancer by targeting MMP16. J Huazhong Univ Sci Technolog Med Sci 2011;31:509-14.
200. Patnaik SK, Kannisto E, Mallick R, Yendamuri S. Overexpression of the lung cancer-prognostic miR-146b microRNAs has a minimal and negative effect on the malignant phenotype of A549 lung cancer cells. PLoS One 2011;6:e22379.
201. Patnaik SK, Kannisto E, Knudsen S, Yendamuri S. Evaluation of microRNA expression profiles that may predict recurrence of localized stage I non-small cell lung cancer after surgical resection. Cancer Research 2010;70:36-45.
202. Garcia AI, Buisson M, Bertrand P, et al. Down-regulation of BRCA1 expression by miR-146a and miR-146b-5p in triple negative sporadic breast cancers. EMBO Mol Med 2011;3:279-90.
203. Pallante P, Visone R, Croce CM, Fusco A. Deregulation of microRNA expression in follicular-cell-derived human thyroid carcinomas. Endocr Relat Cancer 2010;17:F91-104.
204. Geraldo MV, Yamashita AS, Kimura ET. MicroRNA miR-146b-5p regulates signal transduction of TGF-beta by repressing SMAD4 in thyroid cancer. Oncogene 2011.
205. Calder PC. Polyunsaturated fatty acids and inflammation. Prostaglandins Leukot Essent Fatty Acids 2006;75:197-202.
206. Ryan GB, Majno G. Acute inflammation. A review. Am J Pathol 1977;86:183-276.
207. Serhan CN, Clish CB, Brannon J, Colgan SP, Chiang N, Gronert K. Novel functional sets of lipid-derived mediators with antiinflammatory actions generated from omega-3 fatty acids via cyclooxygenase 2-nonsteroidal antiinflammatory drugs and transcellular processing. J Exp Med 2000;192:1197-204.
208. Genetic Eye Diseases. September 2015. (Accessed September 14, 2015, at http://www.eyewiki.aao.org.)
209. Orphan Drug Act. 21 CFR Section 316. United States1983.
210. Lucentis(R) [Prescribing Information]. Genentech, Inc. . February 2015. (Accessed May 29, 2016, at http://www.gene.com/download/pdf/lucentis_prescribing.pdf.)
211. Dalkara D, Byrne LC, Klimczak RR, et al. In vivo-directed evolution of a new adeno-associated virus for therapeutic outer retinal gene delivery from the vitreous. Science translational medicine 2013;5:189ra76.
212. Kolstad KD, Dalkara D, Guerin K, et al. Changes in adeno-associated virus-mediated gene delivery in retinal degeneration. Human gene therapy 2010;21:571-8.

213. Dalkara D, Kolstad KD, Caporale N, et al. Inner limiting membrane barriers to AAV-mediated retinal transduction from the vitreous. Molecular therapy : the journal of the American Society of Gene Therapy 2009;17:2096-102.
214. Atchison RW, Casto BC, Hammon WM. Adenovirus-Associated Defective Virus Particles. Science 1965;149:754-6.
215. Goncalves MA. Adeno-associated virus: from defective virus to effective vector. Virology journal 2005;2:43.
216. Dalkara D, Sahel JA. Gene therapy for inherited retinal degenerations. Comptes rendus biologies 2014;337:185-92.
217. Mowat FM, Gornik KR, Dinculescu A, et al. Tyrosine capsid-mutant AAV vectors for gene delivery to the canine retina from a subretinal or intravitreal approach. Gene therapy 2014;21:96-105.
218. Petrs-Silva H, Dinculescu A, Li Q, et al. High-efficiency transduction of the mouse retina by tyrosine-mutant AAV serotype vectors. Molecular therapy : the journal of the American Society of Gene Therapy 2009;17:463-71.
219. Surace EM, Auricchio A. Versatility of AAV vectors for retinal gene transfer. Vision research 2008;48:353-9.
220. Choi VW, McCarty DM, Samulski RJ. AAV hybrid serotypes: improved vectors for gene delivery. Current gene therapy 2005;5:299-310.
221. Martin KR, Klein RL, Quigley HA. Gene delivery to the eye using adeno-associated viral vectors. Methods 2002;28:267-75.
222. Bainbridge JW, Smith AJ, Barker SS, et al. Effect of gene therapy on visual function in Leber's congenital amaurosis. The New England journal of medicine 2008;358:2231-9.
223. Cideciyan AV, Aleman TS, Boye SL, et al. Human gene therapy for RPE65 isomerase deficiency activates the retinoid cycle of vision but with slow rod kinetics. Proceedings of the National Academy of Sciences of the United States of America 2008;105:15112-7.
224. Hauswirth WW, Aleman TS, Kaushal S, et al. Treatment of leber congenital amaurosis due to RPE65 mutations by ocular subretinal injection of adeno-associated virus gene vector: short-term results of a phase I trial. Human gene therapy 2008;19:979-90.
225. Maguire AM, Simonelli F, Pierce EA, et al. Safety and efficacy of gene transfer for Leber's congenital amaurosis. The New England journal of medicine 2008;358:2240-8.
226. Bainbridge JW, Mehat MS, Sundaram V, et al. Long-term effect of gene therapy on Leber's congenital amaurosis. The New England journal of medicine 2015;372:1887-97.
227. Cideciyan AV. Leber congenital amaurosis due to RPE65 mutations and its treatment wtih gene therapy. Progress in retinal and eye research 2010;29:398-427.
228. Maguire AM, High KA, Auricchio A, et al. Age-dependent effects of RPE65 gene therapy for Leber's congenital amauarosis: a phase 1 dose-escalation trial. Lancet 2009;374:1597-605.
229. Pang JJ, Chang B, Kumar A, et al. Gene therapy restores vision-dependent behavior as well as retinal structure and function in a mouse model of RPE65 Leber congenital amaurosis. Molecular therapy : the journal of the American Society of Gene Therapy 2006;13:565-72.
230. Pierce EA, Bennett J. The status of RPE65 gene therapy trials: safety and efficacy. Cold Spring Harb Perspect Med 2015:a017285.
231. Schimmer J, Breazzano S. Investor Outlook: Focus on Upcoming LCA2 Gene Therapy Phase III Results. Hum Gene Ther Clin Develop 2015;26:144-9.

232. Cideciyan AV, Aguirre GK, Jacobson SG, et al. Pseudo-fovea formation after gene therapy for RPE65-LCA. Investigative ophthalmology & visual science 2015;56:526-37.
233. Cideciyan AV, Jacobson SG, Beltran WA, et al. Human retinal gene therapy for Leber congenital amaurosis shows advancing retinal degeneration despite enduring visual improvement. Proceedings of the National Academy of Sciences of the United States of America 2013;110:E517-25.
234. Jacobson SG, Cideciyan AV, Roman AJ, et al. Improvement and decline in vision with gene therapy in childhood blindness. The New England journal of medicine 2015;372:1920-6.
235. Jacobson SG, Cideciyan AV, Ratnakaram R, et al. Gene therapy for leber congenital amaurosis caused by RPE65 mutations: safety and efficacy in 15 children and adults followed up to 3 years. Archives of ophthalmology 2012;130:9-24.
236. Cideciyan AV, Hauswirth WW, Aleman TS, et al. Human RPE65 gene therapy for Leber congenital amaurosis: persistence of early visual improvements and safety at 1 year. Human gene therapy 2009;20:999-1004.
237. Simonelli F, Maguire AM, Testa F, et al. Gene therapy for Leber's congenital amaurosis is safe and effective through 1.5 years after vector administration. Molecular therapy : the journal of the American Society of Gene Therapy 2010;18:643-50.
238. Colour Blindness. Colour Blind Awareness. (Accessed May 29, 2016, at http://www.colourblindawareness.org/colour-blindness/.)
239. Mancuso K, Hauswirth WW, Li Q, et al. Gene therapy for red-green colour blindness in adult primates. Nature 2009;461:784-7.
240. Mancuso K, Mauck MC, Kuchenbecker JA, Neitz M, Neitz J. A multi-stage color model revisited: implications for a gene therapy cure for red-green colorblindness. Advances in experimental medicine and biology 2010;664:631-8.
241. Neitz M, Neitz J. Curing color blindness--mice and nonhuman primates. Cold Spring Harb Perspect Med 2014;4:a017418.

VITAE

Catherine M. Lockhart was born in Boise, Idaho. In 1998, she graduated from the University of Idaho with a B.F.A. in Theatre Arts and a B.S. in Visual Communications. After working professionally in theatre for several years, she returned to school and graduated with a B.S. in Electrical Engineering from the University of Washington in 2004. In 2009 she entered the School of Pharmacy at the University of Washington to pursue a concurrent Pharm.D. and Ph.D. in Pharmaceutics. She graduated with a Pharm.D. in 2013, and joined Dr. Edward Kelly's lab to complete her Ph.D. In 2015 she also entered the Department of Pharmacy to complete an M.S. in Pharmaceutical Outcomes Research, Pharmacoeconomics and Policy. Catherine was the recipient of a Plein Fund grant, an Institute of Translational Sciences Pilot Study grant, and an NIH TL1 Multidisciplinary Clinical Research training grant.